Spin-flip Raman spectroscopy of ZnCdSe-based heterostructures

Karimov, Oleg Zufarovitch

Award date:
2000

Awarding institution:
University of Bath

Spin-flip Raman spectroscopy of ZnCdSe-based heterostructures

Submitted by Oleg Zufarovitch Karimov
for the degree of
Doctor of Philosophy
of the University of Bath
2000

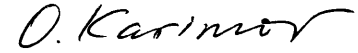

ProQuest LLC
789 East Eisenhower Parkway
P.O. Box 1346
Ann Arbor, MI 48106-1346

To my parents

Abstract

This thesis presents the results of the study of ZnCdSe-based heterostructures of two systems, namely bulk single-phase cubic ZnCdSe epilayers with Cd content varying from 0 to 100 percent and ZnCdSe/Zn(S)Se quantum wells. In the latter system increased attention has been paid to the special case of submonolayer structures. The main tool of the study, spin-flip Raman spectroscopy, enabled observation of sharp spectral features related to the spin transitions of different excitations of these systems. The analysis of the experimental data allowed determination of the nature of these excitations as well as their parameters, leading thus to a better understanding of the properties of the systems studied.

Acknowledgments

I am very grateful to:

Prof J. J. Davies and Dr D. Wolverson for giving me the opportunity to carry out this work, for the steady support and ready accessibility in a countless number of discussions; for taking over the considerable task of reading the whole thesis before its submission, making helpful comments and suggestions as well as for having to suffer the quality of my English.

Dr T. Ruf and Prof M. Cardona for making possible my visits of the Max-Planck Institute in Stuttgart to conduct experiments in high magnetic fields and for fruitful discussions.

Prof S. A. Permogorov and the members of his group for their close collaboration.

Dr V. F. Sapega, Dr Yu. G. Kusraev and Dr R. T. Harley for helpful discussions.

Dr S. V. Ivanov, Prof K. Prior, Prof D. Hommel, Prof S. J. C. Irvine and Dr K. Ogata for providing high quality samples.

Mr S. I. Stepanov and Mr S. Strauf for the measurements of the X-ray scattering and PLE spectra.

Mr R. J. C. Draper, Mr H. Bone, Mr H. Hirt and Mr M. Siemers for providing excellent technical assistance.

my housemates, particularly Ivan Griffin, Leonard Mwaikambo, Shin Ushiroda, Ken-ichi Ogata and Alexander Grigorenko for lots of fun "outside" physics.

my friend Ms M. Last for all her help and care through these years - my thanks to her cannot be measured.

my parents and sister - without their moral support, everything would have been far more difficult.

the University of East Anglia and CVCP ORS award schema for financial support.

Preface

Physics of semiconductors heterostructures nowadays is one of the most important and fastest developing areas of solid state physics[1]. The importance and fast development of the field are determined by the demand of micro/opto-electronics and the power of modern epitaxial technologies allowing production sophisticated heterostructures with desirable physical properties.

Being of paramount importance from the application point of view, the physics of semiconductor heterostructures provides also a wide field for the basic research. Most attention is paid to low-dimensional heterostructures, where the energy spectrum, symmetry and fundamental parameters of the quasi-particles are modified compared to the three-dimensional case. At the same time the studies of "simple" bulk epitaxial heterolayers in many situations are necessary prerequisites for the understanding of the basic properties of the low-dimensional case. Moreover, such studies provide a unique possibility of testing the existing theories, particularly the band structure theories, when they are applied to bulk semiconductor materials, which may only be grown by heteroepitaxy. Many effects in semiconductor heterostructures, particularly those that are caused by the reduction of dimensionality can be successfully studied by optical methods. Amongst them, spin-flip Raman spectroscopy has proved to be one of the most powerful. All this makes the chosen theme of study highly topical.

The thesis consists of five chapters. The first two chapters provide a background of spin-flip Raman spectroscopy and ZnCdSe-based heterostructures. The next two chapters present the original experimental results and their discussion. The overall conclusions are given in the last chapter. There are four appendices at the back of the thesis. Appendix A contains a table with some of the parameters of ZnSe and CdSe. Appendices B, C and D contain information concerning the electron g-factor, the $\mathbf{k} \cdot \mathbf{p}$ method and the exchange interaction.

The results included in this thesis were presented at two UK and three international conferences and published in refereed journals.

[1]During the last 15 years three Nobel prizes were awarded for works related to the physics of semiconductor heterostructures.

Contents

Chapter 1

Spin-flip Raman spectroscopy

1.1 Introduction

Spin-flip Raman (SFR) spectroscopy is an effective and nowadays a well established tool for the investigation of semiconductors. This type of Raman spectroscopy is based on the process of so called "spin-flip Raman scattering" of light. In this process the electric field of light incident on a semiconductor interacts via spin-orbit coupling with an elementary spin excitation in a magnetic field and induces a change of the spin state (or spin-flip). This leads to the energy of the scattered light being shifted, in the simplest case, by an amount equal to the Zeeman spin-splitting energy

$$\Delta E = \hbar(\omega_l - \omega_s) = g\mu_B B, \tag{1.1}$$

where $\omega_l(\omega_s)$ denotes the frequency of the incident(scattered) light, g is the absolute value of the effective g-factor of the elementary spin excitation, $\mu_B = e\hbar/2mc$ is the Bohr magneton and B is the magnetic field. In Eq. 1.1 ΔE can be either positive or negative, corresponding respectively to whether the light loses (Stokes process) or gains (anti-Stokes process) energy due to the interaction with the elementary spin excitation. Thus SFR spectroscopy enables one to observe the elementary spin excitations of semiconductors by the frequency shift between the incident and scattered light, and by varying conditions of the experiment (magnetic field, polarization, temperature, etc.), to investigate their properties.

During more than 30 years of application of SFR spectroscopy (see the following section) the properties of a large variety of excitations in bulk non magnetic and diluted magnetic semiconductors were investigated; see examples in Refs. [1, 2, 3] and Refs. [4, 5, 6, 7], respectively. The signals from both free electrons and free holes, electrons bound to donors and holes bound to acceptors, localized excitons, bound magnetic polarons, as well as scattering spin-flip transitions within the Zeeman multiplets of paramagnetic ions, have been detected. From these measurements, band structure and single particle parameters such as effective g-factors and life times, electron-hole exchange constants of excitons, as well as information about the dynamics of spin relaxation of individual carriers and excitons, can be obtained. SFR spectroscopy has also been applied successfully to investigate epitaxial semiconductor heterostructures, including bulk epilayers and low dimensional structures. Examples of such studies can be found in Refs. [8, 9, 10, 11] and Refs. [12, 13, 14, 15, 16, 17, 18], respectively.

In this chapter we provide general information on spin-flip Raman spectroscopy, covering the important historical steps of its development and describing the main components of its experimental arrangement. Some important aspects of the theory of spontaneous Raman scattering helpful for the presentation of the experimental results of Chapters 3 and 4 are also discussed.

1.2 Historical survey

SFR spectroscopy is not a new tool for investigation of semiconductors and its up to date experimental setup is described in section 1.3. The theoretical background for SFR spectroscopy originates from the works of Elliott [19] and Elliott and Loudon [20] published, respectively, in 1954 and 1963. In these works it was shown that the SFR process is possible in the presence of mixing of spin and orbital states and thus can be realized in semiconductors. The next step was made by Wolff in 1966 [21], who gave for the first time a detailed consideration of inelastic light scattering by mobile carriers (electrons and holes) in semiconductors in a magnetic field. He predicted a Raman process which involves a transition between two Landau levels with $\Delta n = 2$. Electron spin effects were not considered. This work was extended by Yafet [22] and by Kelley and Wright [23], who included the mixed spin character of the valence states of InSb induced by spin-

orbit coupling and considered a spin-flip process with $\Delta n = 0$. They estimated the cross sections for the Raman scattering by electrons and holes for InSb and InP, finding them sufficiently large to permit the observation of this type of the Raman transition. They also pointed out that SFR transitions can be of use in band structure measurements. Very shortly after these theoretical works the first experimental observations of spontaneous SFR scattering by mobile electrons in InSb were reported by Slusher, Patel and Fleury [24] in 1967, followed by the detection of SFR signals from bound electrons and holes in CdS by Thomas and Hopfield [25] in 1968. In the last of these works the effective g-factors of bound carriers were determined and also a theory was developed which gives a qualitative understanding of the phenomenon as taking place via intermediate state formed by bound excitons. Since then there has been a growing interest in using SFR spectroscopy for the investigation of semiconductors.

An important contribution to this field was the first spectroscopic observation of stimulated SFR scattering from conduction electrons in InSb by Patel and Shaw [26] and in CdS by Scott and Damen [27], respectively in the infra-red and the visible. This led then to the development of the tunable SFR laser acting in both pulsed and c.w. modes of operation; a comprehensive review of SFR lasers can be found in Ref. [28]. The tuning is achieved by changing the applied magnetic field (see Eq. 1.1). The basic physical process of the SFR laser is based on the quantum mechanical motion of the electrons in magnetic states and is of a great interest in pure physics. This fact caused more attention to be given to SFR spectroscopy.

A very important step for the development of SFR spectroscopy tool was made when tunable dye- and Titanium sapphire lasers became widely available in the 70's and 80's. The scattering efficiency is strongly increased, sometimes up to several orders of magnitude, when the incident photon energy is in resonance with one of the optically allowed intermediate state. Such "resonance" behaviour had been already pointed out by Yafet [22]. It plays a crucial role in SFR studies and will be considered further in this Chapter (subsection 1.4.2).

Several reviews have been published which cover different aspects of SFR spectroscopy of semiconductors. We mention some of these reviews given by Scott [29], Geschwind and Romestain [30], Häfele [31] and Davies *et al.* [32]. In the latest review a comparison of the sensitivity and spectral resolution obtained by

SFR spectroscopy with that of other widely used magneto and magneto-optical techniques (electron spin resonance, optically detected magnetic resonance and Zeeman spectroscopy) is also provided.

1.3 Experimental arrangement

The experimental arrangement of SFR spectroscopy of semiconductors in general consists of a continuous wave laser light source, a high resolution spectrometer equipped with a very sensitive photon detector and a helium cryostat with a strong magnet. In some cases the spectrometer is replaced by a multipass Fabry-Perot, which is usually piezoelectrically scanned. This allows the spectral resolution of the apparatus to be increased up to a hundred times compared to a spectrometer based one [30]. Nevertheless in many cases a spectrometer provides the necessary resolution and is the first choice for SFR studies. The experimental results presented in the Chapters 3 and 4 have been obtained using a spectrometer based computer controlled apparatus of the Optical Spectroscopy Group at the University of Bath[1]. A schematic representation of this apparatus is shown in Fig. 1.1. A significant part of the experiments was also performed using the high magnetic field facilities of the Cardona Department at the Max-Planck-Institut für Festkörperforschung in Stuttgart, where the apparatus is also based on a spectrometer. In this section a description of the requirements for the main components of the experimental technique for SFR spectroscopy, along with technical details of the apparatus in Bath and Stuttgart, is provided.

The requirements of a source for the excitation of Raman spectra in general and SFR in particular are that it should be stable, intense and highly monochromatic (narrow line width). A laser meets these requirements perfectly and, in addition, provides a beam which is self-collimated and plane polarized. Different gas lasers which produce a variety of discrete lines covering a wide spectral interval from infrared to ultraviolet are available. For fine adjustment of the incident wavelength, as is essential for resonant SFR scattering, lasers with a quasi-continuous tuning range are often used. These tunable lasers are based on a laser medium which gives stimulated emission in a wide spectral range in which the laser wavelength

[1]This apparatus was also used for photoluminescence, reflectance and phonon Raman measurements.

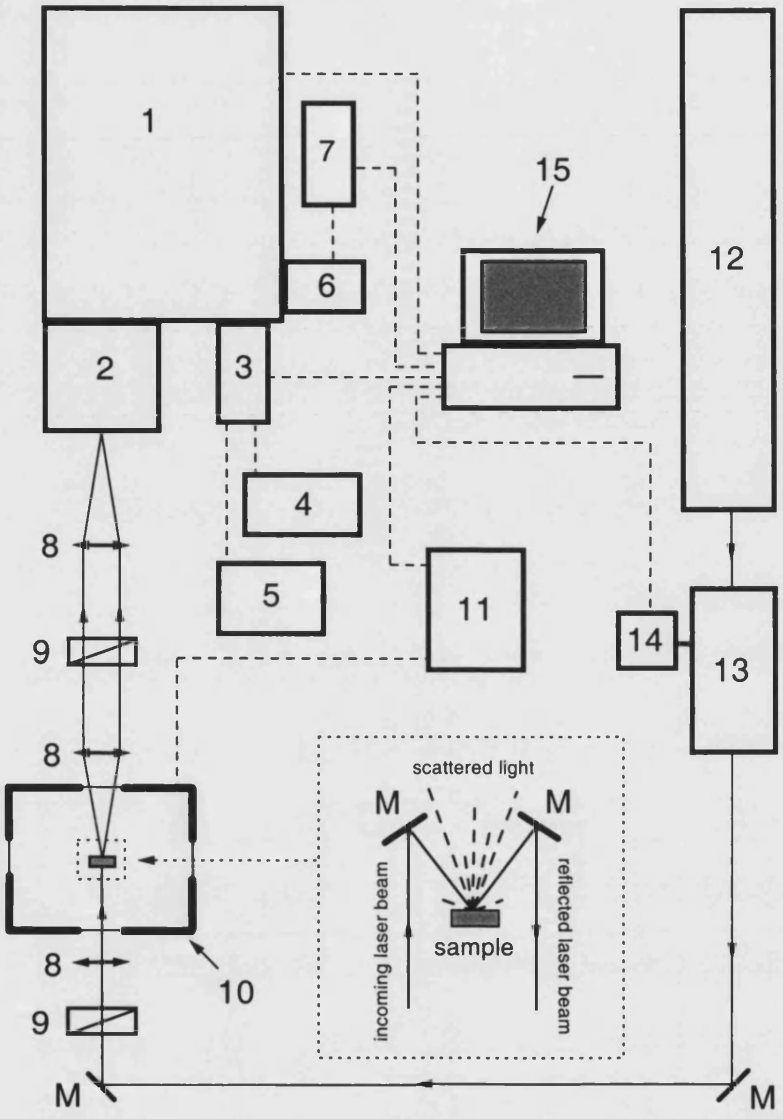

Figure 1.1: Schematic picture of the main components of the apparatus for SFR scattering measurements (Optical spectroscopy group, University of Bath). 1 - monochromator, 2 - premonochromator, 3 - photomultiplier and photon counting electronics, 4 - photomultiplier stabilized power supply, 5 - photomultiplier Peltier-effect cooler, 6 - liquid nitrogen cooled CCD camera, 7 - CCD camera interface, 8 - lenses, 9 - linear or circular polarizers, 10 - cryostat with the magnet, 11 - stabilized power supply and operational block for the magnet, 12 - pumping Ar^+ ion laser, 13 - dye or Ti-sapphire laser, 14 - stepper motor, 15 - computer system for apparatus operation and data acquisition, M - mirrors. The inset shows the arrangement for a sample in the sample chamber of the cryostat.

can be chosen by change of the laser cavity resonant conditions. Generally, liquid dyes are used as a lasing medium. The spectral region of each dye covers about 50 nm but the availability of a large number of different dyes makes possible to cover the whole spectral region between 390 nm and 900 nm ($\sim 3.18 - 1.38$ eV). By use of an appropriate pumping source some dyes even allow one to achieve a shorter wavelength than 390 nm. A tunable solid state laser whose laser medium is a Titanium sapphire crystal covering the spectral range between 700 nm and 1 μm ($\sim 1.77 - 1.24$ eV) is also available. This laser is free from problems of the dye-laser caused by the limited life time of any of the dyes but at the same time the possible extension to the wavelength region shorter than 700 nm requires the use of very expensive frequency doublers, which at present do not operate in the continuous wave regime. All of our experiments were performed using these two types of tunable lasers, which were pumped by an Ar^+-ion laser (dyes used were S1, S3, C420, C480, Pyromethene and R6G). Both lasers could be tuned to an appropriate wavelength by a stepper motor automatically operated by the computer system. Using an etalon inserted into the dye laser cavity allows one to reduce the laser linewidth by a factor of 3, making it comparable with the instrumental linewidth of the spectrometer. For investigating the selection rules of SFR scattering the polarization of the incident light can be varied by a combination of a linear polarizer and a $\lambda/4$ (or $\lambda/2$) plate. The laser beam of power 0.1-100 mW is focused on to the sample by a long-focus spherical lens into a spot of 0.5 mm in diameter.

The scattered light is collected through a lens system and focused on to the entrance slit of a spectrometer. A high-quality imaging system is required since the entrance slit must be quite narrow to achieve a sufficient spectral resolution (usually 10-20 μm). Spherical aberration effects should be minimized, because they reduce the effective aperture angle and therefore can affect measurements of weak intensity signals. A polarization analyzer inserted in front of the entrance slit allows the selective detection of scattered light with a well-defined polarization, so as to separate the individual component of the Raman tensor. For the frequency analysis of the scattered light, a spectrometer based on a grating monochromator is used. Because of the low efficiency of the scattering (resulting often in less than 100 photon counts/s), the monochromator must produce a very high frequency resolution to separate the very weak Raman light from the far more intense elastically-scattered (Rayleigh) light. The frequency resolution is determined by the focal length of the monochromator, the line density of the gratings, the size of

the grating and the slit widths. The setup in Bath is equipped with a Jobin-Yvon S 3000 spectrometer containing a single grating 0.64 m focal length monochromator and a double subtractive grating pre-monochromator (both Czerny–Turner arrangements; the gratings have 1800 grooves/mm). The pre-monochromator acts as a spatial filter for the monochromator and serves to improve stray light reduction. The setup in Stuttgart is based on a SPEX 1404 double grating (1800 grooves/mm) 0.8 m focal length monochromator (Czerny–Turner arrangements). The spectrometers are equipped with single-photon counting photomultiplier systems. The spectrometer in Bath is additionally equipped with a CCD camera. Both of the systems allow one to measure Raman signals as close as 1.5 cm^{-1} ($\sim$ 0.2 meV) to the laser line.

Helium cryostats of two types were used in our experiments. In the first cryostat, the sample is placed in superfluid helium at a temperature of 1.5 K in a split-pair magnet that is capable of generating magnetic fields of up to 6 T (Bath). The second cryostat has a solenoid superconducting magnet producing magnetic fields of up to 14 T and, since the sample is held in a helium exchange gas, allows temperatures down only to about 4.5 K (Stuttgart). Both cryostats are equipped with temperature controllers allowing measurements at temperatures up to room temperature.

The SFR scattering experiments were performed in the backscattering Faraday geometry, in which the magnetic field $\mathbf{B}$ and the light propagation direction $\mathbf{k}$ are parallel, and in the backscattering Voigt geometry, in which $\mathbf{B}$ and $\mathbf{k}$ are perpendicular to each another. In the split-pair magnet cryostat, to change from the Faraday geometry to Voigt, the magnet is rotated through 90 degrees. The arrangement of the sample in the cryostat is shown in the inset of Fig. 1.1. In this arrangement the laser beam is incident on the sample surface at a certain angle, but because of the high refractive index of about 3.0 for all of the semiconductors investigated, the light travels internally very close to the normal to the surface (deviation $\sim$ 5 degrees). The use of a special sample holder allowed a continuous rotation to give an angle θ between the specimen normal and the magnetic field where, in the Faraday geometry, $|\theta|$ ranged from 0 to 50 degrees and, in the Voigt geometry, from 40 to 90 degrees. By these means we are able to measure the angular dependences of the SFR scattering signals for all field directions. In the solenoid magnet cryostat, the sample could also be placed in the Faraday and Voigt geometries. The arrangements for both geometries are shown in Fig.

1.2. In this magnet, a continues rotation of the sample was not possible, but the sample could also be mounted with a fixed angle θ of 15, 30, 45, 60 or 75 degrees[2]. Two deficiencies which are important for the precise measurements of polarization dependences in a magnetic field in the Voigt geometry have to be mentioned. The first of them comes from the axes of the solid angle of the scattered light being tilted relatively to the sample normal. This leads to the additional polarization of the scattered light due to the effect of Fresnel polarization. The second deficiency arises since the use of the glass lens causes the rotation of the polarization plane in the magnetic field due to the Faraday effect and therefore leads to incorrect values of the measured polarization. The effects, however, can easily be excluded by measurements of their influence at different values of the magnetic field. These correction factors were kindly made available to us by V. F. Sapega. The internal diameter of the solenoid and the focal lengths of the spherical mirror and the lens cause the maximal deviation of the scattered light inside the sample away from the normal to the sample surface to be not more than 5 degrees - similar to the case of the split-pair cryostat. Therefore, the experimental results can be compared without significant errors with the theory in which the incident light and the scattered light are considered to be parallel.

1.4 Basics of Raman scattering theory

1.4.1 Classical and quantum mechanical pictures

The effect of Raman scattering, in which light is scattered inelastically by molecules or crystals with a change of frequency, is normally associated with excitation or de-excitation of vibrational oscillations (as happened historically). There is a well established classical consideration of such a case which consists of the following. Imagine a molecule. If the molecule is motionless then the light incident on it and described by the expression for the electric field strength $\mathbf{E} = \mathbf{E}_l \cos(\omega_l t)$ will build up oscillations of the electron shell in time with its own frequency ω_l and induce an electric polarization $\mathbf{P} = \alpha_0 \cos(\omega_l t)$ (where α_0 is a constant) in the molecule. This polarization will determine the light scattering in all directions with the frequency ω_l of the exciting light. This is Rayleigh scattering. The pic-

[2]This arrangement was developed by V. F. Sapega [33]

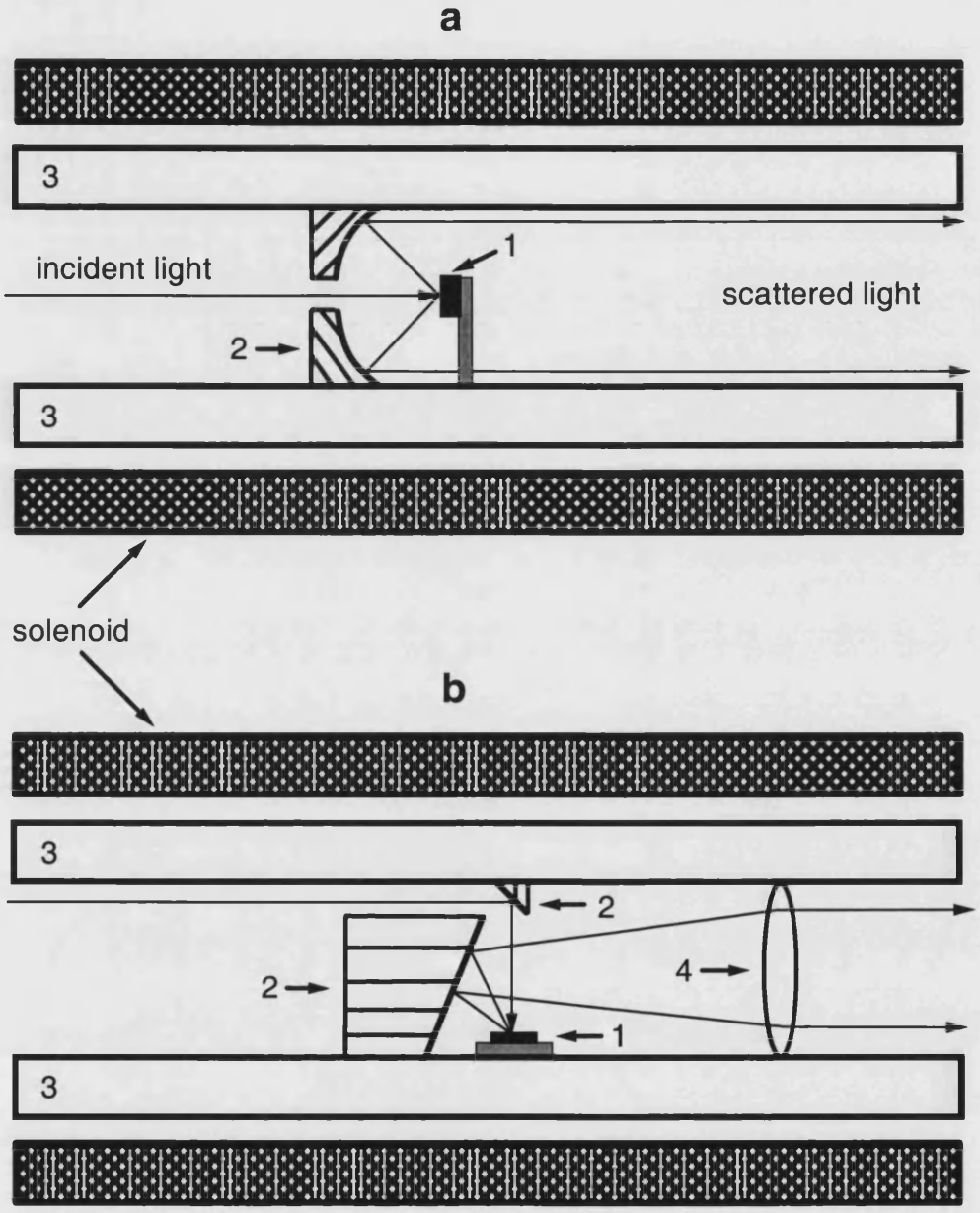

Figure 1.2: Arrangements for the sample inside the superconducting solenoid (Max-Planck Institut für Festkörperforshung, Stuttgart). a) Faraday geometry, 1 - sample, 2 - spherical mirror with a hole, 3 - liquid helium heat-exchanger. b) Voigt geometry, 1 - sample, 2 - flat mirror prisms, 3 - liquid helium heat-exchanger, 4 - lens.

ture described of the interaction between light and a molecule is not a practical case. In reality, the atoms of the molecule will "shake" under the action of thermal motion and for the induced molecular polarization one can write the expression:

$$\mathbf{P}(Q, \omega_l) = \alpha(Q)\mathbf{E}_l \cos(\omega_l t), \tag{1.2}$$

here Q is a generalized coordinate, $\alpha(Q)$ is the molecular polarisability, which is generally a tensor quantity but which we assume for simplicity that it is a scalar. Possible molecular rotation is disregarded.

For small displacements of atoms from their equilibrium position and for sinusoidal atomic oscillations in the molecule, the polarisability can be expanded in a Taylor series as follows

$$\alpha(Q) = \alpha(0) + \frac{\partial \alpha}{\partial Q} \cos(\Omega t + \varphi), \tag{1.3}$$

where φ is an arbitrary phase and Ω is the frequency of the oscillations. Substituting (1.2) into (1.3), we obtain:

$$\mathbf{P} = \alpha(0)\mathbf{E}_l \cos(\omega_l t) + \frac{1}{2}\frac{\partial \alpha}{\partial Q}\mathbf{E}_l \left\{\cos\left[(\omega_l + \Omega)t + \varphi\right] + \cos\left[(\omega_l - \Omega)t - \varphi\right]\right\} \tag{1.4}$$

The intensity and the spectral composition of the scattered light will be determined by the induced polarization (1.4), and it is therefore seen that the lines of frequency ω_l and two more lines – one of frequency $\omega_l - \Omega$ (a Stokes component) and the other of frequency $\omega_l + \Omega$ (an anti-Stokes component) must be present in the scattered light.

In analogy with that described above the classical picture of SFR scattering can be considered as follows. A spin centre precesses at the Zeeman frequency $\Omega_Z = g\mu_B B$ in an external magnetic field. It drags around its electronic charge cloud due to the existence of spin-orbit coupling, leading to that the electronic polarisability being modulated at the same frequency. This classical picture was proposed by Geschwind [30].

The quantum mechanical approach to Raman scattering takes into account that the energy spectrum of an excitation ("shaking" or the vibrational energy of the molecule in the case described above) is quantized. In this approach the first step in a Raman process is the absorption of a photon with energy $\hbar\omega_l$ and momentum

$\hbar\mathbf{k}_l$. This leads to a virtual or real electronic intermediate state $|n>$ which may interact with an elementary excitation of energy $\hbar\Omega$, via a certain mechanism. Then the elementary excitation is created or annihilated. The last step is that the scattered intermediate state recombines emitting a photon of different energy $\hbar\omega_s$ and momentum $\hbar\mathbf{k}_s$. The elementary excitation in this process is therefore either excited or de-excited from an initial quantized state $|i>$ to a final quantized state $|f>$. In SFR scattering this is associated with a change of the spin state. Energy conservation is required for the whole process and the momentum is conserved for each intermediate step so that

$$\hbar\omega_l = \hbar\omega_s \pm \hbar\Omega, \tag{1.5}$$

$$\hbar\mathbf{k}_l = \hbar\mathbf{k}_s \pm \hbar\mathbf{q}, \tag{1.6}$$

where $\mathbf{q}$ is the crystal-momentum of the elementary excitation. These conditions are shown in Fig. 1.3.

In the SFR scattering process which occurs between two spin states $|i>$ and $|f>$ the electric field $E_l \cos\omega_l t$ of the incident laser beam admixes an electronic intermediate state $|n>$ into these states (the corresponding Hamiltonian H_{ep} is given in subsection 1.4.2) so that in first order time dependent perturbation theory the modified states are given [30]

$$|\Psi_i> = \exp(-i\omega_i t - i\varphi)\left(|i> - \sum_n \frac{|n><n|e\mathbf{r}\cdot\mathbf{E}_l|i>}{2(E_n - E_i - \hbar\omega_l)}\exp(-i\omega_l t)\right), \tag{1.7}$$

where $\mathbf{r}$ denotes a space coordinate and e is the electron charge. In this equation the non-resonant term in $\exp(+i\omega_l t)$ has been omitted for simplicity. For the $|\Psi_f>$ state a similar expression is derived but without the phase factor $\exp(-i\varphi)$ which describes the relative phase between the two states $|i>$ and $|f>$. The matrix element $<\Psi_f|e\mathbf{r}|\Psi_i>$ describes the electric dipole emitting Raman radiation at frequencies $\omega_l \mp \omega_{if}$.

1.4.2 Scattering intensity and resonant effect

The Raman scattering intensity is proportional to the probability of the Raman process R. In the case of electron SFR scattering this probability is derived consi-

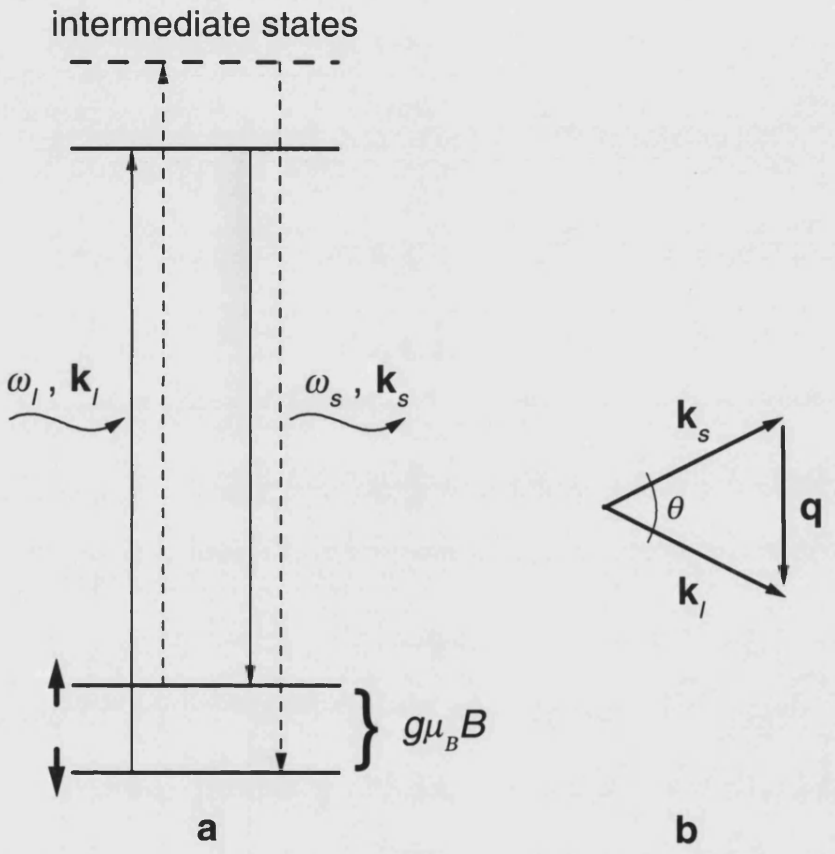

Figure 1.3: a) Energy level diagram to illustrate SFR scattering process described in the text. The small bold arrows indicate the different spin states. The long arrows correspond to the Stokes (solid) and anti-Stokes (dashed) processes. The wavy arrows represent incident and scattered photons. b) Momentum diagram for the scattering angle θ: $\mid \mathbf{q} \mid = \mid \mathbf{k}_l - \mathbf{k}_s \mid = 2 \mid \mathbf{k}_l \mid \sin\theta/2$.

dering the interaction of electrons with photons via a time dependent perturbation theory analysis that gives [22]

$$R = \left[\sum_n \left(\frac{< f|H^s_{ep}|n >< n|H^l_{ep}|i >}{\hbar\omega_l - (E_n - E_i)} - \frac{< f|H^s_{ep}|n >< n|H^l_{ep}|i >}{\hbar\omega_s + (E_n - E_i)} \right) \right]^2, \quad (1.8)$$

where the sum is carried over all intermediate states $|n >$; E_i and E_n are the energy of the initial and intermediate states, respectively; the electron-photon coupling Hamiltonian H_{ep} is given via the electron momentum $\mathbf{p}$ and the vector potential $\mathbf{A}(\mathbf{r})$ of the electromagnetic field by

$$H_{ep} = \frac{1}{2m}\left[\mathbf{p} - \frac{e}{c}\mathbf{A}(\mathbf{r})\right]^2, \quad (1.9)$$

where m is the electron mass. We note here that only the term $\mathbf{p} \cdot \mathbf{A}$ of the Hamiltonian contributes to SFR scattering in the dipole approximation [22].

It is clear from Eq. 1.8 that the scattering probability goes to infinity as the incident photon energy $\hbar\omega_l$ approaches $E_n - E_i$, which corresponds therefore to a resonant condition. A more realistic case of scattering is described by adding to Eq. 1.8 damping terms preventing the denominator going to zero. Nevertheless, in practice such a resonant increase in Raman intensity can be several orders of magnitude. It opens a remarkable opportunity to study particular spin excitations by fine tuning the laser wavelength in resonance with corresponding with them transitions. Chapters 3 and 4 provide examples of the use of this resonant effect.

1.4.3 Polarization selection rules

The polarization selection rules are determined in general by symmetry properties of the interactions involved in a process of Raman scattering. These rules are directly summarized in the form of the Raman tensor $\Re$ - a second-rank tensor with complex components proportional to R of Eq. 1.8. Group-theoretical considerations show that a Raman tensor will have non-zero elements related to a certain polarization geometry of the experiment if the excitation participating in the process transforms according to an irreducible representation of the direct product of the polarization vectors under the point group of the crystal [34]. By a contraction of $\Re$ with the unit electric-field polarization vectors of incident $\mathbf{e}_l$

and scattered $\mathbf{e}_s$ photons the scattering intensity I_s for a particular geometry or the experiment is given as

$$I_s \sim |\mathbf{e}_s^* \cdot \Re \cdot \mathbf{e}_l|^2, \tag{1.10}$$

where $\mathbf{e}_s^*$ is a complex conjugate to $\mathbf{e}_s$.

For SFR scattering of conduction band related states in a system of cubic symmetry Eq. 1.10 can be shown to be [7, 35]

$$I_s \sim |\mathbf{B} \times (\mathbf{e}_l \times \mathbf{e}_s)|^2, \tag{1.11}$$

where $\mathbf{B}$ is the unit vector of the static magnetic field. Consider the case of the Voigt and Faraday backscattering geometries mentioned in Section 1.3. The polarization arrangement for both of these geometries is shown in Fig. 1.4, where $\sigma^+(\sigma^-)$ represent (in the chosen coordinate system) right(left)-hand circular polarization of the light and $\pi(\sigma)$ its linear polarization, so that

$$\sigma^+ = \frac{1}{\sqrt{2}}(x\mathbf{e}_x - iy\mathbf{e}_y), \quad \sigma^- = \frac{1}{\sqrt{2}}(x\mathbf{e}_x + iy\mathbf{e}_y), \quad \pi = -z\mathbf{e}_z, \quad \sigma = \frac{1}{\sqrt{2i}}(\sigma^+ + \sigma^-) \tag{1.12}$$

It is seen from Eq. 1.11 that I_s will be maximum when $\mathbf{e}_l$ is perpendicular to $\mathbf{e}_s$ (crossed polarization) whereas $\mathbf{B}$ must lie in the "xy" plane, thus corresponding to the Voigt geometry (Fig. 1.4). The parallel polarization ($\mathbf{e}_l \parallel \mathbf{e}_s$) will be forbidden in both geometries.

The selection rules for optical transitions between the conduction and valence band states of a direct gap zinc-blende semiconductor are the same as in the case of an atomic dipole-allowed transitions between ground states with $J = 3/2$ ($J_z = \pm 3/2$ or $J_z = \pm 1/2$) and excited states with $J = 1/2$ ($J_z = \pm 1/2$): light of π-polarization does not change the component of angular momentum of the electronic state along the magnetic field ($\Delta m_j = 0$) whereas light of σ-polarization changes it by one unit ($\Delta m_j = \pm 1$). Fig. 1.5 demonstrate the selection rules schematically. The conservation in the scattering process of the sum of the angular momentum components along the magnetic field of all the particles involved demands, therefore, that the incident and scattered light have to have different (crossed) polarization, either π or σ or vice versa. This selection rule is written in a conventional Porto notation [36] as $z(\sigma, \pi)\bar{z}$ or $z(\pi, \sigma)\bar{z}$; z and $\bar{z}$ denote the wave-vector directions of the incident and scattered light. Similar consideration for the backscattering geometry leads to the selection rule for SFR transitions

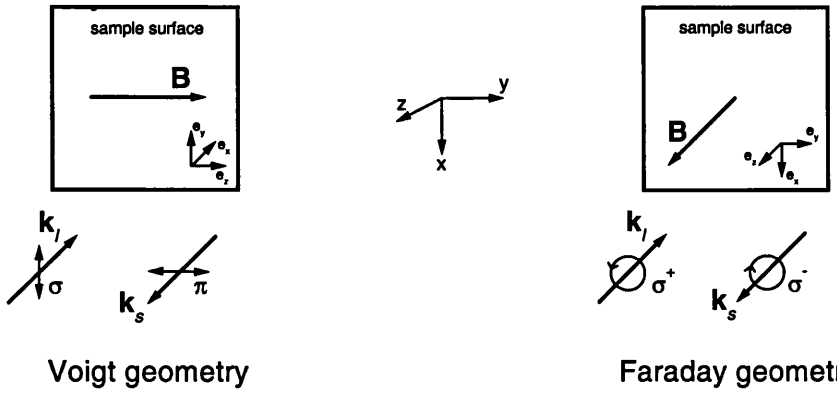

Figure 1.4: Polarization arrangements for the Voigt (electron signal detection) and Faraday (hole signal detection) backscattering geometries corresponding to the SFR selection rules of a system with cubic symmetry (see text).

at valence band related states of $z(\sigma^+,\sigma^-)\bar{z}$ and $z(\sigma^-,\sigma^+)\bar{z}$ and the transition is observed in the Faraday arrangement (corresponding to the Voigt geometry the heavy hole g-factor in a zinc-blende semiconductor is very small by symmetry [37]). We see that, for example bound heavy hole related SFR scattering is forbidden. Under a transition $\pm 3/2 \rightarrow \mp 3/2$, the hole changes the z component of its angular momentum by $\Delta m_j = \pm 3$, whereas for the backscattering geometry, the photon angular-momentum projection either remains unchanged or changes by ± 2. These selection rules strictly hold if (i) the structure has no other imperfections except a substitutional acceptor atom and (ii) electron spin-lattice relaxation or electron-nuclear hyperfine interaction is neglected [38].

We mention finally that a non-zero SFR transition probability may also be produced by the interaction of light with the higher moments of the system (quadrupole etc.). The corresponding transitions are much weaker and will possess their own selection rules.

1.5 Raman scattering or hot luminescence?

Usually in a resonant Raman experiment the excited intermediate state is a real (not virtual) electronic state. The absorption of a photon into such a state may be followed by spontaneous emission from that state aided by the emission or

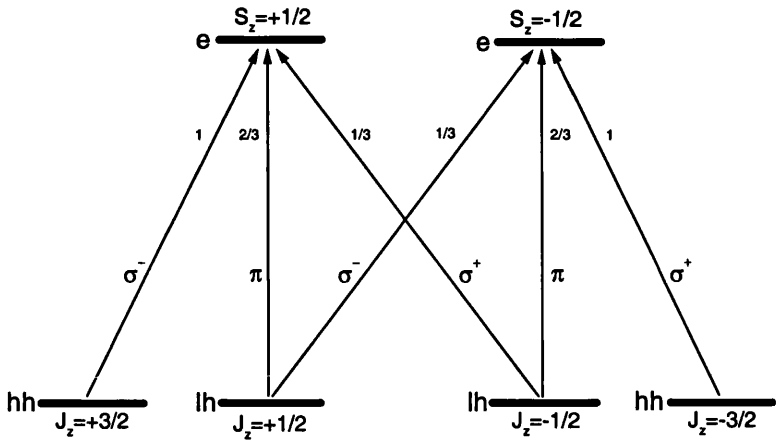

Figure 1.5: Selection rules for the band edge optical transitions in a direct gap zinc-blende semiconductor [39]. e, hh and lh label the electron, heavy hole and light hole energy levels, respectively. The numbers near the arrows correspond to the transition probabilities. The case of $B = 0$ is shown.

absorption of one or more phonons. This is a process of so-called hot (nonequilibrium) luminescence [40]. The spectroscopy of this type of luminescence is very similar to that of resonance Raman scattering and a confusion may arise analyzing experimental data when attempting to distinguishing between these two processes. The first theoretical work on the problem was performed by Klein [41]. It was shown on the basis of the Fermi Golden rule approach that in some cases the resonance Raman scattering efficiency can be written as the product of the absorption coefficient and the quantum yield for hot luminescence emission and a conclusion followed that these two processes are often equivalent and indistinguishable. However, obvious physical differences of the processes can be seen. First, resonance Raman scattering is a two-photon direct process, while hot luminescence is at least two-step process. Second, hot luminescence arises from radiative decay of the excess population pumped into the intermediate state by the excitation, but resonant Raman is not. Using density matrix formalism which takes more correctly into account relaxation or energy broadening due to the effect of random fields (unspecified scattering processes), Shen [42] showed that the scattering probability consists of two terms. One of them is proportional to the number of electrons in the excited intermediate state and can be identified as the hot luminescence part. The other term represent the direct process between the initial and final state and does not depend on how many electrons are excited into the intermediate state. This term is identified as the Raman scattering part. This formal "theoretical" consideration of resonance Raman scattering and hot luminescence as two different physical processes does not always lead to their

"experimental" distinction. These processes are always simultaneously present, and as it was also shown [42], can interfere with each other. In experiments with continuous wave excitation and response, they are not clearly distinguished, except that hot luminescence has a broader spectral width containing the widths of initial and final states. In some cases, the two processes can probably be distinguished in time-resolving experiments, since resonance Raman scattering is essentially an instantaneous two-photon direct process while the hot luminescence is a two-step process which depends on the relaxation of the excess population in the intermediate states [42].

Chapter 2

ZnCdSe-based heterostructures

2.1 Introduction

The need for electro-optical devices for the blue-green spectral region has caused increased attention to be given to wide-gap II-VI semiconductors, in particular to their heterostructures. ZnCdSe-based heterostructures are an important example. The recent advances in the epitaxial growth of this semiconductor material makes it possible to realize the whole range of heterostructures from bulk ZnCdSe epilayers to sophisticated structures containing ZnCdSe-based low-dimensional features - quantum wells, quantum wires and quantum dots. An important type of low-dimensional heterostructure, which contains just a fraction of a monolayer, the so called submonolayer structure, has also been realized; such structures will be discussed in detail in section 2.5. These technological achievements open a remarkable opportunity for researchers to study a variety of topics related not only to the device applications but also to pure physics. The band structure of ZnCdSe and properties of low-dimensional excitons are topics of particular interest.

This chapter introduces semiconductor heterostructures based on ZnCdSe with the purpose of providing information helpful for the presentation of the experimental results given in Chapters 3 and 4. After considering the binary end-members ZnSe and CdSe of the ZnCdSe, as well as the alloy itself, we then consider the heterostructures. Bulk ZnSe, CdSe and ZnCdSe epilayers grown

on the most frequently used substrate of GaAs and low-dimensional systems of ZnCdSe/ZnSe and CdSe/ZnSe, often called the emeralds of the II-VI heterostructure family will be considered. Most attention will be paid to their structural and optical properties. Physical parameters related to ZnSe and CdSe are collected in the table in Appendix A.

2.2 ZnSe and CdSe

ZnSe and CdSe are simple binary compounds composed of elements belonging to groups II and VI of the periodic table of elements. These compounds are grown in the cubic (zinc blende) crystals of the symmetry point group T_d and the hexagonal (wurtzite) structure of the symmetry point group C_{6v}, respectively. These two crystal structures are closely related, both being made up of tetrahedrally bonded atoms (Fig. 2.1). The cohesive energy of the zinc blende structure is very close to that of the wurtzite and as a result some of the group II-VI semiconductors, including ZnSe and CdSe, under appropriate growth conditions can crystallize in both zinc blend and wurtzite structures. Nevertheless, up to now only application of heteroepitaxial techniques allows both forms to be realized.

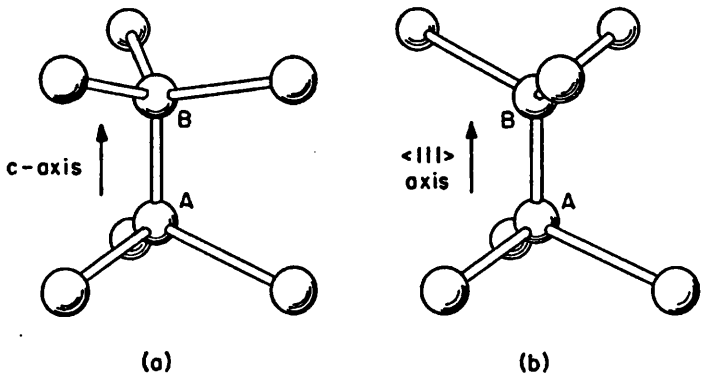

Figure 2.1: Orientations of adjacent atomic tetrahedra in hexagonal (a) and cubic (b). The A and B label the two different types of atom.

Cubic ZnSe and hexagonal CdSe are well studied semiconductors. Both of them are direct gap semiconductors with the smallest energy gap at the Γ point of the Brillouin zone. The lowest conduction band has a single Γ_6 minimum (T_d symmetry) in ZnSe formed by $4s$ states of Zn and a single Γ_7 minimum (C_{6v}

symmetry) in CdSe formed by $5s$ states of Cd. The topmost valence band in ZnSe results from the $4p$ states of Se split due to spin-orbit coupling into a fourfold Γ_8 state with quantum numbers of the angular momentum $J_z = \pm 3/2$ and $J_z = \pm 1/2$ and twofold Γ_7 with $J_z = \pm 1/2$ state. The CdSe topmost valence band is split due to crystal-field and spin-orbit coupling into three spin-degenerate states which are often referred to in the literature as the A, B and C bands in order of decreasing electron energy. The A-band has Γ_9 symmetry and $J_z = \pm 3/2$, while B and C have Γ_7 symmetry with $J_z = \pm 1/2$. Fig. 2.2 demonstrates schematically the ordering of energy states at the Γ point in zinc blend and wurtzite crystals.

A variety of different calculations of the real band structures has been performed for both semiconductors and as an example Fig. 2.3 shows a result of such calculations for cubic ZnSe by the pseudopotential technique.

Unlike cubic ZnSe and hexagonal CdSe, very little information is available on hexagonal ZnSe and cubic CdSe - as mentioned above, they are normally not grown in these modifications. The first attempts to calculate the band structures of these semiconductors were reported in Refs. [43, 44]. Only recently have experimental data related to the band structure of cubic CdSe been obtained on epitaxial layers by means of ellipsometry and low-temperature excitonic spectroscopy. This has allowed much more precise calculations of the cubic CdSe band structure to be performed [45].

2.3 ZnCdSe alloy

ZnCdSe is a pseudobinary (ternary) alloy of the form $A_{1-x}B_xC$, where x is the fractional concentration. This form indicates a cation substituted alloy, which is considered as a result of replacing a fraction x of the cations A(Zn) in the AC(ZnSe) compound by B(Cd) atoms from the same column in the periodical table of elements.

The bulk single crystalline form of this alloy has been investigated intensively for a long period. In particular, it was shown that $Zn_{1-x}Cd_xSe$ alloys have the cubic structure for $x \leq 0.3$, the hexagonal structure for $x \geq 0.5$, and mixed phases for

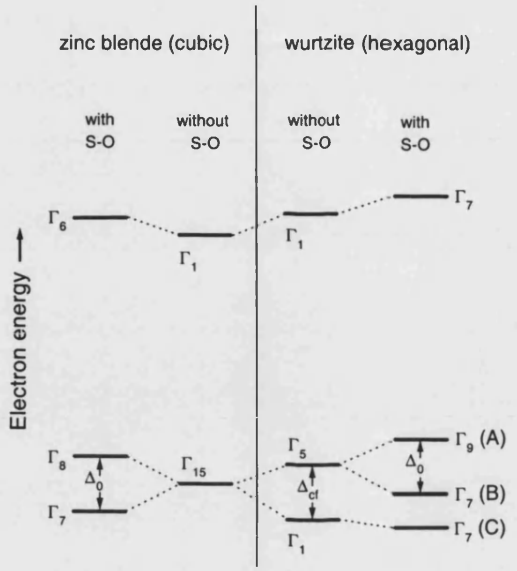

Figure 2.2: Schematic diagram showing evolution and splitting of degeneracies of the electronic energy levels at the Γ point from the cubic structure to the hexagonal; both without and with the spin-orbit interaction (S-O). Δ_0 - spin-orbit splitting, Δ_{cf} - crystal field splitting.

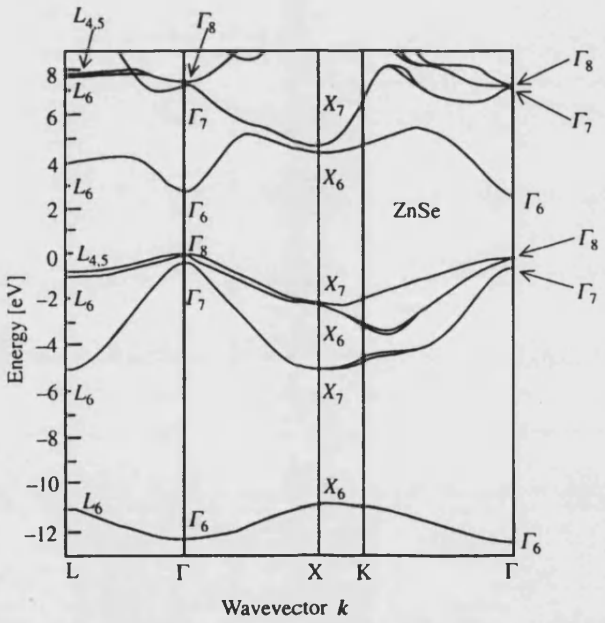

Figure 2.3: Electronic band structure of ZnSe calculated by the pseudopotential technique [46].

$0.3 < x < 0.5$ [47]. The alloy is a direct gap semiconductor for any value of x. As in the case of cubic CdSe there is very little information about the cubic modification of bulk ZnCdSe with $x > 0.3$. However, the situation has improved - it has recently been demonstrated that the growth of $Zn_{1-x}Cd_xSe$ alloys on zinc-blende substrates by molecular beam epitaxy (MBE) can result in single-phase cubic crystalline layers over the entire composition range from ZnSe to CdSe [48].

In general, structural features of a pseudobinary alloy are similar to its constituent binary crystals. For example, the X-ray diffraction pattern of the alloy is similar to those of the pure binary compounds, except that the intensity profile for alloys may have a broader width caused by unavoidable disorder of the crystalline structure. The lattice parameters a_0 determined from X-ray diffraction are found to be well approximated by the concentration weighted average of those of the binary compounds, which is usually described by Vegard's law,

$$a_0 = (1-x)a_0^{\mathrm{AC}} + xa_0^{\mathrm{BC}} \tag{2.1}$$

Alloying studies show that the fundamental band gap E_0 varies quadratically with composition x. According to Hill [49], E_0 can be described by

$$E_0(x) = E_0^{\mathrm{CdSe}} + (E_0^{\mathrm{ZnSe}} - E_0^{\mathrm{CdSe}} - b)(1-x) + b(1-x)^2, \tag{2.2}$$

where b is the bowing parameter. In Hill's theory it is assumed that, for an alloy $A_{1-x}B_xC$, the bowing parameter is not affected by the random potential due to disorder of the crystal, but it is a result of the nonlinear dependence of the crystal potential on the properties of the component ions. Because of the fact that in most II-VI alloys (including ZnCdSe) formed by isoelectronic substitution the disorder-induced potential is weak, this assumption (the so-called virtual crystal approximation) can be considered as a good approximation [50]. The bowing parameter b for the fundamental band gap can be calculated from the equation

$$b = \frac{Ze}{8\pi\epsilon_0}\left[\left(\frac{1}{r_{\mathrm{A}}} - \frac{1}{r_{\mathrm{B}}}\right)^2 (r_{\mathrm{A}} + r_{\mathrm{B}}) \exp\left(-sa_0^m \frac{\sqrt{3}}{8}\right)\right], \tag{2.3}$$

where Ze is the charge of the substituting ions, a_0^m is the lattice constant of the midcomposition alloy ($x = 0.5$), s is the screening constant $s = 0.25$ Å^{-1} [49], and r_{A} and r_{B} are the Pauling covalent radii of elements A and B, respectively. Now we follow the calculations given in Ref. [51]. Using for ZnSe the lattice constant $a_0 = 5.6676$ Å and for cubic CdSe the lattice constant $a_0 = 6.077$ Å

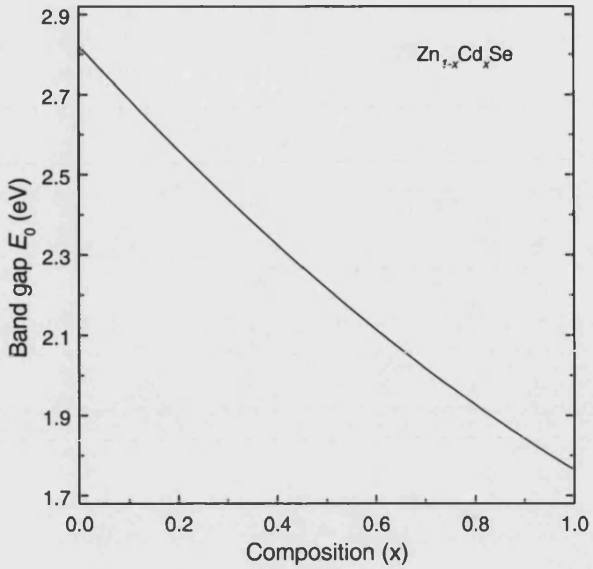

Figure 2.4: Band gap energy of $Zn_{1-x}Cd_xSe$ as a function of alloy composition x.

[52], the lattice constant of the mid-composition is $a_0 = 5.8723$ Å. Using the covalent radii $r_{Cd} = 1.405$ Å and $r_{Zn} = 1.225$ Å, we obtain a bowing parameter $b = 0.301$. For higher band gaps the magnitude and even the sign of the bowing can change [53]. Fig. 2.4 shows the composition dependence of the fundamental band gap for $Zn_{1-x}Cd_xSe$. This dependence was computed by taking the liquid helium temperature values of the fundamental band gaps for ZnSe of 2.821 eV and for cubic CdSe of 1.764 eV. The cubic CdSe value used was determined from excitonic reflectance measurements in the present work (see Chapter 3).

Below, some results related to phonon Raman scattering and excitonic photoluminescence (PL) are provided. Phonon Raman and excitonic spectroscopies of semiconductor alloys provide rich information on their structural properties and quality. These techniques are also often used by growth technologists for determining alloy composition. Moreover, investigation of excitonic PL is a necessary prerequisite for resonant SFR studies (therefore being of special importance for the present work) - excitons may participate in a SFR scattering process forming intermediate states.

Fig. 2.5 demonstrates the results of Valakh et. al. [54] obtained on bulk high quality ZnCdSe crystals in a standard 90°-scattering geometry (the wave vectors of incident and scattered light are perpendicular to each other). It was shown that in $Zn_{1-x}Cd_xSe$ crystals the LO-phonon spectrum versus crystal composition is the

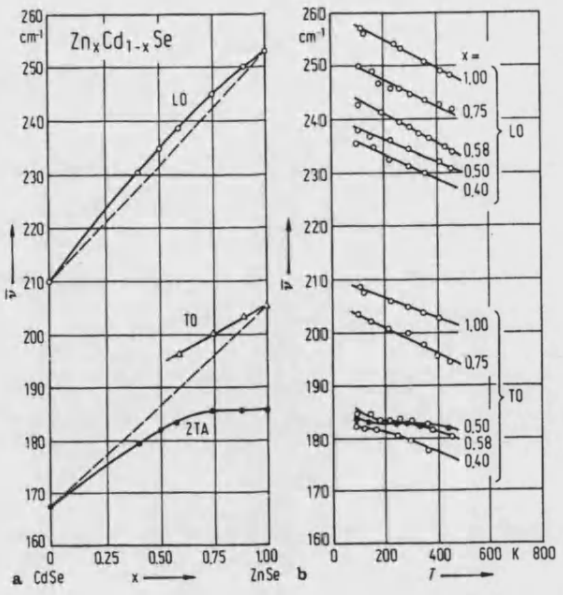

Figure 2.5: $Zn_{1-x}Cd_xSe$. Raman wavenumbers vs. composition (a) and vs. temperature for various compositions (b) [54].

"one mode" type. The LO-phonon frequency decreases from the ZnSe value to the CdSe one. The TO-phonon exhibits anomalous features in the dependences of line shape and TO-mode frequency on crystal composition as well as on temperature; these features are interpreted in terms of the anharmonic resonance coupling between the TO-mode and two phonon states of TA phonons.

In the PL spectra of good quality bulk binary compounds ZnSe ($x = 1$, cubic) and CdSe ($x = 0$, hexagonal) near the absorption edge at liquid helium temperature, the emission lines I_2 (exciton bound at a neutral donor) and I_1 (exciton bound at a neutral acceptor) prevail. Weaker free exciton emission is also observed. As was mentioned above, in II-VI alloys with substitution in the cation sublattice the effect of disorder is weak. Localization of excitons by alloy potential fluctuations influences recombination process only weakly. Bound exciton emission is dominant in the low-temperature PL spectra of bulk high quality $Zn_{1-x}Cd_xSe$ crystals over the entire range of compositions, with a weak indication of emission due to localized excitons [47, 50]. As the composition x is increased the linewidth of an excitonic transition is broadened due to the effect of disorder. It leads to a strong overlapping of the emission lines corresponding to different excitonic transitions. Thus the most general structure dominating the near edge PL spectrum of mid-compositional ZnCdSe is a single asymmetric band formed

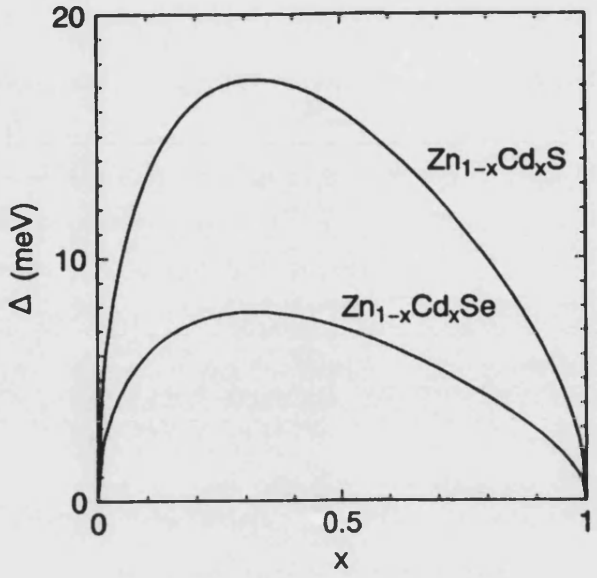

Figure 2.6: Theoretical values of disorder-induced broadening of exciton linewidth in $Zn_{1-x}Cd_xSe$ and $Zn_{1-x}Cd_xS$ [55].

in different intensity proportions by the I_2 and I_1 transitions. The relative intensity of these transitions may vary remarkably in different samples with the same x because the corresponding concentrations of impurities donors and acceptors are uncontrollable. Nevertheless, the I_2 transition prevails in most of the cases.

In Ref. [55] the effect of disorder on the broadening of exciton linewidth was estimated. The full width at half maximum (FWHM) of an exciton line $\Delta(x)$ in an $A_{1-x}B_xC$ alloy due to disorder is given by the equation from Ref. [56]:

$$\Delta(x) = 2\sqrt{2\ln 2}\,[dE_{ex}(x)/dx]\,\sqrt{x(1-x)V_0(x)/V_{ex}(x)} \tag{2.4}$$

where a Gaussian line shape is assumed, $E_{\mathrm{ex}}(x)$ is the exciton transition energy, which depends on concentration x, $V_0(x)$ is the volume of the elementary cell, and $V_{ex}(x)$ is that of the exciton. Zimmermann [57] has derived the relevant exciton volume using a statistical theory expressed by

$$V_{ex}(x) = 8\pi r_{\mathrm{B}}^3(x), \tag{2.5}$$

where r_{B} is the Bohr radius of the exciton. The dependence $\Delta(x)$ is shown in Fig. 2.6. The dependence was obtained using $r_{\mathrm{B}} = 43.4$ Å and 33.0 Å for CdSe and ZnSe, respectively and its linear variation with x. It shows also the compositional

broadening for $Zn_{1-x}Cd_xS$ alloys, which is almost two times larger than in case of $Zn_{1-x}Cd_xSe$ due to the smaller exciton Bohr radius in the latter material.

2.4 Bulk epitaxial layers

One of the major factors which determines the structural quality of epitaxial layers is the lattice mismatch between the layer and the substrate. For epitaxial ZnSe grown on a widely available and relatively cheap (100) oriented GaAs substrate, the lattice mismatch

$$f = \frac{a_0^{\mathrm{GaAs}} - a_0^{\mathrm{ZnSe}}}{a_0^{\mathrm{ZnSe}}} \tag{2.6}$$

at the usual growth temperature of about 620 K is $f = -0.31\%$ [58]. This lattice mismatch leads to a strain in the thin layer material, whereas the substrate remains unstrained. The strain of the layer at room temperature or at liquid helium temperature

$$\epsilon_{\mathrm{biax}} = \epsilon_{\mathrm{res}} + \epsilon_{\mathrm{therm}} \tag{2.7}$$

is caused by the residual strain at growth temperature ϵ_{res} and the thermal strain $\epsilon_{\mathrm{therm}} = (\alpha_{\mathrm{ZnSe}} - \alpha_{\mathrm{GaAs}})\Delta T$ [59], which is due to the different thermal expansion coefficients α of ZnSe and GaAs ($\epsilon_{\mathrm{therm}} = +0.04\%$ and $+0.1\%$ at $T = 620$ K $\rightarrow$ 300 K and $T = 620$ K $\rightarrow$ 2 K, respectively). For layers that are thinner than the critical thickness (see below), the strain at the growth temperature is determined by the lattice mismatch of substrate and layer material ($\epsilon_{\mathrm{res}} = 0.31\%$). Therefore a constant strain of $\epsilon_{\mathrm{biax}} = -0.27\%$ is observed at the room temperature and $\epsilon_{\mathrm{biax}} = -0.21\%$ at $T = 2$ K, respectively.

At the so-called critical thickness the strain starts to relax by the nucleation of misfit dislocations during growth. There are two layer thicknesses which are referred to as the critical thickness. The first is denoted h_{cd} and is defined by Matthews and Blakeslee [60] to correspond to the formation of the first misfit dislocation and this process can be observed using X-ray topography [61]. The second value is denoted as h_{cp} and is defined as the threshold thickness above which long-range lattice relaxation is observed as a change in interplanar spacing by high-resolution X-ray diffraction. The exact value of both of the critical thicknesses depends on growth conditions. For ZnSe epilayers grown directly on to

Table 2.1: Critical thickness in nm for ZnSe and $Zn_{1-x}Cd_xSe$ layers with different x [61].

x	h_{cd}	h_{cp}
0(ZnSe)	97	150
20	12.8	20.2
25	10.1	16.0
30	8.2	13.0
35	6.9	10.9

(100) GaAs substrates by conventional MBE the accepted value for h_{cp} is 150 nm and for h_{cd} is 97 nm [61]. At a thickness of 0.5 μm, the strain is largely reduced. 1-μm-thick layer are unstrained at room temperature [58].

In the case of ZnCdSe grown on (100) GaAs the critical thickness is expected to be smaller for samples with larger Cd content due to the larger Cd atom radius compare to Zn. In Table 2.1 from Ref. [61], estimated values of the critical thicknesses are given for ZnCdSe/GaAs alloys of increasing Cd composition. These values are obtained by scaling theoretical calculations to match the experimental values h_{cd} and h_{cp} of ZnSe/GaAs. To determine the strain of the layer material, it is necessary to perform X-ray diffraction measurements for different asymmetrical Bragg reflections like (224) and $(\overline{2}\overline{2}4)$. Then the strain of the layers can be calculated from the angular difference between the substrate and the layer peaks [62].

Information concerning the strain and its evolution with the thickness of the epitaxial layers can also be obtained by phonon Raman spectroscopy [63]. For example, the observed variation of the ZnSe LO phonon frequency with the thickness of the ZnSe epilayer grown on GaAs is explained well by the strain due to the lattice mismatch between these two semiconductors. It has been calculated that a change of 0.3% of the ZnSe lattice constant will lead to the ZnSe LO frequency shift of about 1 cm^{-1} ($\sim$ 0.12 eV).

As mentioned above, the growth of $Zn_{1-x}Cd_xSe$ alloys on zinc-blende substrates by molecular beam epitaxy (MBE) can result in single-phase cubic crystalline layers over the entire composition range from ZnSe to CdSe, despite natural preference for ZnCdSe alloys with $0.5 < x < 1$ and CdSe itself to form the hexagonal structure. The first successful attempt of growing cubic CdSe epilayers on (100)

GaAs substrates by MBE was reported in Ref. [52]. Reflection high energy electron diffraction (RHEED), X-ray diffraction, transmission electron microscopy (TEM) and excitonic reflectivity measurements showed the resulting epilayers to be of good structural quality, despite the lattice mismatch of 7% between epilayer and substrate. The lattice constant of cubic CdSe was determined to be 6.077 ± 0.0005 Å. Also in that work the in-plane lattice parameter was calculated from the X-ray data to be 6.078 ± 0.001 Å for the epilayers with thicknesses ranging from 0.2 μm to 4 μm. These result suggest that at least for this range of thicknesses, within experimental resolution, the CdSe lattice was not tetragonally distorted. It also indicates that well-matched substrates for epitaxial growth are ZnTe ($a_0 = 6.089$ Å), GaSb (6.096 Å), InAs (6.058 Å), and HgSe (6.085 Å).

Fig. 2.7 (a) shows the result of X-ray diffraction measurements taken on ZnSe and ZnCdSe ($x = 0.61$) of the cubic phase grown on (100) GaAs. As is seen, the full width of the intensity contour increases from 0.25 degrees for $x = 0$ to 0.7 degrees for $x = 0.61$. This broadening is a result of increasing influence of disorder (as in bulk ZnCdSe) as x increases and, as was shown by TEM, an increasing density of stacking faults. The result of X-ray measurements taken on CdSe grown on (100) InAs is shown in Fig. 2.7 (b) (note the absence of a signal around $2\theta_{Br} = 52^o$ corresponding to the hexagonal phase [64]). In this case the width of the intensity contour is about 1.5 times broader than that of ZnSe. This can be due to at least two reasons. First, the lattice mismatch for the ZnSe/GaAs system is *better* than that for the CdSe/InAs system (although the difference is only about 0.1%). Second, the growth conditions for the CdSe/InAs system at present are not so well established as they are for the ZnSe/GaAs one.

2.5 Low-dimensional systems

2.5.1 ZnCdSe/ZnSe

In the ZnCdSe/ZnSe system (we consider the most common case of (100) ZnSe), the bulk ZnCdSe has the smallest fundamental band gap for any Cd content (see section 2.3). A layer of ZnCdSe with thickness of several tens of Ångströms acts as a two dimensional (2D) quantum well with band-to-band profile of type I for

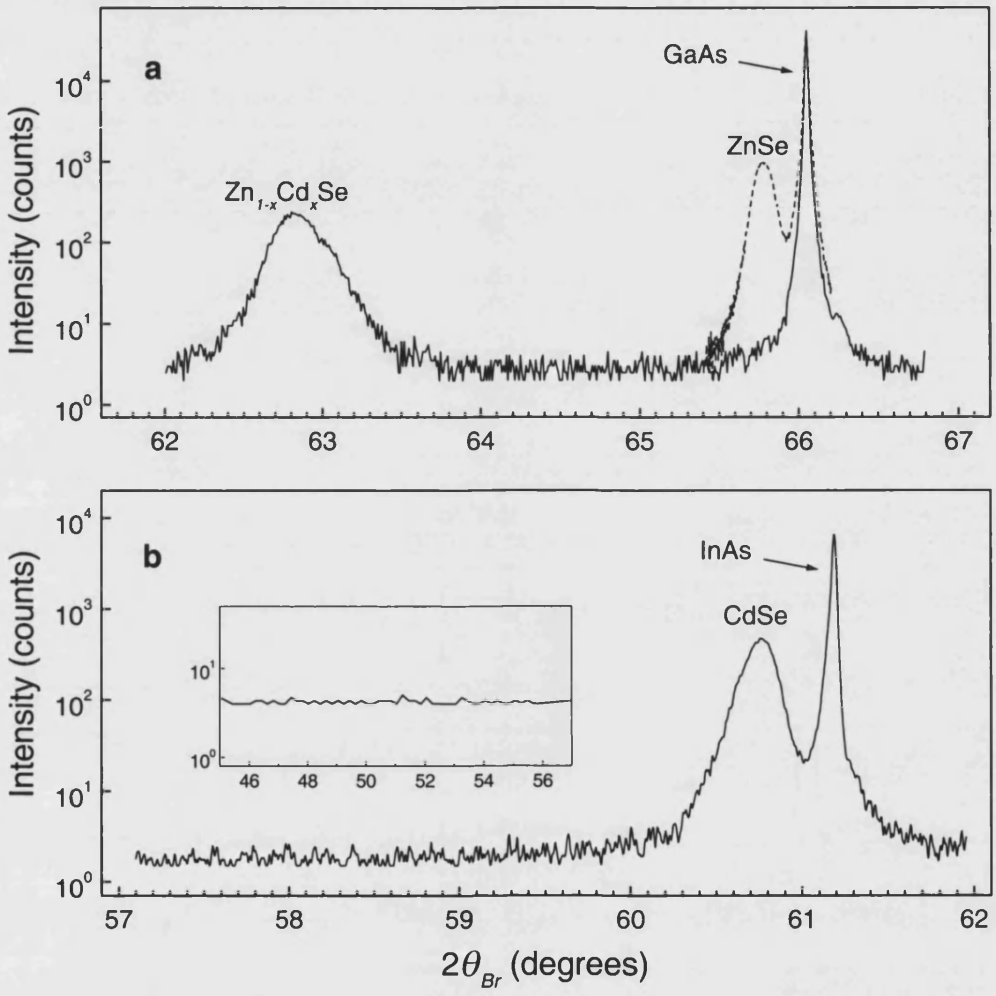

Figure 2.7: X-ray double rocking diffraction pattern from the epilayers of the cubic modification of ZnSe (dotted line) and $Zn_{1-x}Cd_xSe$ ($x = 0.61$) grown on (100) GaAs (a) and of CdSe grown on (100) InAs (b). The thickness of each epilayer is ~ 1 μm. The inset demonstrates the absence of a signal around $2\theta_{Br} = 52^o$, which would indicate the presence of the hexagonal modification in the CdSe epilayer.

the charged carriers when it is embedded between two ZnSe layers (barriers). It also has the largest lattice parameter, leading to ZnCdSe QWs with thicknesses below the critical thickness being strained. It is assumed that the QW is pseudomorphic i.e. its in-plane lattice parameter is completely adapted to that of (much thicker) ZnSe. This is a good assumption for ZnCdSe QWs with relatively low Cd composition ($x \leq 0.25$), which is the case of importance for blue-green opto-electronic devices. At higher x and when the thickness of a particular QW exceeds the critical thickness for the ZnCdSe/ZnSe heteropair, the structural and therefore optical quality of the QW layer deteriorates. Everything that follows below in this subsection concerns the pseudomorphic ZnCdSe/ZnSe QWs.

It is well known that elastic strain changes the width of the band gap and therefore also the potential barrier in the QW. In the particular case of a pseudomorphic QW the stress can be considered as a superposition of a hydrostatic deformation and a shear deformation (in our case we have uniaxial compressive strain) [65, 66]. The hydrostatic deformation changes the difference of the conduction- and valence-band centres of gravity (ΔE^{hy}) by the amount

$$\Delta E^{hy} = 2a_{hy}\left(1 - \frac{C_{12}}{C_{11}}\right)\left(\frac{a_0^b}{a_0} - 1\right), \tag{2.8}$$

where a_0 and a_0^b are the lattice parameters of the unstrained QW and the barrier, respectively, C_{11} and C_{12} are the elastic stiffness components of the QW material, and a_{hy} is the hydrostatic deformation potential for the fundamental band gap. In contrast, shear stress affects only the valence band and the change in the energy position of the heavy- and light-hole (lying at a lower energy) bands is different because of the difference in their symmetry properties. This effect leads to an additional splitting of the Γ_8 heavy- and light-hole levels compared to the quantum confinement effect, which also is affected (reduced) by the interaction of the light-hole and the Γ_7 spin-orbit split-off band. The changes in the energy position of the heavy-hole band (ΔE_h^{sh}) and the light-hole band (ΔE_l^{sh}) are determined by

$$\Delta E_h^{sh} = \delta E^{sh}, \tag{2.9}$$

$$\Delta E_l^{sh} = \frac{1}{2}\left[\Delta_0 - \frac{1}{2}\delta E^{sh} - \sqrt{(\Delta_0 + \delta E^{sh})^2 + 8(\delta E^{sh})^2}\right], \tag{2.10}$$

where Δ_0 is the (unstrained) spin-orbit splitting and

$$\delta E^{sh} = -b_{sh}\left(1 + 2\frac{C_{12}}{C_{11}}\right)\left(\frac{a_0^b}{a_0} - 1\right), \tag{2.11}$$

where b_{sh} is the shear deformation potential. Thus the effective band gap in the QW for the heavy ($E^h_{0,w}$) and the light ($E^l_{0,w}$) holes is given as

$$E^{h(l)}_{0,w} = E_{0,w} + \Delta E^{hy} + \Delta E^{sh}_{h(l)}, \tag{2.12}$$

where $E_{0,w}$ is the band gap of the unstrained QW material. The corresponding band offsets for electrons (U_e), heavy (U_h) and light (U_l) holes are given as

$$U_e = (1 - Q_h)(E_{0,b} - E^h_{0,w}), \tag{2.13}$$

$$U_h = Q_h(E_{0,b} - E^h_{0,w}), \tag{2.14}$$

$$U_l = E_{0,b} - E^h_{0,w} - U_e, \tag{2.15}$$

Here $E_{0,b}$ and Q_h are the band gap for unstrained barrier material and the relative valence-band offset for the heavy hole, respectively. The quantity Q_h is defined as

$$Q_h = \frac{V_h}{E_0^{ZnSe} - E_0^{ZnCdSe}}, \tag{2.16}$$

where V_h is a potential discontinuity affecting the heavy hole. The dependence on Cd composition x of V_h as well as for corresponding electronic V_e and light-hole V_l values are not very well established at present. However, for $x < 0.25$ good fits of the experimental data obtained by means of photoreflectance and photoluminescence spectroscopy have been obtained by using linear dependences $V_e(x) = 925x$ (meV), $V_h(x) = 435x$ (meV) and a weakly non-linear dependence $V_l(x) = 55x + o(x^2)$ (meV) [67]. Thus, for example, we found $Q_h \sim 0.33$ for a QW with $x = 0.1$.

Fig. 2.8 shows as an example the result of the standard calculations from Ref. [68] of the energy level dispersion for a ZnCdSe/ZnSe QW. The calculation procedure was based on the use of the four-band strain Hamiltonian developed by Bir and Pikus

$$\begin{aligned} H_{BP} &= D_d(\epsilon_{xx} + \epsilon_{yy} + \epsilon_{zz}) \\ &+ \frac{2}{3}D_u\left[\left(J_x^2 - \frac{1}{3}J^2\right)\epsilon_{xx} + c.p\right] \\ &+ \frac{4}{3}D'_u[\{J_x, J_y\}\epsilon_{xy} + c.p.], \end{aligned} \tag{2.17}$$

which is added to the kinetic energy Hamiltonian of Kohn and Luttinger written

in the matrix form with:

$$P = \gamma_1(k^2 - K_z^2)/2, \qquad Q = \gamma_2(k^2 - 2k_z^2)/2,$$

$$R = \sqrt{3\gamma_2}(k_x^2 - k_y^2)/2, \qquad S = J\sqrt{3\gamma_3}(k_x - jk_y)k_z,$$

as

$$H_{KL} = \begin{pmatrix} P+Q & R & -S & 0 \\ R^* & P-Q & 0 & S \\ -S^* & 0 & P-Q & R \\ 0 & S^* & R^* & P+Q \end{pmatrix}, \tag{2.18}$$

Here D_d, D_u and D'_u are deformation potentials of the valence bands in Bir and Pikus notation; D_d is the hydrostatic potential and D_u, D'_u are shear potentials determining the valence band splitting for axial $< 100 >$ and $< 111 >$ strain, respectively, *c.p.* stands for circular permutations, indexed ϵ, the strain tensor components; γ_1, γ_2 and γ_3 are the Luttinger parameters; $k = \sqrt{k_x^2 + k_y^2}$ and k_z are the components of the wavevector $\mathbf{k}$ (z denotes the direction perpendicular to the QW plane); J the $\frac{3}{2}$-angular momentum operator[1]. At each heterointerface the continuity of the wavefunction and of the current of probability should be kept.

The calculations show that for the light-hole the confining potential is marginal (type I) and for some Cd compositions, the edge of the light-hole band can even lie at a lower energy in the ZnCdSe QW than in the ZnSe barrier ($U_l < 0$). In this case there is no localizing potential for the light-hole, meaning that a type II QW is realized and a transition will occur from an electronic level into a barrier state.

The heavy hole is confined rather well for all x. In Fig. 2.9 from Ref. [66] a semi-empirically computed dependence of the $1e - 1hh$ optical transition (at temperature of 2 K) on Cd content and the QW width is shown. The energy levels ε in the potential wells were determined from the transcendental equation

$$\pm\left(\sqrt{\frac{m_w}{m_b}(V-\varepsilon)}\right)^{\pm 1} = \tan\left(\sqrt{\frac{m_w\varepsilon}{2}}\frac{L}{\hbar}\right), \tag{2.19}$$

where the plus(minus) signs correspond to odd(even) energy levels, m_w and m_b

[1]{ab}=(ab+ba)/2.

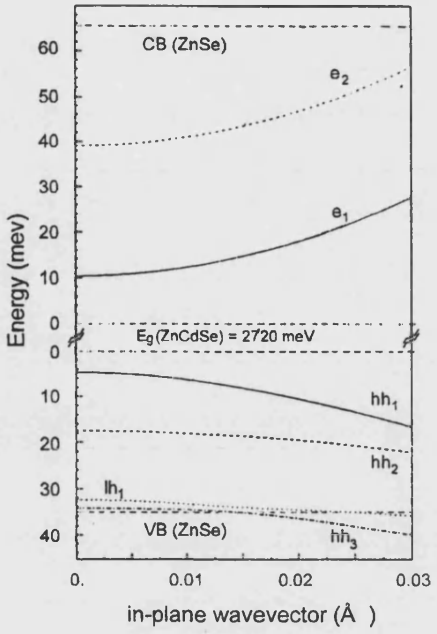

Figure 2.8: Dispersion relations for the conduction and valence states in a 100 Å wide ZnCdSe/ZnSe QW (Cd content $x = 0.075$) as a function of the in-plane $< 10 >$ wavevector [68].

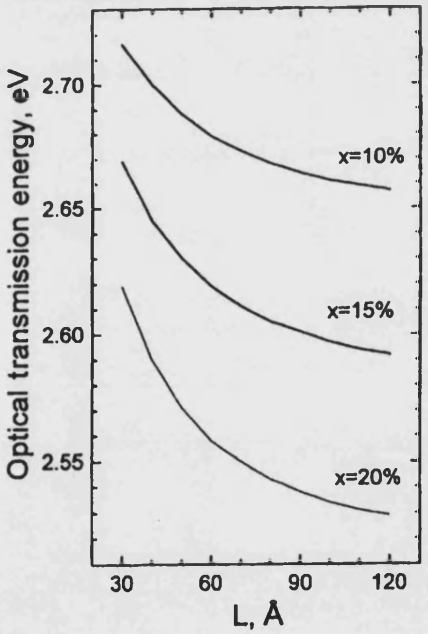

Figure 2.9: Computed energies of optical transitions with participation of heavy hole as a function of the QW thickness for different compositions [66].

are the effective masses of particles in the QW and barrier, respectively (the spatial anisotropy of the masses was disregarded in these calculations), V stands for the height of the corresponding potential barrier for electrons and holes (V_e, V_h, V_l), and L is the thickness of the QW layer. The optical transition energy $\hbar\omega$ is then

$$\hbar\omega = E_{0,w}^{eff} + \varepsilon_e + \varepsilon_{h(l)} - E_x, \tag{2.20}$$

where E_x is the exciton binding energy. As it is seen from Fig. 2.9 even a small change in the Cd composition results in a large change in the transition energy, while the dependence of the transition energy on the thickness of the QW is more weakly affected. In these calculations, E_x for the heavy hole exciton of 30 meV was employed; the dependences of the exciton binding energy on Cd composition and on thickness of the QW were ignored for simplicity.

The value E_x may vary strongly due to the quantum confinement effect. In the particular case of the heavy hole exciton it varies from $\sim$ 20 meV for bulk material to values $\sim$ 40 meV for QWs less than 50 Å thick. In Fig. 2.10 we demonstrate the result of self-consistent variational calculations of E_x for the heavy hole excitons in ZnCdSe/ZnSe QWs [69]. For these calculations an excitonic trial wavefunction of two variational parameters (α and λ) has been used

$$\chi(\rho, z, \alpha, \lambda) = N \exp[-f(\rho, z, \alpha)/\lambda], \tag{2.21}$$

where x, y and z are single particle coordinates, $\rho = \sqrt{(x_e - x_h)^2 + (y_e - y_h)^2}$ and $z = z_e - z_h$ are the electron-hole distances in the QW plane and perpendicular to it, respectively, and $f(\rho, z, \alpha) = \sqrt{\rho^2 + \alpha^2 z^2}$. N is a normalization factor obtained from the square root of

$$N^2 = \left(\frac{\lambda^2}{4}\right) \int_{-\infty}^{+\infty} \chi_e^2 \mathrm{d}z_e \int_{-\infty}^{+\infty} \chi_h^2 \mathrm{d}z_h \left(1 + \frac{2\alpha|z|}{\lambda}\right) \exp\left(\frac{-2\alpha|z|}{\lambda}\right), \tag{2.22}$$

where $\chi_e(\chi_h)$ are the envelope functions of the confined electrons(holes) (Fig. 2.11). Applying the Hamiltonian including the excitonic effect to this wavefunction and then solving the corresponding Schrödinger equation enables E_x to be determined. This is the most general way for such computations, which depending on the degree of sophistication may include additional effects such as band mixing, mismatch of dielectric constants in the QW and barrier, etc.

Lastly we note that: (i) under certain conditions the energy of the LO phonon

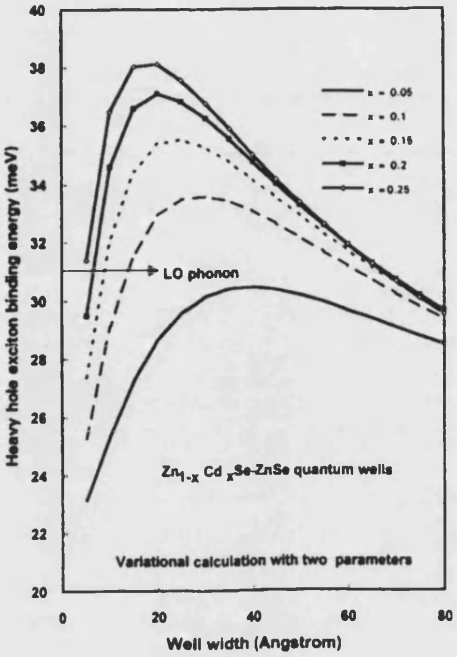

Figure 2.10: Heavy hole binding energies in ZnCdSe/ZnSe QWs. The calculations are made using a two-parameter excitonic trial function [69].

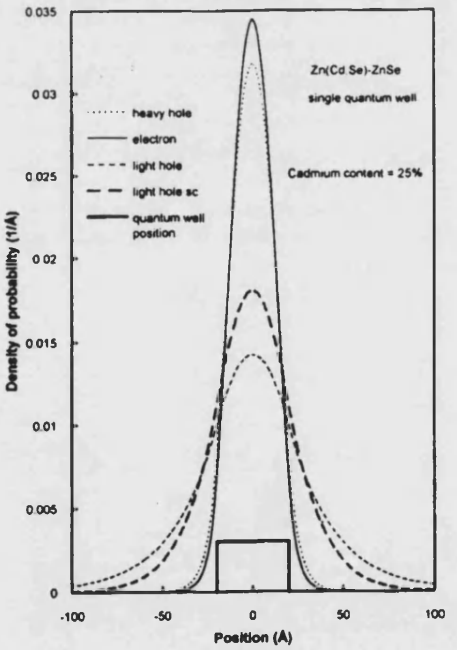

Figure 2.11: Single particle envelope functions for a 40 Å wide ZnCdSe/ZnSe QW. For the light hole the envelope function obtained with and without (light hole sc) influence of the electron density of charge [69].

in ZnCdSe/ZnSe QW structure may be exceeded by the exciton binding energy and therefore the absorption of a LO phonon can not dissociate the exciton into free electron and hole, (ii) the heavy hole exciton binding energy may also exceed the room temperature kT energy leading to the existence of excitonic PL at this temperature. Obviously, both of these features make ZnCdSe/ZnSe QW system attractive for opto-electronic applications.

2.5.2 CdSe/ZnSe

Since the first report of epitaxial growth of CdSe QWs on (100) ZnSe [70], this heterosystem has attracted much attention. The early papers focused mainly on growth and studies of structures containing QWs and superlattices with integer numbers of CdSe monolayers (ML). Then the focus was shifted to epitaxial growth of CdSe/ZnSe self-organized quantum dots (QD) due to certain similarities of this heteropair to the very well studied InAs/GaAs system, which allows formation of InAs QDs in a GaAs matrix. Both of the systems possess type I band alignment and both of the systems have a large lattice mismatch of $\sim$ 7%, which is the driving force for the QD self-organization. In particular, the realization of the Stranski-Krastanov (SK) growth mode for CdSe/ZnSe system has been reported [71].

It is considered that the SK growth mode consists of two phases. In the case of CdSe/ZnSe system the first phase is a 2D growth of a strained homogeneous wetting layer of ZnCdSe alloy. The second phase results in the formation on top of the wetting layer of relatively large three-dimensional (3D) CdSe dots. The 2D $\rightarrow$ 3D transition occurs when a critical thickness t_{cr} of the CdSe layer grown on ZnSe surface exceeds $\sim$ 3 ML ($\sim$ 10 Å). A typical diameter of these dots is 20 - 50 nm - much larger than the exciton Bohr radius in CdSe ($\sim$ 4 nm). Thus these dots do not provide efficient three-dimensional quantum confinement - the case of a great interest for fundamental physics and applications. This fact stimulated studies of self-organization of localized sites comparable with the exciton Bohr radius in the structures containing just a few MLs (less than t_{cr}) or noncomplete MLs of CdSe deposited on the ZnSe matrix surface. The latter are called submonolayer (SML) or fractional monolayer structures. Such structures provide already a basis to study many fundamental phenomena from exciton localization to optical anisotropy effects. Also they have great potential

for applications. For example, it has already been demonstrated that there occur a very low threshold and an enhanced degradation stability for an optically-pumped laser of a conventional design, when a single CdSe SML was used as an active region instead of a "normal" QW [72]; the achieved threshold was 5 times lower than obtained with ZnCdSe-based QW lasers.

The intrinsic morphology of the CdSe/ZnSe SML is an important point to investigate. It was considered originally that a homogeneous layer of ZnCdSe alloy formed at the CdSe/ZnSe interface as a result of Zn/Cd interdiffusion [73]. However, recent investigations reveal a more complicated structure of the SMLs. Beside the alloy-like phase, SMLs may include also planar CdSe-rich islands with a uniform thickness ranging from 1 ML to up to several MLs and a lateral size comparable with the exciton Bohr radius. The average Cd composition in the islands amounts to 40% whereas the Cd content in the ZnCdSe layer between the islands is at least a factor of two lower - such a structure, has been observed by high resolution transmission electron microscopy (HRTEM) in Ref. [74] when investigating 0.7 MLs CdSe/ZnSe structure. Fig. 2.12 shows a colour-coded map of the total atomic displacement in the vertical [100]-direction obtained by a computer analysis of HRTEM data of Ref. [74]. The island-like regions corresponding to large Cd content are clearly seen (shown by arrows). From this HRTEM study the average thickness of 4 MLs for the Cd-rich islands was determined. This is an upper limit because steps in the HRTEM imaging direction may also lead to a contrast broadening.

Although the formation of nanoscale islands under SML growth mode is an established fact, their *electronic* structure is still debated. Up to now the current view is that these CdSe islands are still not electronic QDs, but rather 2D-islands of ultra-thin QWs with a specific carrier/exciton localization potential resulting from the local Cd content and/or thickness fluctuations. Thus the better performance of the CdSe/ZnSe SML lasers compared to ordinary ZnCdSe/ZnSe QW lasers can be explained not by the superiority of electronic properties of proper QDs, but by the proposal that the CdSe islands may serve as efficient localization and recombination centres for the nonequilibrium carriers, preventing their migration toward defect regions, where they could recombine nonradiatively. More studies are needed to understand the nature of the confinement in these islands as well as their real sizes.

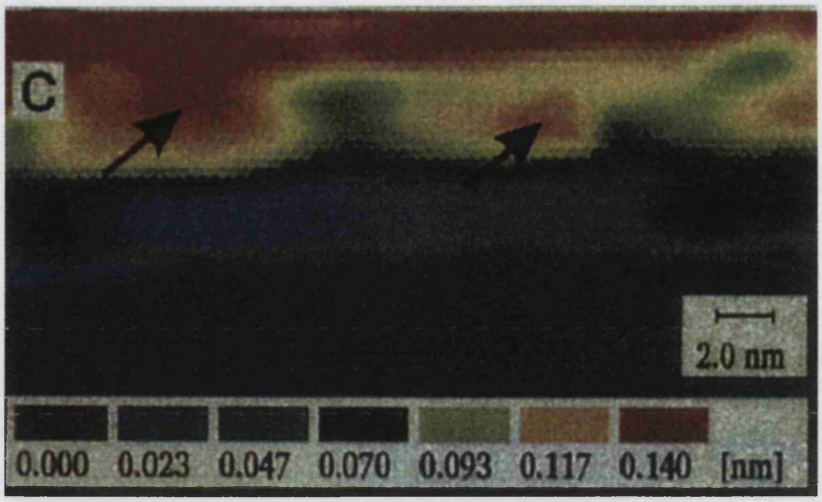

Figure 2.12: The result of HRTEM study from Ref. [74] of a 0.7 SML CdSe/ZnSe structure. The colour-coded map shows the total atom displacement with respect to the underlying ZnSe lattice. The regions with increased displacement are located directly above the regions with larger Cd content indicated by the arrows. The effect originates from a bowing of the (100)-lattice planes in the [100] direction which is caused by the underlying regions of increased tetragonal distortion.

Apart from practical applications, the scaling properties of 2D island size distribution are of fundamental interest and are known for SML epitaxy. According to the scaling theory of Bartelt and Evans [75], the island distribution is given by

$$n_s = \frac{\theta}{< s >^2} f(s/ < s >), \tag{2.23}$$

where n_s is the number of islands (normalized by the number of lattice sites) which contain s atoms, θ is the fractional surface coverage, $< s >$ is the average number of atoms in an island, and $f(x)$ is the scaling function depending only on $s/ < s >$. This scaling relation was confirmed experimentally in InAs/GaAs heteroepitaxy [76].

A remarkable phenomenon related to the self-organization of nanoscale objects in highly strained semiconductor systems is that these objects may form a periodically ordered structure with a periodicity much larger than the lattice parameter. The spontaneous formation of periodically ordered domain structures in solids is a known phenomenon [77]. There are two distinct possibilities. (i) equilibrium domain structure can be formed in so called closed systems. Thermodynamical

consideration meeting the conditions of the free energy minimum should be applied to describe equilibrium structures. (ii) non-equilibrium domain structure can be formed in so called open systems. In this case the resulting structure is additionally ordered by growth kinetics. In the context of semiconductor growth the closed structure can be realized by long-term growth interruptions or by post-growth annealing whereas, the open structures are formed in the growth process and observed in as-grown samples.

In the case of SML deposition these domains are ML-height islands on the substrate surface. The driving force of the ordering of domains is surface stress relaxation. The surface stress is determined by the fact that atoms in the surface layer are in a different environment to that in the bulk, and the surface layer energetically favours a lattice parameter to be different from the bulk value - the surface layer is intrinsically compressed or stretched. Thus the surface can be characterized by the intrinsic surface stress tensor $\beta_{\mu\nu}$ [78]. The discontinuity of $\beta_{\mu\nu}$ at domain boundaries creates a long-range strain field and results in an elastic energy relaxation. The energetically favourable structure is then a 2D periodic structure of domains [79, 80].

The formation of the periodically ordered structure of ML-height islands has still to be realized for the CdSe/ZnSe SML system by finding the appropriate growth conditions. This is not an easy task, since precise growth control still remains difficult for such structures. However, it has already been shown by scanning tunneling microscopy (STM) for MBE-grown InAs/GaAs(100) islands that there exists a range of deposition parameters where islands have a similar shape and size and form a locally ordered (4x4) arrays for a coverage as low as 0.17 MLs [76].

Chapter 3

SFR spectroscopy of bulk epitaxial layers

3.1 Introduction

In this chapter we present a SFR spectroscopy study of bulk epitaxial layers of the cubic modification of $Zn_{1-x}Cd_xSe$ ($0 < x \leq 1$). The main purpose of the present work was to investigate changes of the electron g-factor with Cd content.

The electron g-factor (or gyromagnetic ratio) describes the magnitude of the Zeeman splitting between the two spin states of an electron in a magnetic field (see Eq. 1.1). In semiconductors its value, due to spin-orbit coupling, can differ substantially from the value $g_0 \approx 2$ for a free electron in vacuum and can be positive or negative. For conduction electrons and electrons bound in conduction band related states (shallow donors, excitons) the g-factor is, like the effective mass, very sensitive to the band structure of the material. The determination of g can therefore be used to test band structure theories. Furthermore, the g-factor is affected by quantum confinement and knowledge of its dependence on x for bulk $Zn_{1-x}Cd_xSe$ alloys is a necessary prerequisite for the understanding of the magnetic behaviour of electrons in $Zn_{1-x}Cd_xSe$/ZnSe quantum well structures and in CdSe/ZnSe quantum dot systems.

This is the first time that such data have been obtained for the cubic phase of this

material. Five-band $\mathbf{k}\cdot\mathbf{p}$ perturbation theory was successfully used to reproduce the experimental dependence of the g-factor on Cd content. General information concerning the electron g-factor is given in Appendix B and the $\mathbf{k}\cdot\mathbf{p}$ theory is outlined in Appendix C.

It is essential to mention that the obtained data related to the case of liquid Helium temperatures.

3.2 Experiment and samples

The SFR scattering experiments were carried out using the apparatus described in section 1.3 of Chapter 1.

The samples of cubic $Zn_{1-x}Cd_xSe$ were grown by MBE on substrates of (100) GaAs (x = 0.04, 0.15, 0.24, 0.42, 0.61; Heriot-Watt University) and of cubic CdSe on (100) InAs (Ioffe Institute). The choice of InAs instead of GaAs for the growth of cubic CdSe reduces the density of extended defects that would otherwise be caused by the large CdSe/GaAs lattice mismatch (see section 2.4 of Chapter 2). The Cd content determination was based on low-temperature measurements of excitonic photoluminescence (PL) and reflectance and is in good agreement with the growth calibrations based on reflection high-energy electron diffraction (RHEED) oscillations [81]. The thicknesses of the epilayers (around 1 μm) and confirmation that they were of the fully relaxed cubic modification were obtained by RHEED and X-ray scattering measurements. In particular, from these measurements the CdSe lattice constant for the CdSe/InAs structure was determined to be 6.077$\pm$0.001 Å being in agreement with the value for cubic CdSe reported in the literature [52, 64]. An epilayer of pure ZnSe (thickness slightly above t_{cr}) as well as an epilayer of a very low Cd content ZnCdSe (x = 0.002, thickness $\sim$ 1 μm) grown on (100) GaAs substrates by metal organic vapor phase epitaxy (North-East Wales Institute) have also been investigated. A comparison with the published X-ray scattering data [48, 64, 82] allows one to conclude that all our epilayers are of the best structural quality achievable to date; Fig. 2.7 shows the X-ray scattering spectra for three of the investigated samples. This fact is also supported by existence of a strong excitonic PL (see the following section) and phonon Raman scattering in all of the epilayers. In the latter case, narrow

LO-phonon lines are detected in the backscattering geometry of the experiment, whereas TO-phonon signals are absent. This result is consistent with the selection rules for structures having cubic symmetry [83]. Fig. 3.1 shows the dependence of the LO-phonon energy on Cd content in the epilayers investigated.

3.3 Experimental results

3.3.1 Photoluminescence

For the purpose of using the resonant enhancement effect described in section 1.4.2 of Chapter 1, the SFR scattering experiments were performed by exciting in resonance with the bands of the excitonic PL. We now consider the excitonic PL of the samples investigated.

Excitonic PL in epitaxial ZnSe grown on (100) GaAs has been widely studied [84, 85]. In a PL spectrum of a high quality epilayer, taken at liquid helium temperature, a structure consisting of well resolved bands of free exciton (FX) transitions and I_2 transitions (corresponding to excitons bound at shallow neutral donors (D^0X)) is usually observed. The most common donors are Cl and Ga (depth around 25 meV; well described by the hydrogenic model). Adding even a small amount of Cd ($x < 0.01$) to ZnSe leads at least (i) to a shift of the excitonic spectrum towards lower energies, (ii) to a broadening of the components and (iii) to a strong decrease of the FX intensity. Fig. 3.2 demonstrates this picture.

The result of further increases of Cd content is shown in Fig. 3.3, where the PL spectra of cubic $Zn_{1-x}Cd_xSe$ alloys with three different values of x are presented. The spectra demonstrate two main PL features commonly observed in epilayers of $Zn_{1-x}Cd_xSe$ grown on GaAs. The broad emission on the low energy side of each of the spectra arises from defects that have not yet been identified. The intensity of this band increases with x. The strong and relatively narrow band (width 8-10 meV) on the high energy side was attributed in Ref. [48] to PL of an impurity bound exciton. Our spectra are consistent with this interpretation, since the higher energy PL band lies about 5 meV beneath the free exciton feature in the reflectance spectra, a typical binding energy of an exciton to a shallow donor.

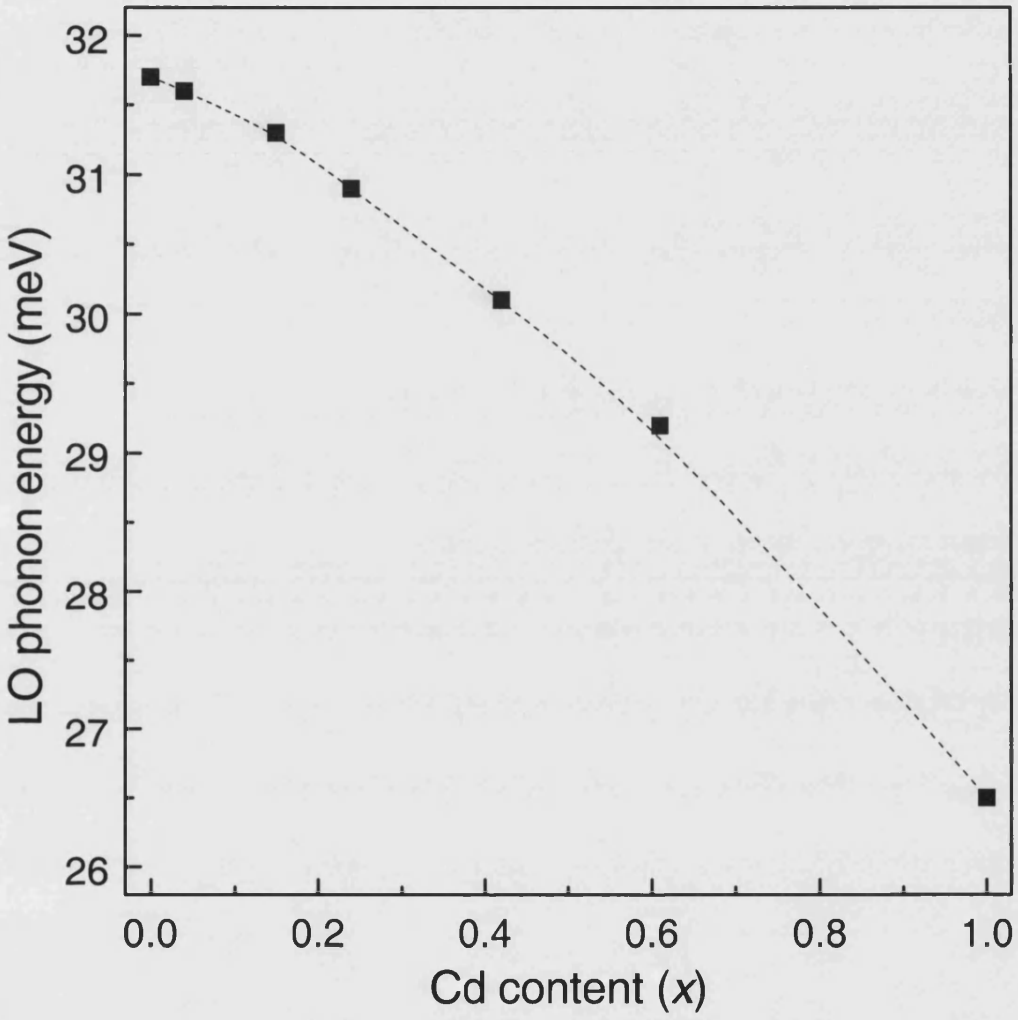

Figure 3.1: Dependence of the LO-phonon energy on Cd composition x in cubic $Zn_{1-x}Cd_xSe$ epilayers. The data corresponding to ZnSe and CdSe are also included. $T = 1.5$ K.

This assignment also agrees with other work on $Zn_{1-x}Cd_xSe$ in which, despite experimental indications of exciton localization by compositional fluctuations, the near edge PL is dominated by the emission of bound excitons [50]. Since ZnSe and CdSe are normally n-type, we assign the higher energy PL band to the recombination of excitons bound at neutral donors I_2. However a possible (weak) contribution of acceptor bound excitons I_1 and localized excitons to this band can not be completely omitted (see section 2.3 of Chapter 2). The shift of this band and of the free exciton feature in the reflectance spectra to lower energy with increasing Cd content reflects the reduction of the alloy fundamental band gap and is in a good agreement with calculations [51]. The transition with a peak at 1.745 eV in the PL spectrum of the pure CdSe sample (Fig. 3.4) is also attributed to D^0X [64]. We note that the free exciton feature in this sample is seen as a pronounced shoulder on the high energy PL slope of the D^0X and that it lies about 80 meV lower in energy than the FX (A-exciton) in CdSe of hexagonal modification.

In a magnetic field B the excitonic PL bands change their positions towards the higher energies, thus exhibiting a diamagnetic shift

$$E(B) = E(0) + cB^2, \tag{3.1}$$

where c is the diamagnetic coefficient. The inset to Fig. 3.4 demonstrates this effect for the D^0X exciton in cubic CdSe.

3.3.2 SFR scattering

We have already introduced Spin-flip Raman scattering in Chapter 1 as a process consisting of the inelastic scattering of light from a charge carrier in a semiconductor when, in the scattering process, the spin state of the charge carrier is altered. When the semiconductor is placed in a magnetic field B, the two electron-related spin states $S_z = \pm 1/2$ split in energy by an amount given by Eq. 1.1. The shift in energy between the incident and scattered light (Raman shift) is a direct measure of this splitting, so that g is readily determined. The g-factors of conduction band electrons, electrons in excitons, electrons in excitons bound to shallow impurities and electrons bound to donors are expected to be very similar to each other [3].

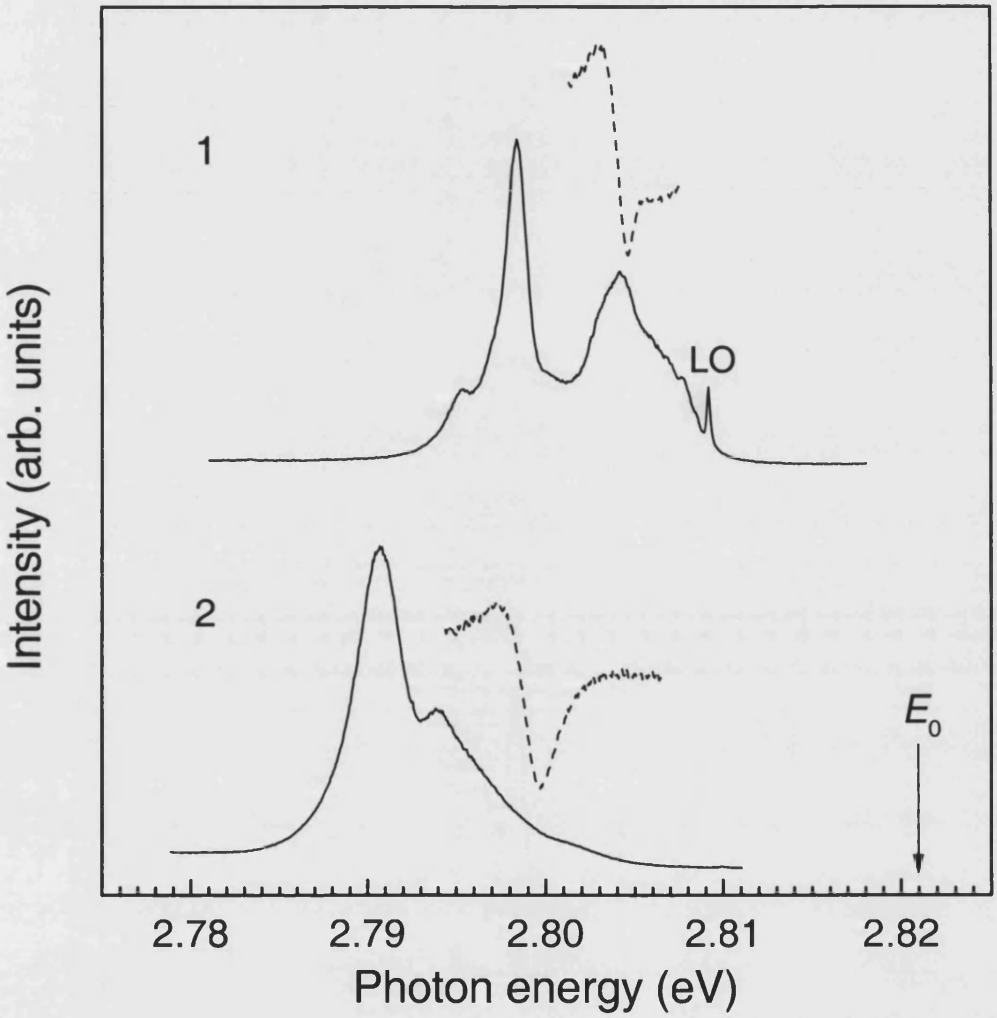

Figure 3.2: PL (solid) and reflectance (dashed) spectra of 1) ZnSe and 2) $Zn_{0.998}Cd_{0.002}Se$ epilayers grown on (100) GaAs, $T = 1.5$ K. The PL bands corresponding to the features in the reflectance spectra are due to FX transitions. The others dominating bands are due to D^0X transitions [85]. The arrow labeled E_0 indicates the ZnSe fundamental band gap energy.

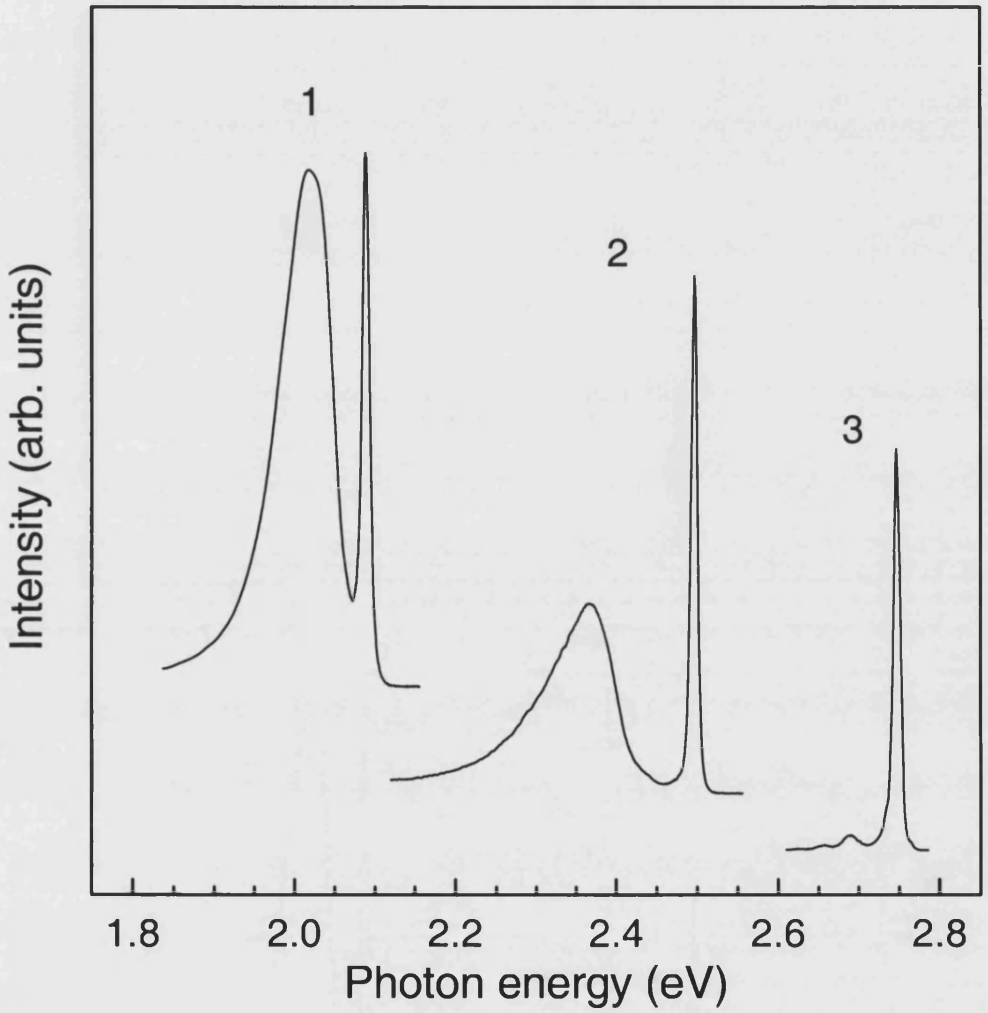

Figure 3.3: PL spectra of cubic $Zn_{1-x}Cd_xSe$ with different Cd content, x: 1 - 0.61, 2 - 0.24 and 3 - 0.04, $T = 4.5$ K. The spectra 1 and 2 were shifted along the intensity-axis for clarity.

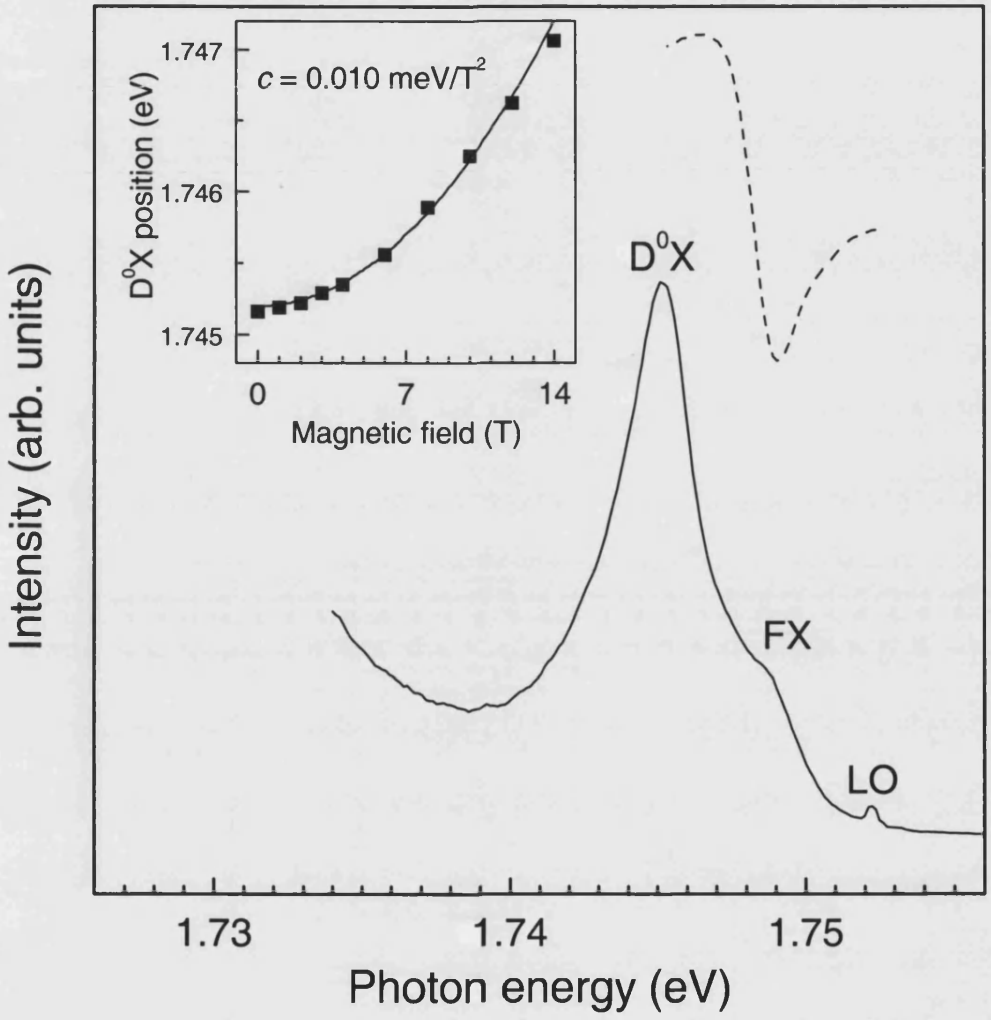

Figure 3.4: PL (solid) and reflectance (dashed) spectra of cubic CdSe, $T = 4.5$ K. The labels FX and D^0X indicate the free exciton and neutral donor bound excitonic PL bands, respectively. The inset presents the diamagnetic shift of the PL peak for the D^0X band.

The SFR scattering experiments presented in this chapter were performed by exciting in resonance with the PL transitions identified above as being D^0X. The advantage of such resonant excitation lies in the fact that the exciton forms the intermediate state in the scattering process and a strong enhancement of an electron spin-flip signal is expected when the incident photon energy $\hbar\omega_i$ approaches the energy of the excitonic state (see also Chapter 1, subsection 1.4.2). Schematically, this process is shown in Fig. 1.3. The differential cross-section in the case of D^0X for a single electron spin-flip Raman scattering is given by [3]

$$\frac{d\sigma}{d\Omega} \sim f^2 \left(\frac{e^2}{m_0 c^2}\right)^2 \frac{\omega_s}{\omega_i} \frac{(\hbar\omega_i)^2}{(E_1 - \hbar\omega_i)^2 + (\Gamma/2)^2}, \tag{3.2}$$

where f, E_1 and Γ are respectively the oscillator strength, the energy and the phenomenological damping for the D^0X complex; $\hbar\omega_s$ is the energy of the scattered photons. Such resonant enhancement has been used widely for the investigation of SFR scattering in semiconductors and particularly for g-factor measurements (see for example, Refs. [3] and [86]).

Examples of the resonance enhancement of the scattering efficiency are demonstrated in Fig. 3.5 for two epilayers (ZnSe and $Zn_{0.998}Cd_{0.002}Se$), where the inset shows a typical spectrum of the well-studied SFR process of an electron bound to a donor in ZnSe. It is seen that the SFR resonance profiles repeat in detail the excitonic PL profiles for these epilayers (shown in Fig. 3.2).

We concentrate further on the results obtained on cubic CdSe. In Fig. 3.6, we show SFR scattering spectra for this material obtained when the excitation is tuned to the energy of D^0X. In the Voigt geometry (the direction of $\mathbf{B}$ is then perpendicular to the light propagation direction $\mathbf{k}_l$), similar to the ZnSe case, strong Stokes and anti-Stokes Raman signals are detected when the linear polarizer and analyzer are mutually perpendicular. In contrast, these signals are very weak in the Faraday geometry ($\mathbf{B} \parallel \mathbf{k}_l$), independent of the polarization conditions. This behaviour corresponds to the appropriate electric dipole selection rules selection rules for an electron spin-flip[1] (see section 1.4.3 of Chapter 1). The Raman shifts of the Stokes and anti-Stokes are equal for both geometries and are proportional to the magnetic field. By use of Eq. 1.1, we obtain for cubic CdSe

[1]The observation of the (forbidden) signals in the Faraday geometry more probably is due to a weak relaxation of the selection rules caused by the imperfections of the experimental alignment described in section 1.3 of Chapter 1.

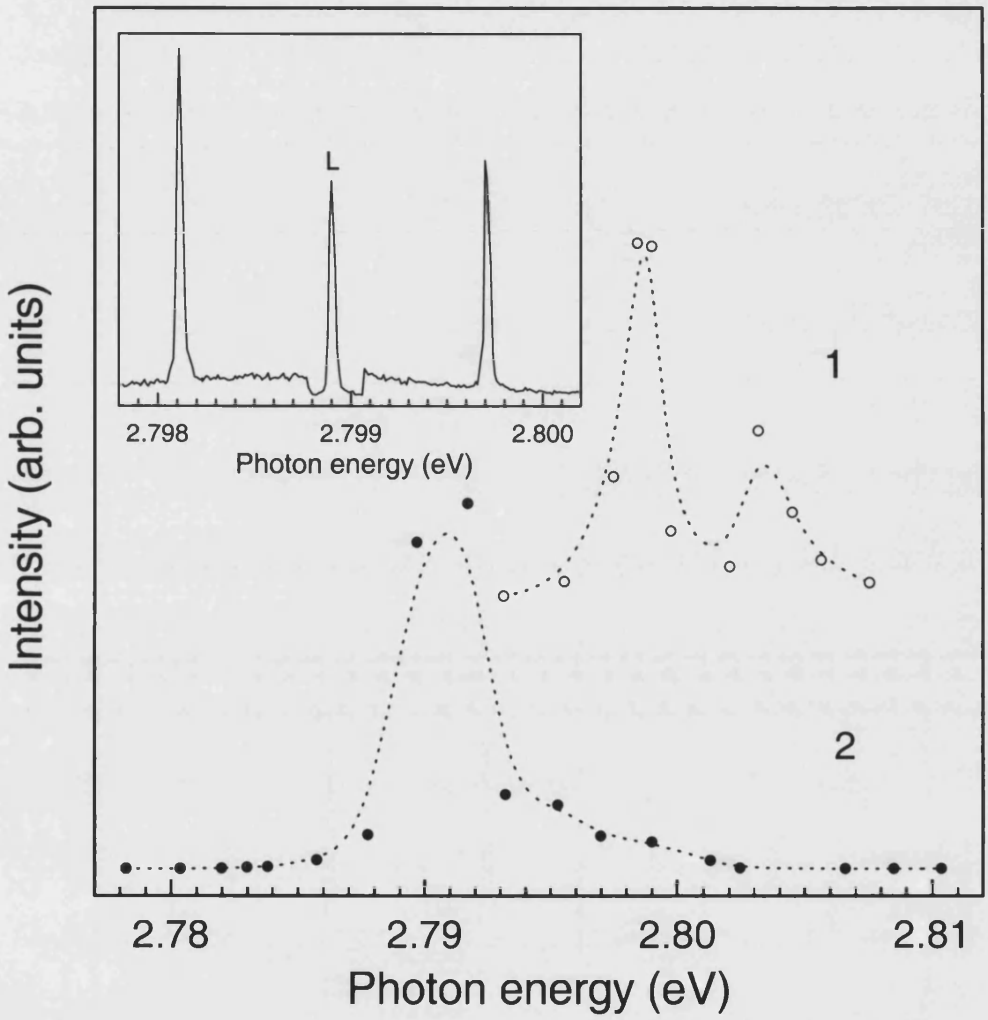

Figure 3.5: Resonance profiles of the donor electron SFR Stokes signals measured at $B = 6$ T $T = 1.5$ K in the backscattering Voigt geometry: ZnSe (1, open circles), $Zn_{0.998}Cd_{0.002}Se$ (2, solid circles). Inset shows a typical SFR spectrum taken under excitation in resonance with D^0X in ZnSe; $B = 14$ T, $T = 4.5$ K, $z(\sigma, \pi)\bar{z}$. Intensity of the exciting laser beam (corresponding spectral line is marked by L) was attenuated during the scan of the spectrum by a neutral density filter by a factor of 10.

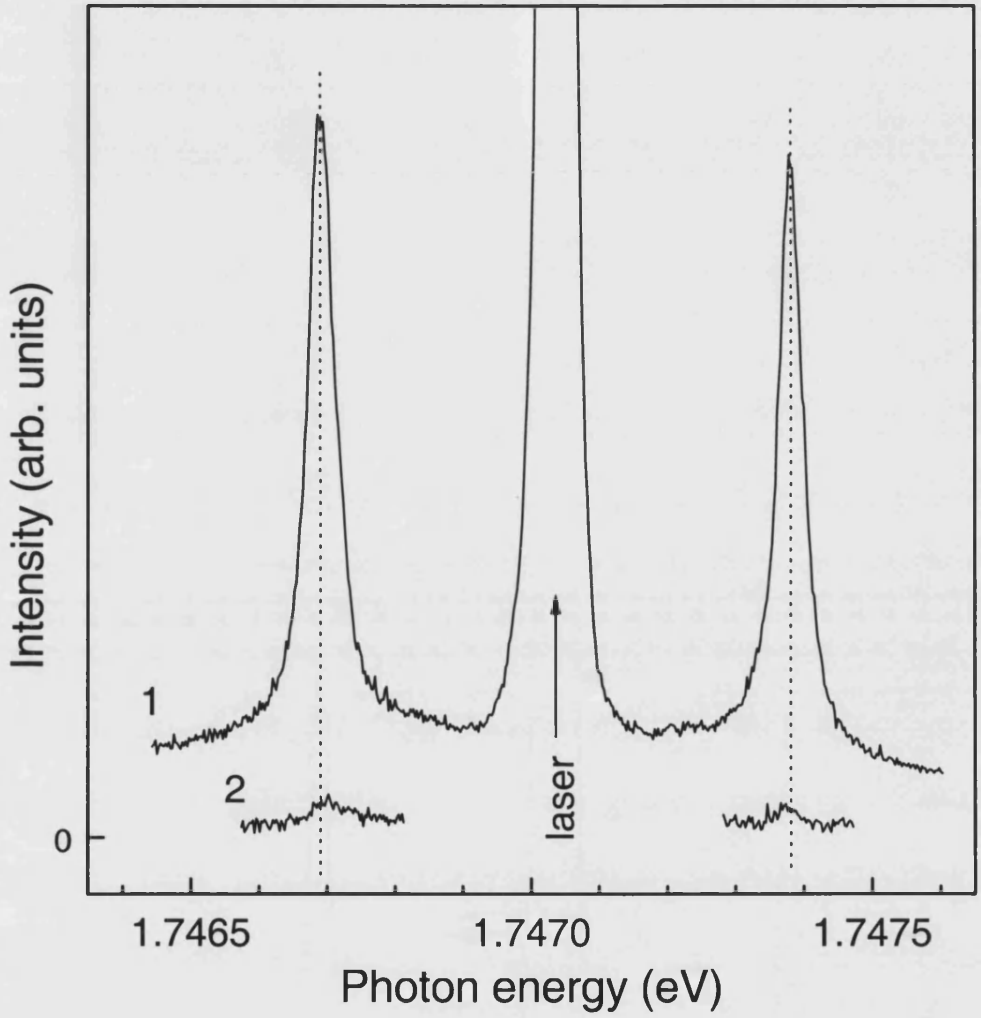

Figure 3.6: SFR scattering spectra of the donor electrons in cubic CdSe taken in the backscattering (a) Voigt and (b) Faraday geometries (see text). $T = 4.5$ K, $B = 14$ T. For clarity the laser line in case (b) is not shown. The dashed lines are guides for the eye.

$|g| = 0.42 \pm 0.01$. We observe also that the g-factor is isotropic, as expected for the SFR scattering of states related to the conduction band (i.e., free or shallow donor-bound electrons) in the cubic modification of the sample under study. Any anisotropy would suggest, for example, the existence of the hexagonal CdSe phase, or of a large strain in the cubic CdSe layer, or that the signals observed originate from scattering between valence band-related states.

The existence of a diamagnetic shift with the quadratic coefficient $c = 0.010 \pm 0.001$ meV/T^2 for the D^{0}X PL band (see inset, Fig. 3.4) leads to the situation that the excitation energy (kept constant in our experiments) *passes* through a large part of the PL band (width ~ 3.5 meV) when B changes from 14 T to 3.5 T (at lower values of B, the signals are not spectrally resolved). This affects both the absolute and relative intensity of the Stokes and anti-Stokes signals because of changing resonance conditions (obviously different for these two signals; the anti-Stokes signal can even be more intensive than the Stokes one) but does not affect the observed Raman shifts or the value of the g-factor that we obtain.

Qualitatively similar SFR scattering spectra were measured for the ZnCdSe samples with different Cd contents. The strong Stokes and anti-Stokes signals demonstrate the same selection rules as for cubic CdSe and, again, there is a linear proportionality of the Raman shifts to the magnetic field; this result for all epilayers studied, as shown in Fig. 3.7. As before, the SFR scattering signals were obtained in resonance with D^{0}X and are attributed to the donor-bound electron spin-flip; when exciting at different points of the D^{0}X PL we do not observe any variation in the g-factor within experimental error (see Fig. 3.8).

These observations contrast to other studies of ours on epitaxial CdSe submonolayers in ZnSe barriers [17] (see Chapter 4), where we observe SFR scattering transitions between the spin-split levels of localized excitons, rather than between the levels of a donor-bound electron; in the former case, Eq. 1.1 no longer describes the dependence on magnetic field of the SFR shifts, due to a finite zero-field splitting arising from the electron-hole exchange energy, whilst the parameters of the exciton spin Hamiltonian also show a significant dependence on excitation energy due to the effects of varying degrees of localization in that highly inhomogeneous system. In view of the relative simplicity of the present observations, we therefore rule out SFR scattering between excitonic levels as an explanation of the present data.

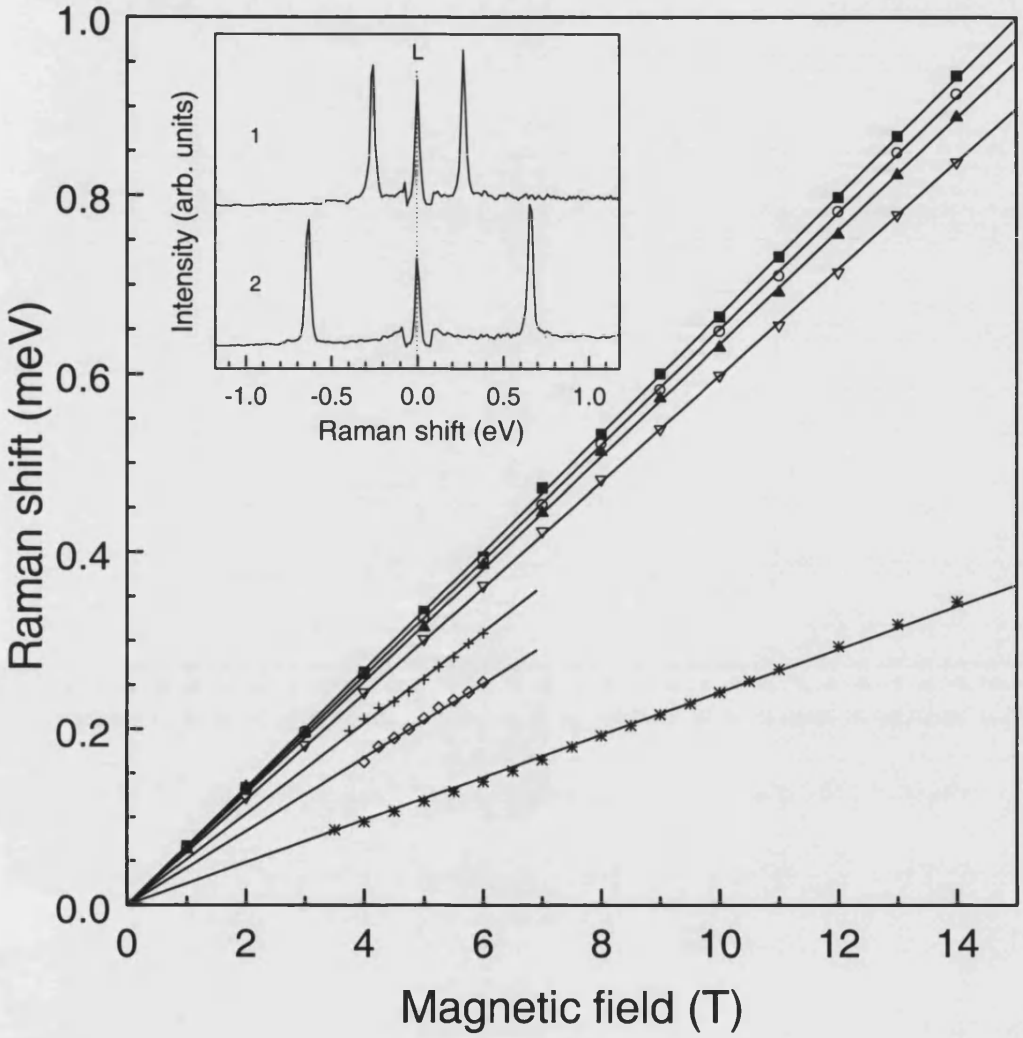

Figure 3.7: Magnetic field dependence of the Raman shift for the donor electrons spin-flip Stokes signals measured in ZnCdSe epilayers with different Cd content, $x = 0$ (ZnSe, solid squares), 0.04 (open circles), 0.15 (solid triangles), 0.24 (open triangles), 0.42 (crosses), 0.61 (diamonds) and 1 (CdSe, stars). The solid lines represent least-square fits to the data; the fits pass the origin within the experimental error. Inset presents two donor electron SFR spectra for ZnCdSe epilayer with $x = 0.04$ taken at (1) $B = 4$ T and (2) 10 T. $T = 4.5$ K; $z(\sigma, \pi)\bar{z}$.

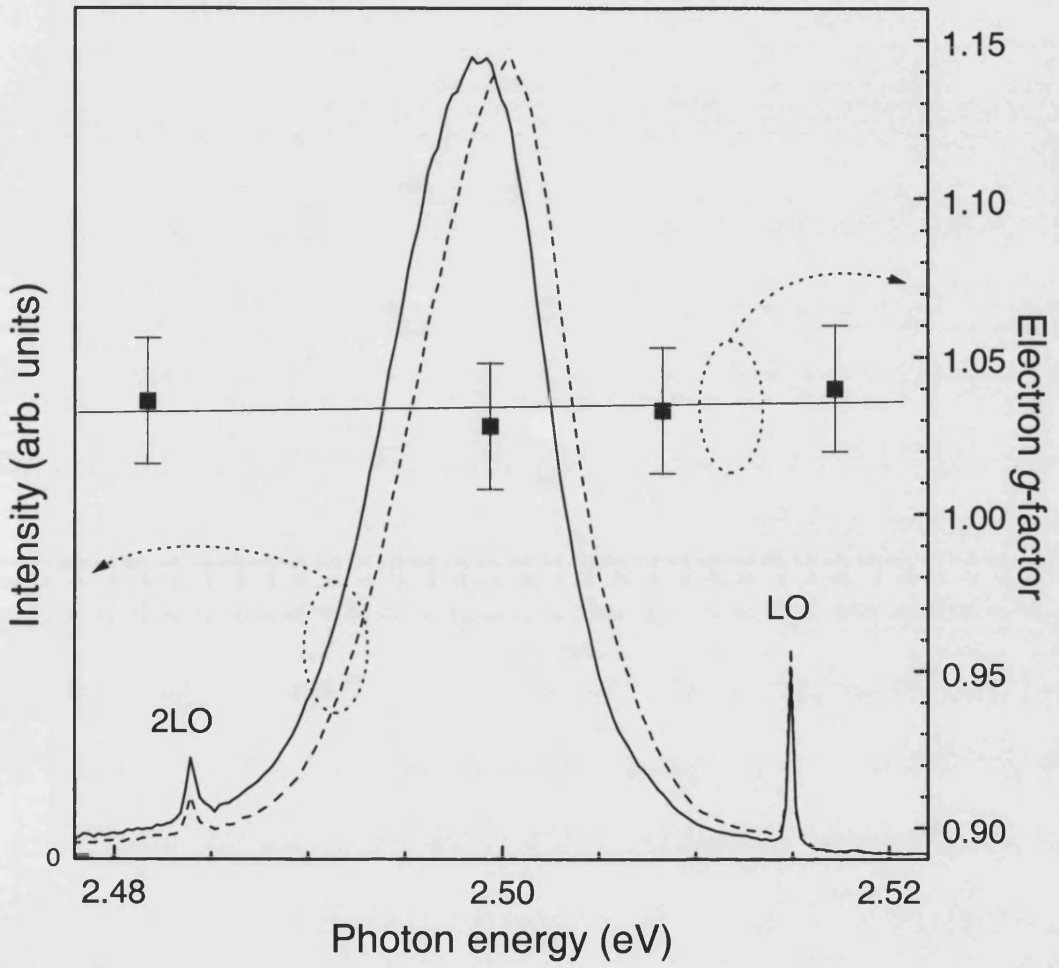

Figure 3.8: D^0X PL spectra of ZnCdSe epilayer with $x = 0.24$ taken at $B = 0$ T (solid line) and 14 T (dashed line). The solid squares represent electron g-factors measured under excitation of SFR scattering at different spectral points of the D^0X PL.

3.4 Discussion

Fig. 3.9 present the g-factors measured for the samples with different x (solid circles). It includes also the value of $g = 1.15 \pm 0.01$ for epitaxial ZnSe on (100) GaAs, which we measured also by SFR scattering as part of this work. This value is close to the value of $g = 1.120 \pm 0.001$ for electrons in conduction band related states determined by an optically-detected magnetic resonance (ODMR) experiment [87]. Direct measurements using circularly-polarized microwave radiation in this ODMR experiment established also that the ZnSe g-factor is positive [88]. This value of g also agrees well with that calculated via five-band $\mathbf{k} \cdot \mathbf{p}$ perturbation theory [89] for ZnSe. Therefore, the monotonic dependence of g from its value for ZnSe to that for cubic CdSe shows that the g-factor remains positive for the entire region of Cd content in cubic $Zn_{1-x}Cd_xSe$. For convenience in using these data, we note that a quadratic least squares fit to the data over the whole composition range yields the relationship $g(x) = 1.16 - 0.56x - 0.18x^2$.

The ZnCdSe epilayers were sufficiently thick ($t \gg t_{cr}$) that they could be assumed to be relaxed to a zero-strain state at the growth temperature, though they may still be strained at the liquid helium temperature because of the different contractions of ZnSe, CdSe and GaAs (see section 2.4 of Chapter 2). In general the lattice mismatch (compressive) and thermally induced (tensile) strain lead to a splitting of the degenerate Γ_6 heavy- and light-hole free exciton states and to their shift (in energy) compared to the zero-strain case [84]. This is demonstrated by the FX band of the ZnSe PL (see Fig. 3.2). This band has an asymmetric shape, where the main peak is attributed to the heavy hole exciton and the shoulder on the high energy side is due to the light-hole exciton [85]. A slight shift ($\sim 1 - 2$ meV) towards the higher energies compared to the bulk ZnSe case [90] is also observed. Nevertheless, the g-factor for this sample is identical, within experimental error, with that we measured for the much thicker and therefore being differently strained $Zn_{0.998}Cd_{0.002}Se$ epilayer. It has also been established in our studies of many samples of doped epitaxial ZnSe that typical thermal and lattice mismatch strains do not induced any detectable shift in the conduction band g-factor. So we shall not discuss here the details of the influence of the strain on the g-factor for the different samples.

To model the experimental data we have carried out calculations using an ex-

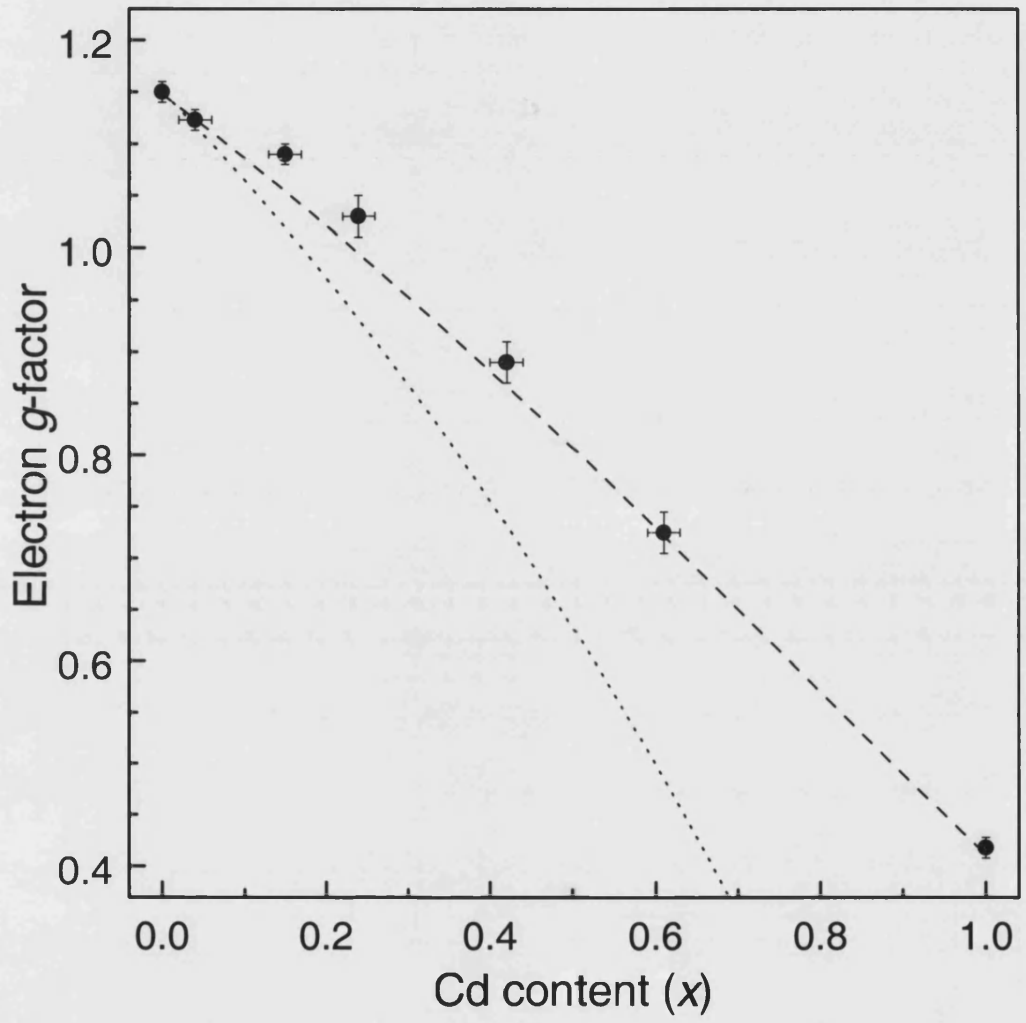

Figure 3.9: Dependence of the electron g-factor for cubic $Zn_{1-x}Cd_xSe$ on Cd content. The solid circles are experimental points. The dotted and dashed curves present the result of the calculations (see text).

pression derived from the five-band $\mathbf{k}\cdot\mathbf{p}$ second order perturbation theory.

Based on $\mathbf{k}\cdot\mathbf{p}$ perturbation theory the g-factor for an electron at the Γ-point in a non-degenerate band of a cubic semiconductor is given as [91, 92]:

$$\frac{g}{g_0} = 1 + \frac{1}{im_0}\sum_n \frac{< S|p_x|n >< n|p_y|S > - < S|p_y|n >< n|p_x|S >}{E_0 - E_n}, \qquad (3.3)$$

where g_0 is the free electron g-factor, S the conduction-band wave function; the wave function n corresponds to a state at energy E_n; $p_{x(y)}$ is the $x(y)$ component of the momentum operator. Taking into account five bands, namely Γ_6^c, Γ_7^c, Γ_8^c, Γ_8^v, Γ_7^v (see schema of Fig. 3.10) an expression presenting an approximation to Eq. 3.3 can be derived [89, 93, 94]

$$\begin{aligned}\frac{g}{g_0} &\approx \left[1 - \frac{P^2}{3}\left(\frac{1}{E_0} - \frac{1}{E_0+\Delta_0}\right)\right] \\ &- \left[\frac{P'^2}{3}\left(\frac{-1}{E_0'+\Delta_0'-E_0} + \frac{1}{E_0'-E_0}\right) + C'\right] \\ &+ \left[\frac{2}{9}\frac{\Delta^- PP'}{E_0'-E_0}\left(\frac{1}{E_0} + \frac{2}{E_0+\Delta_0}\right)\right],\end{aligned} \qquad (3.4)$$

where, in Cardona's notation E_0, E_0', Δ_0, Δ_0' are the energy intervals shown schematically in Fig. 3.10; the quantities (expressed in eV)

$$P^2 = (2/m_0)|< S|p_x|n_v >|^2$$

and

$$P'^2 = (2/m_0)|< S|p_x|n_c >|^2$$

are the squared momentum matrix elements describing the coupling to the p-bonding valence band ($\Gamma_8^v + \Gamma_7^v$) and to the p-antibonding conduction band ($\Gamma_8^c + \Gamma_7^c$); m_0 is the free electron mass. In Eq. 3.4 the first term is that arising from the three-band model whilst, with the addition of the second term, the expression is that of the five-band model. In the second term the quantity C' contains contributions to g-factor from higher conduction bands; it is accepted that $C' = -0.02$ in all semiconductor compounds [89, 93]. The third term adds the off-diagonal spin-orbit coupling term Δ^- via third-order (rather than second-order) perturbation theory [89, 94]. We refer to the models that include each of these three terms in succession as the three-band (3B), five-band (5B) and third-order (TO) models, respectively.

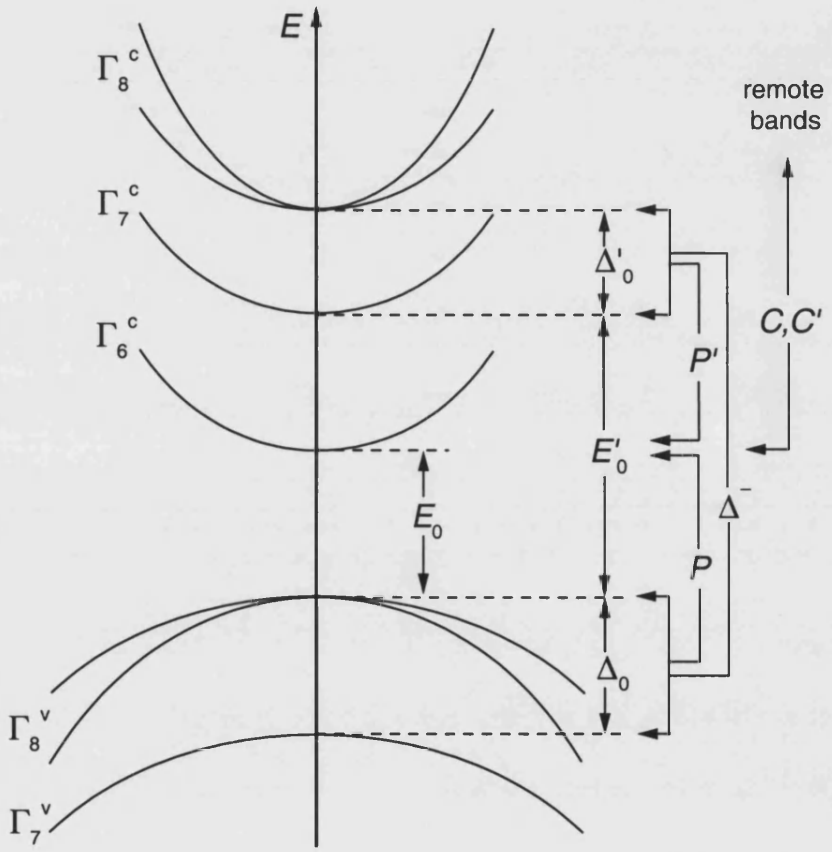

Figure 3.10: Schematics of the band structure near the Γ-point in a zinc-blende semiconductor.

The 3B term alone does not give a good description of the electron g-factor for ZnSe . For example, taking the values of E_0, P^2 and Δ_0 that are shown in Table 3.1, one obtains a calculated value of $g = +1.28$ for ZnSe, which differs from the measured value by considerably more than the experimental uncertainties. However, with the same parameters, the 5B and especially TO models give much better descriptions of the experimental data not only for ZnSe but for the whole range of II-VI compounds and their alloys [89, 95]. We therefore expect Eg. 3.4 to be applicable also for $Zn_{1-x}Cd_xSe$ and CdSe.

For the calculations a linear interpolation between the corresponding parameters of ZnSe and cubic CdSe has been used, apart from the band gap E_0, where a bowing parameter of $b = 0.301$ eV in the conventional expression $E_0(x) = (1-x)E_0(0) + xE_0(1) - bx(1-x)$ was included [51]. The band parameters for ZnSe and CdSe that were used are presented in Table I. Since the values of the squared interband matrix elements P^2 and P'^2 for cubic CdSe are not available from the literature, we used first the corresponding values for ZnSe, keeping them constant over the entire region of Cd composition and only varying the band gap. The dotted curve in Fig. 3.9 shows the result of this calculation. A large discrepancy with the experimental data exists for $x > 0.15$. The most likely reason for this discrepancy is that, as shown by Hermann and Weisbuch [93], P^2 and P'^2 do not remain constant over the entire composition range of a ternary semiconductor. For the present case of $Zn_{1-x}Cd_xSe$, we therefore need to obtain these parameters for cubic CdSe itself and then to make a linear interpolation over the intermediate composition range.

To estimate P^2 and P'^2 for cubic CdSe we applied the approach of Hermann and Weisbuch [93], in which Eq. 3.4 is solved for P^2 and P'^2 simultaneously with the equation for the conduction electron effective mass, m (isotropic: $m = m_x = m_y = m_z$), also derived within a five-band $\mathbf{k}\cdot\mathbf{p}$ framework:

$$\begin{aligned} \frac{m_0}{m} - 1 &= \sum_n \frac{|<S|p_x|n>|^2}{E_0 - E_n} \\ &\approx \left[\frac{P^2}{3}\left(\frac{2}{E_0} + \frac{1}{E_0 + \Delta_0}\right)\right] \\ &- \left[\frac{P'^2}{3}\left(\frac{2}{E_0' + \Delta_0' - E_0} + \frac{1}{E_0' - E_0}\right) + C\right], \end{aligned} \tag{3.5}$$

where C is the term accounting for remote bands. It is accepted that $C = 2$

Table 3.1: Band parameters (in eV) for ZnSe and (cubic) CdSe used for the calculations.

	E_0	Δ_0	E'_0	Δ'_0	Δ^-	P^2	P'^2
ZnSe	2.821[a]	0.403[b]	7.33[b]	0.09[b]	−0.046[c]	24.27[c]	9.83[c]
CdSe	1.764[d]	0.47[c]	6.8[e]	0.24[c]	−0.047[c]	18.3[f]	4.9[f]

a - from Ref. [51], *b* - from Ref. [90], *c* - from Ref. [89], *d* - obtained by adding the hexagonal CdSe free exciton binding energy of 15 meV [51] to the experimentally measured free exciton PL transition energy for cubic CdSe (present work), *e* - from Ref. [98], *f* - estimated from the experimental values for the hexagonal CdSe electron effective mass [51] and the electron *g*-factor (present work) for cubic CdSe via the expression given in Eqs. 3.4 and 3.5.

for all semiconductor compounds [93]. The coupling through Δ^- affects m only negligibly [96] and the appropriate term is omitted in Eq. 3.5. In our analysis we used the well known value $m = 0.13m_0$ for bulk hexagonal CdSe [51]. There are no published data for cubic bulk CdSe and we therefore use this value rather than the recent value $m = 0.112m_0$ [97] obtained by cyclotron resonance measurements for electrons in modulation-doped cubic CdSe/ZnSe which has been obtained for a 10.5 nm single quantum well, rather than for bulk material. The resulting parameters are given in Table I. The use of P^2 and P'^2 estimated in this way allows us to calculate the dependence of the *g*-factor on the Cd content, which is now in very good agreement with experiment (Fig. 3.9, dashed curve). The value of P'^2 that we obtain for cubic CdSe (4.9 eV when expressed in energy units) is approximately a factor of two lower than that of ZnSe; a difference of this magnitude is quite plausible (for instance, estimates of P'^2 for CdTe, CdS and ZnS are all in the range 5-10 eV [89]). A good estimate of the value of P^2 (independent of the above approach) can be obtained by noting that, in the nearly-free electron model, its value is given by $h^2/a_0^2 m_0 e$ where a_0 is the lattice constant [83]. This estimate leads to a value of 16.6 eV, using a lattice parameter of 6.077 Å [52], in reasonable agreement with the value of 18.3 eV that the above procedure yields.

We note finally that our *g*-factor of 0.42 ± 0.01 for cubic CdSe compares well with the values of $g_\parallel = 0.6 \pm 0.1$ and $g_\perp = 0.51 \pm 0.05$ obtained respectively for the magnetic field parallel to and perpendicular to the c-axis in the hexagonal modification[90]. In Ref. [89], it was an average of these values $(g_\parallel + 2g_\perp)/3 = 0.54$ which was used when comparing theory with experiment. This earlier paper also used the ZnSe values of P^2 and P'^2 in the analysis of CdSe, thereby obtaining

a theoretical value for cubic CdSe of $g = 0.23$ which is much smaller than the value we observe by SFR scattering. In the present work we have been able to remove this discrepancy by using the directly measured value of the g-factor for the cubic phase of CdSe and by using consistent values of P^2 and P'^2 obtained as discussed above.

Chapter 4

SFR spectroscopy of low-dimensional systems

4.1 Introduction

SFR spectroscopy has recently been applied intensively to study properties of excitons localized in semiconductor low-dimensional systems [12, 13, 14, 15, 16, 17, 18]. The studied systems include QWs made from different compounds (such as GaAs/Al(Ga)As, CdTe/CdMgTe) and QDs formed by Stranski-Krastanov growth (InAs/GaAs, InP/InGaP) or by diffusion-controlled phase decomposition of solid solutions while annealing in a glass matrix (CdS/glass). In such studies, for example, SFR spectroscopy allows one to measure the exciton g factors and their variation with the confinement conditions. In addition (in a system with a quantum well), by varying the angle between the quantum well planes and the magnetic field, the electron and hole g factors contributing to an exciton can be determined separately, unlike, e. g., in electron spin resonance or photoluminescence measurements, where usually only one or a combination of these parameters is obtained. Another example is that the SFR technique can provide information about such an interesting phenomenon as exchange interaction existing between an electron and a hole within an exciton (general information on the exchange interaction is given in Appendix D). Also SFR spectroscopy is a very convenient tool to study properties of excitations localized in different states within a broad ensemble of localized states of a single highly inhomogeneous system (the exciting

laser photon energy can be adjusted within a spectral interval of less than 0.1 meV).

In this chapter we report on results of a SFR study of ZnCdSe/Zn(S)Se QWs and CdSe/ZnSe submonolayer structures. Shortly after the beginning of our study, Puls and Henneberger published the results of their magneto-optical experiments, where the resonant excitation was applied to the ZnCdSe/ZnSe QW system in the Voigt geometry [99]. This was the first publication in this area. Our experimental observations on this system are more detailed but, in some points, are similar to that of Ref. [99]. The SFR results obtained on ZnCdSe QWs provide a very helpful material to study the main subject of our interest - the CdSe/ZnSe submonolayer system. This is the first time that such a system was studied by SFR spectroscopy.

4.2 Experiment and samples

The SFR scattering experiments were carried out using the apparatus described in section 1.3 of Chapter 1. A detail to mention here is that, when performing the experiments using the continuous flow cryostat (where the sample was kept at $T = 4.5$ K), the incident laser power was kept below 0.1 W/cm^2 to avoid heating of the sample.

SFR scattering experiments have been performed on two sets of samples. The first set includes grown by MBE on (100) GaAs substrates single QW structures. The QW and the thick (< 50 nm) barrier regions ware formed by ZnCdSe and/or ZnSe/$ZnS_{0.06}Se_{0.94}$, respectively. The amount of 6% of sulfur added to the barrier of ZnSe allows one to achieve a better lattice match to GaAs resulting in improvement of the structural quality of the QW region; it also leads to the slightly deeper QW potential. The Cd composition of the different QWs ranges from 12% to 25% and their thicknesses from 35 Å to 55 Å. All the samples of this set exhibited, in SFR scattering experiments, qualitatively the same behavior. We will concentrate therefore on a sample with 35 Å $Zn_{0.08}Cd_{0.02}Se/ZnS_{0.06}Se_{0.94}$ QW (sample S0601). The second set consists of CdSe/ZnSe submonolayer structures. Again as in the case of the QW structures we will concentrate our attention on one sample (sample B1485). This sample is a structure with a period of 54 Å

containing eleven sheets of nominally 0.5 MLs CdSe in ZnSe matrix. The structure has a laser diode design - the region of the CdSe submonolayer sheets was separated from the (100) GaAs substrate and the surface by thick ZnSe, ZnSSe and ZnMgSSe layers. This provides lattice matching and good electronic confinement of the carriers in the submonolayer region. The structures of both sets of samples ware grown in the MBE facilities laboratories of the University of Bremen (QWs) and the Ioffe Institute (QWs and submonolayers) - the world's leading laboratories for the production of the state-of-the-art II-VI semiconductor structures.

4.3 Experimental results

4.3.1 Photoluminescence: spectral composition

Low temperature steady-state excitonic PL in pseudomorphic ZnCdSe/Zn(S)Se QWs has been studied intensively [51, 100]. It is determined by excitons localized in the QW at potential fluctuations formed by compositional disorder and in addition to interface roughness. Consider some details of the PL in ZnCdSe/Zn(S)Se QWs noting that in comparison with the case of three-dimensional localization, the quantum confinement of excitonic states in low-dimensional structures strongly enhances the effect of localizing potential due to compositional fluctuations [101, 102]. This determines the large PL efficiency of localized excitons (LX) in the ZnCdSe-based low-dimensional structures compared to the case of bulk ZnCdSe alloys.

A PL spectrum of an undoped ZnCdSe/Zn(S)Se QW structure has the typical line shape displayed in Fig. 4.1; the spectrum was obtained by measuring PL of the S0601 structure used for the SFR study. The 6% sulfur in ZnSSe barrier region does not change qualitatively the PL spectrum compared to that of structures with ZnSe barriers (mainly it leads to a shift of the spectrum towards higher energy due to the creation in this case of a deeper confining potential for electrons and holes). In general, the spectrum is asymmetric with an intensity shoulder on the low energy side. The spectrum can be satisfactorily fitted by two Gaussian bands of different width. The high energy band is assigned to emission of heavy

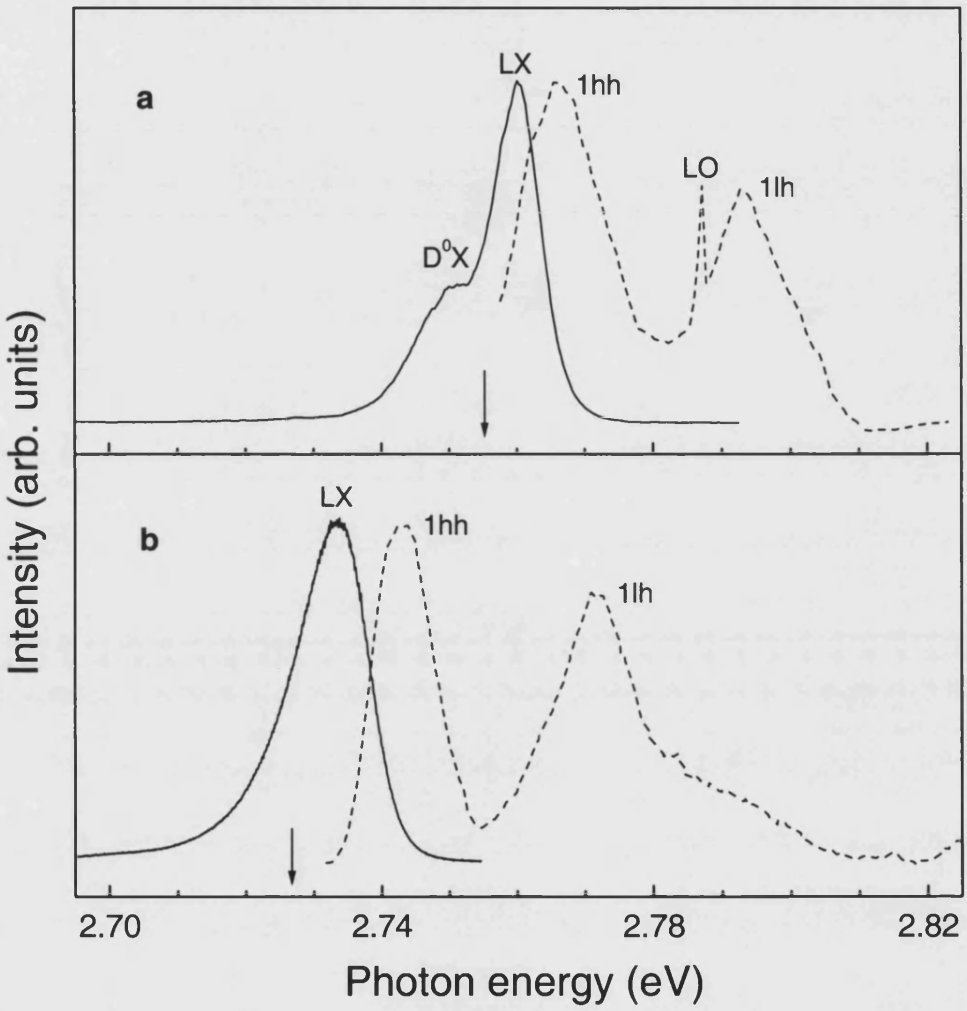

Figure 4.1: PL and PLE (solid line and dashed line, respectively) spectra of a) - 35 Å $Zn_{0.80}Cd_{0.02}Se/ZnS_{0.06}Se_{0.94}$ single QW structure (S0601) and b) - 0.5 MLs CdSe/ZnSe structure (B1485). The arrows indicate the PLE detection energy. $T = 1.5$ K. The labels LX, D^0X and 1hh, 1lh mark, respectively the localized exciton, exciton bound at neutral donor PL and the first heavy hole and light hole PLE bands; LO labels a ZnSe LO-phonon Raman signal.

hole LXs, while the low energy band is attributed to excitons bound at neutral donors (D^0X). For samples of differing QW thickness, Cd content, growth conditions or doping, the relative intensity of the two bands as well as their widths may vary strongly. Apart from D^0X, another band can also be present on the low-energy side of the heavy hole LX. The nature of this band, as was demonstrated in many optical and magneto-optical experiments, is determined by localized bi-excitons (the bound state of two excitons with oppositely aligned spins) (LXX). With increasing the excitation power, the D^0X emission saturates and the LXX band, often being coincide with D^0X, begins to develop. The LXX band increases superlinearly with the excitation power. This fact provides a way to distinguish between LXX and D^0X transitions. Our study of excitonic PL of the sample S0601 revealed that at least at the excitation power used for the SFR experiment presented further in this Chapter, the shoulder on the low energy side belongs to D^0X (Fig. 4.1 (a)).

Consider now the excitonic PL in the case of submonolayer CdSe/ZnSe. It is also determined by the localized heavy-hole excitons. The origin and detailed parameters of the localizing potential in such structures still remain unclear (see Chapter 2). However recent investigations allow one to make some conclusions. Ivanov and Toropov have investigated a set of structures with the nominal CdSe submonolayer thickness ranging from 0.15 MLs to 1 ML (growth calibration accuracy was $\sim$ 10%) by means of steady state and time-resolved PL spectroscopies [103]. It was demonstrated that the position of the excitonic PL band decreases gradually in energy with the increase in the nominal thickness (reflecting the confinement effect) and displays a clear relationship between CdSe layer fraction and the PL band shape. A relatively narrow (5-10 meV) single peak was observed at a small mean thickness of the CdSe submonolayer (less than 0.5 MLs). With increasing the thickness (more than 0.5 MLs) a low energy shoulder begins to develop, resulting in an asymmetric (or even doublet) PL band. Fig. 4.1 (b) presents a spectrum of low temperature PL of localized excitons taken on the sample B1485, which corresponds thus to the border-line content of 0.5 MLs. The asymmetric PL band can also, as in the case of ZnCdSe/ZnSe QWs, be decomposed into two strongly overlapped Gaussian components with the high-energy component being always narrower than the low-energy one. The time-resolved PL measurements of Ref. [103] revealed a nonmonotonic behaviour of excitonic lifetimes across the overall PL contour. The lifetime corresponding to the high-energy PL component is about one order smaller than that of the low-energy

component (respectively $\sim$ 25 ps and $\sim$ 250 ps). The proposed in Ref. [103] explanation of these results is given in the following paragraph.

The high-energy PL component originates from excitons in a spatially homogeneous quantum system e. g., perfect QW. This is also consistent with the model suggesting a high density of small 2D ZnCdSe islands with a typical size less than the exciton Bohr radius. In this case, the potential fluctuations are very well averaged, leading to a narrow excitonic PL band. The wider low-energy component results from excitons localized at 2D ZnCdSe islands of a lateral size comparable with the exciton Bohr radius or larger. Although some contribution of the D^0X PL cannot be completely omitted the low-energy PL component is not attributed to this transition because both the band width and the gap between the two PL components are sensitive to the mean submonolayer thickness and growth conditions. The lateral size and width as well as Cd-content distributions related to these islands determine the larger width of the high-energy PL component. The noticeably faster PL decay corresponding to the high-energy PL component can result either from intrinsic properties of the homogeneous quantum system, reflecting a larger oscillator strength of the weaker localized (nearly free) excitons, or has an extrinsic origin like a fast trapping of excitons by the islands. This model is in agreement with the HRTEM study of the intrinsic morphology in submonolayer CdSe/ZnSe system described in Chapter 2.

In Fig. 4.1 (a) and (b) we also show PLE spectra of the samples S0601 and B1485. The two well-resolved resonances split in energy by confinement and stress are attributed to the fundamentally heavy- (1hh) and light-hole (1lh) excitons in both cases; the 1hh-1lh separations in energy are 27 meV and 30 meV, respectively. The spike marked by LO corresponds to ZnSe LO-phonon resonant Raman scattering. Some asymmetry of the 1lh band is caused by contribution of the higher lying confined excitonic states and the excitonic states in the barrier region. The Stokes shift of the LX band in the PL spectrum (under above barrier excitation) from the 1hh band in the PLE spectrum represents clear evidence for localization. The value of the Stokes shift of about 8 meV (S0601) and 10 meV (B1485) as well as the width of the LX band of about 6 meV (S0601; measured after decomposing the overall PL contour into two Gaussians) and 15 meV (B1485) indicate that in these structures the energy relaxation from the free excitons (which reached the exciton mobility edge) to the LXs is assisted by the acoustic phonon emissions rather than by one LO phonon emission.

We note finally that in multisheet submonolayer structures a vertical coupling of excitons in different sheets occurs if the separating ZnSe layers are of a thickness smaller or comparable with the exciton Bohr radius. It leads to the additional broadening and low-energy shift of the excitonic PL band [104]. A comparison of the excitonic PL spectrum of the sample B1485 (see the sample description given in section 4.2) with the PL spectrum taken on a sample consisting a single CdSe submonolayer of the same thickness and grown under the same conditions (Ioffe Institute) does not reveal any remarkable change in the PL band shape and its spectral position. We therefore can consider excitons in different CdSe submonolayer sheets of this structure as uncoupled in the vertical direction.

4.3.2 SFR scattering

The SFR experiments presented here were performed by exciting in resonance with the PL bands of LXs discussed in the previous section. One expects that, under such an excitation signals related to excitons can be detected. This expectation is based on the examples of recent works of Refs. [12, 14], where SFR signals from excitons localized by QW width fluctuations in GaAs/AlGaAs and CdTe/CdMgTe QW systems were detected and of work of Ref. [105], where the observed signals were attributed to excitons localized at InAs submonolayer insertions in GaAs matrix. Also due to presence of the strong D^0X component in the PL of the sample S0601 (QW) one expects to observe signals related to a SFR scattering process of an electron bound at a donor. This expectation is supported by observations of such a process in many systems, particular in ZnCdSe epilayers (see Chapter 3).

The zero – field case. Consider first the case when the magnetic field is not applied. Fig. 4.2 shows two PL spectra taken on the B1485 sample (submonolayers) under excitation spectrally in resonance with the localized exciton PL band; the top spectrum was obtained at temperature of about 50 K, whereas the bottom one taken at 1.5 K. One can see that the spectra differ remarkably - the shape of the PL wings from either sides of the exciting laser line change (the temperature shift of the PL band in this temperature range is only about 2 meV, being much less compared with the PL band width). A well resolved peak-like feature is seen on the low energy side from the laser line (spectrum 2); it appears gradually when the temperature decreases. This feature observable in all spectral points when

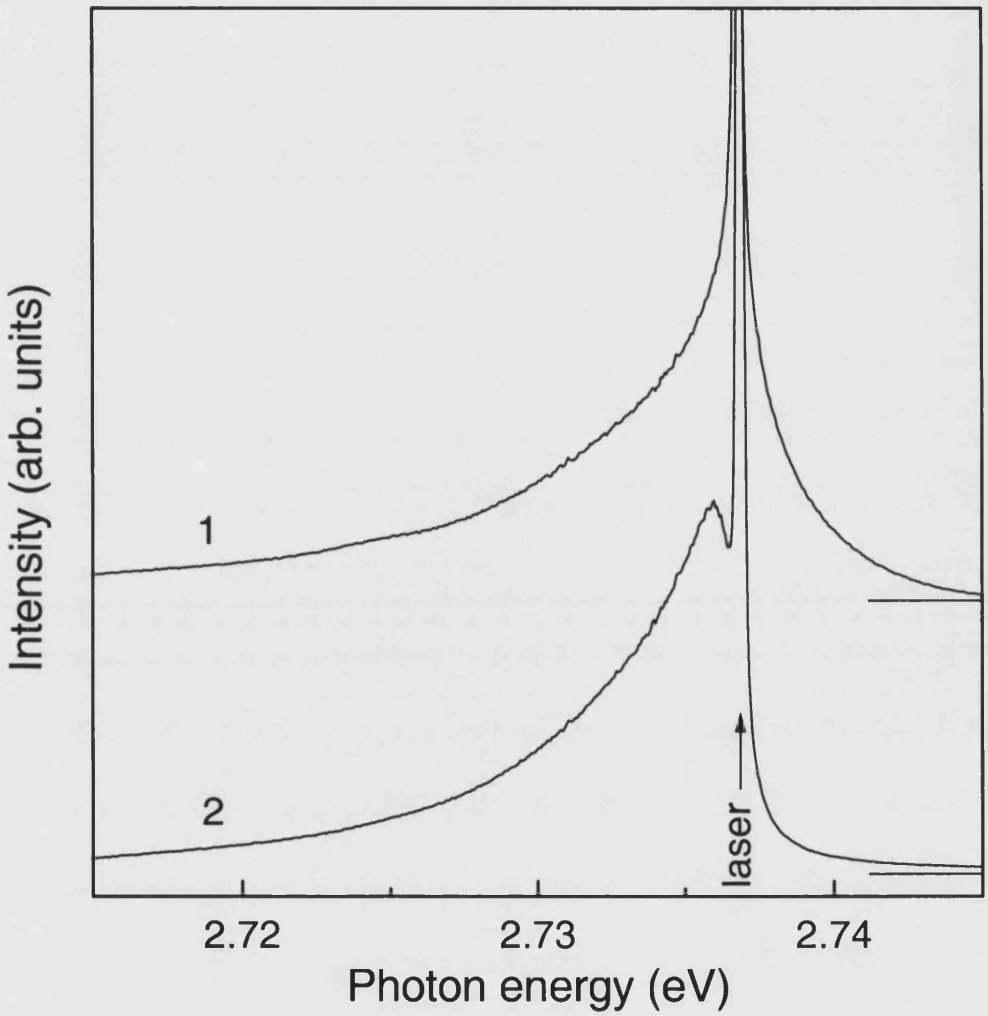

Figure 4.2: PL spectra of the sample B1485 (submonolayers) taken at 1) 50 K and 2) 1.5 K. $B = 0$ T. To compare the two spectra the laser excitation power was set equal in both cases and kept low to avoid strong heating of the sample in case (1).

the exciting laser is tuned across the PL band. A qualitatively similar picture is observed for the sample S0601 when the LX states are excited resonantly. We note that in this sample the peak-like feature almost disappears when the exciting laser is tuned in resonance with that part of the low energy side of the D^0X PL band where the overlapping of this band with the LX PL band is negligible. The low temperature PL spectrum (curve 2, Fig. 4.2) may represent the PL of selectively excited excitonic localized states [99]. The peak-like feature in this case can reflect the available density of localized states, possible relaxation processes or phonon assisted transitions (emission of phonons; the energy interval between the laser line and the peak-like feature suggests the involvement of acoustic phonons). The high temperature spectrum (spectrum 1, Fig. 4.2) shows the smearing of structure and appearance of the emission processes with the phonon absorption.

Voigt geometry. An application of a magnetic field leads to the further changes in the PL spectrum taken at liquid helium temperature. Again these changes are qualitatively similar for both of the samples. Fig. 4.3 shows spectra for two different laser energies within the PL band for the sample S0601. In this Figure the result of a Gaussian decomposition of the overall PL contour into two components related to LX and D^0X transitions is also shown. Note that the D^0X PL component is broader than the LX component. The additional broadening is more likely caused by the well known distribution of the D^0X binding energies across the QW and in the vicinity of the QW in the barriers [106]. In this geometry, two types of lines can be resolved on the Stokes and anti-Stokes sides under excitation in resonance with LX part of the overall PL contour: a sharp line (e) and a broader line (DE; seen as weak shoulder on the anti-Stokes side). These lines are better detected in cross linear $z(\sigma,\pi)\bar{z}$ and $z(\pi,\sigma)\bar{z}$ polarizations, but also can be seen under cross circular polarization conditions. At this stage we provisionally assign these lines to a manifestation of SFR scattering processes and will refer to the related spectra as SFR spectra. On the Stokes side the DE peak coincides with the PL peak-like feature discussed above. When the exiting laser is tuned towards the D^0X shoulder starting from the high energy side of the PL contour, the DE line passes the maximum of its intensity and gradually disappears. The e line is "present" in any spectral point of the PL contour. It is found that the intensity resonance profiles for the e and DE lines closely follow the PL profiles of the D^0X and LX components of the PL spectrum, respectively.

The measurement of the intensity resonance profiles for the e and DE lines taken

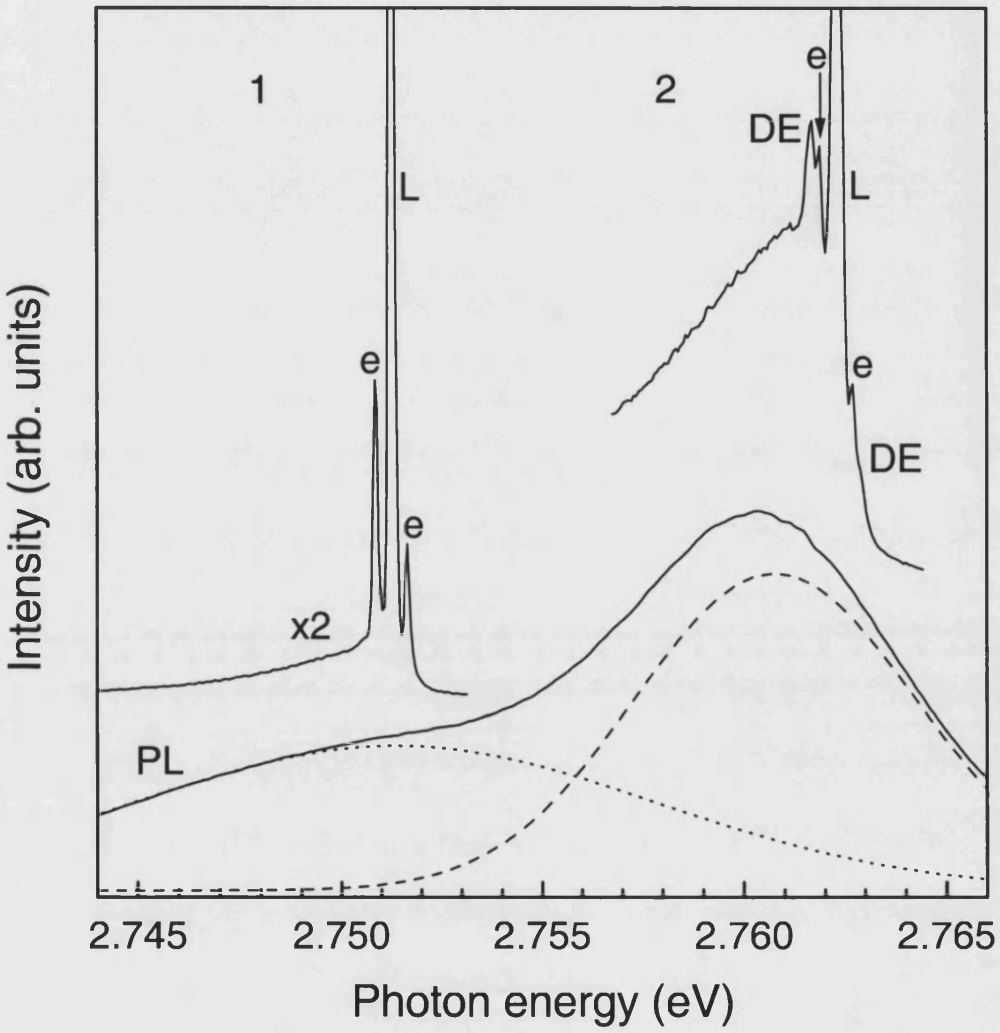

Figure 4.3: PL spectrum of the sample S0601 (QW) - solid curve marked PL. The dashed and dotted curves present a Gaussian decomposition of the overall PL contour into the LX and D^0X components, respectively. SFR spectra obtained in the Voigt geometry, $z(\sigma, \pi)\bar{z}$ at $B = 6$ T for two different excitation energies: 1 - 2.7513 eV and 2 - 2.7623 eV; in each case a broad background is due to PL. $T = 1.5$ K.

on the sample B1485 revealed the situation showed in Fig. 4.4. Again as in the case of the sample S0601 the intensity resonance profile peak positions for the e and DE lines do not coincide. In the present case the peak related to the e line lies higher in energy compared to the DE related peak - it occurs between the maxima of the PL and PLE spectra. The resonance profile of the DE line is remarkably asymmetric: it repeats closely the low energy slope of the PL spectrum, whereas its high energy slopes demonstrate an abrupt-like drop. The e line resonance profile is more symmetric. The abrupt drop can be caused by a reason which will be discussed in the next section. Here we only note that it can not be determined by the fact that the resonance profiles "overlap" with the PLE spectrum. A reabsorption correction is negligible; an estimated absorption for a 100 Å layer when taking the usual value for the excitonic absorption coefficient of 10^5 cm^{-1} is $\sim$ 0.1%. We also note, that in any spectral point "within" the PL band the relative intensity of the e and DE resonance profiles depend on the pumping intensity. Nevertheless, in the range of available pumping intensities we did not find any remarkable change of the shape of the resonance profiles.

Tuning the exciting laser energy E_{laser} within the PL bands of the samples B1485 and S0601 at a fixed magnetic field revealed that the DE line (Stokes and anti-stokes components) becomes slightly broader and that its shift from the laser line gradually increases with decreasing E_{laser}. For the sample B1485 this effect is seen more clearly compared to the sample S0601 due to the wider spectral range, where the DE line can be detected in this sample. The e line exhibits the same Raman shift independently of E_{laser} in both samples. Fig. 4.5 demonstrates this effect. We also found that both lines are well fitted by "single" Lorentzians in all spectral points across the corresponding resonance profiles in magnetic fields up to 14 T.

The two lines have different dependences of their intensities (peak and integral) on the strength of the magnetic field. The DE line exhibits a strong increase in intensity with the magnetic field; in our experiments it is detected only if $B > 2$ T (when exiting in the maximum of the DE line intensity resonance profile). The intensity of the e line does not show any significant dependence on B.

Some other experimental findings in the Voigt geometry which include, particularly the dependence of the Raman shifts of the e and DE lines on magnetic field will be given in the Discussion section.

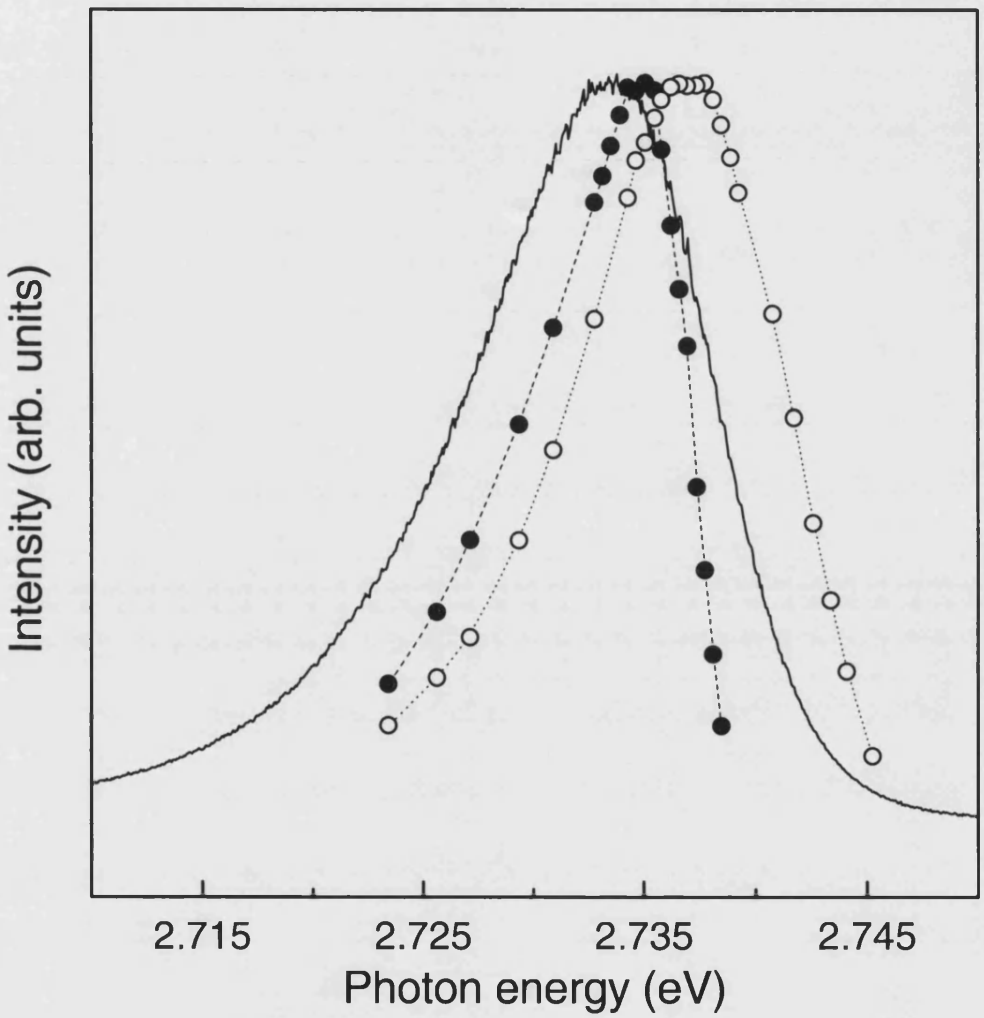

Figure 4.4: The solid line is a PL spectrum of the sample B1485 (submonolayers). The dotted (dashed) lines connect measurements of the scattering intensity resonance profiles (open (filled) circles) for the e (DE) line. $B = 6$ T, $T = 1.5$ K.

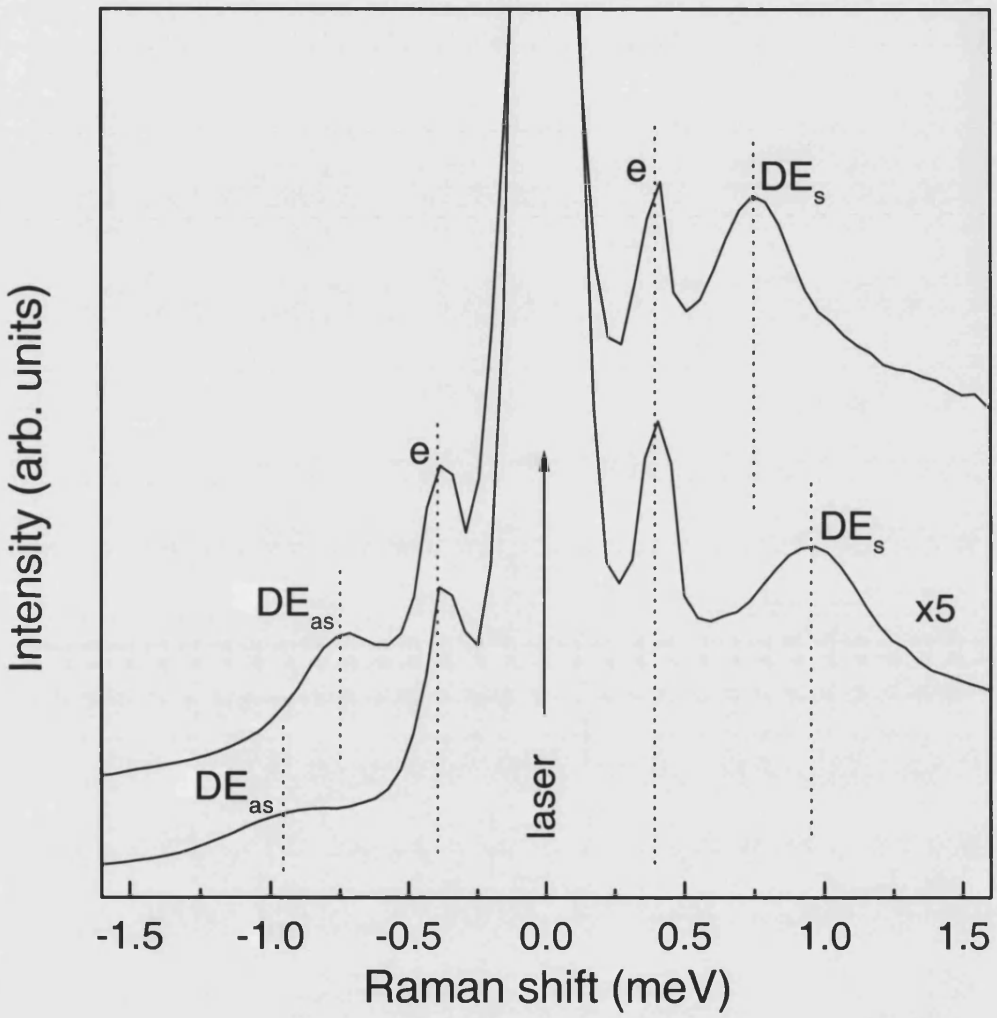

Figure 4.5: SFR spectra for laser energies within the broad PL band (sample B1485; submonolayers). The top and bottom spectra ware taken at, respectively $E_{laser} = 2.7353$ eV and 2.7248 eV in the Voigt geometry, $z(\sigma, \pi)\bar{z}$. $T = 1.5$ K, $B =$ 6 T. The subscripts (s) and (as) stand for Stokes and anti-Stokes, respectively. The lower spectrum was magnified 5 times before plotting. The vertical dotted lines are guides to the eye.

Faraday geometry. For both of the samples under excitation in the region of the LX PL bands we observed in a magnetic field one Stokes and one anti-Stokes lines, which are well fitted by a Lorentzian and have an equal shift from the laser line (within experimental error). These lines are strongly circularly polarized. The Stokes line is detected in cross circular $z(\sigma^+,\sigma^-)\bar{z}$ configuration, whereas the anti-Stokes component can be detected in the opposite $z(\sigma^-,\sigma^+)\bar{z}$ configuration. No signals are detected in both parallel circular configurations. This picture is demonstrated in Fig. 4.6 for the sample S0601. For both of the samples the intensity resonance profiles of these lines closely follow that of the DE line observable in the Voigt geometry. Also, their spectral width is comparable to that of the DE line (being much larger than the width of the e line). Similar to the case of the DE line, these lines show (i) their shifts from the exciting laser line are sensitive to the laser position E_{laser} within the LX PL band: the shift increases when E_{laser} decreases; (ii) their efficiency increases with the magnetic field.

The tilted field case. SFR experiments performed in a tilted magnetic field - the case when the angle θ between the direction of the magnetic field and the normal to the sample takes fixed values in the range $0^o < \theta < 90^o$ - often provide very useful information allowing to connect the results obtained in Faraday ($\theta = 0^o$) and Voigt ($\theta = 90^0$) geometries [9, 12, 14, 25, 105]. For example, such information can be helpful in an attempt to establish the nature of the observed signals. We performed such experiments on the samples B1485 and S0601 and found that again, as in the cases of Voigt and Faraday geometries, the SFR spectra of both of the samples possess a qualitative similarity.

Fig. 4.7 shows the Stokes parts of the SFR spectra of the sample B1485 (sub-monolayers) taken at a fixed magnetic field in the $z(\sigma^+,\sigma^-)\bar{z}$ configuration and at different values of θ. One finds that even a rotation of only several degrees of the magnetic field away from the Faraday geometry affects the Raman shift of the (only) line seen in this geometry (marked 1 in Fig. 4.7): the line moves towards the exciting laser line when θ is increased. Three new lines appear in sequence with increasing θ (marked 2, 3 and 4). As in the case of the line 1 their Raman shifts become smaller with increasing θ (see guides for an eye in Fig. 4.7). All four lines are clearly seen on the spectrum taken at $\theta = 45^o$. Additionally, at this angle in this polarization configuration a sharp line is detected. In the Voigt geometry this line coincides with the e line. Therefore we label this line with e

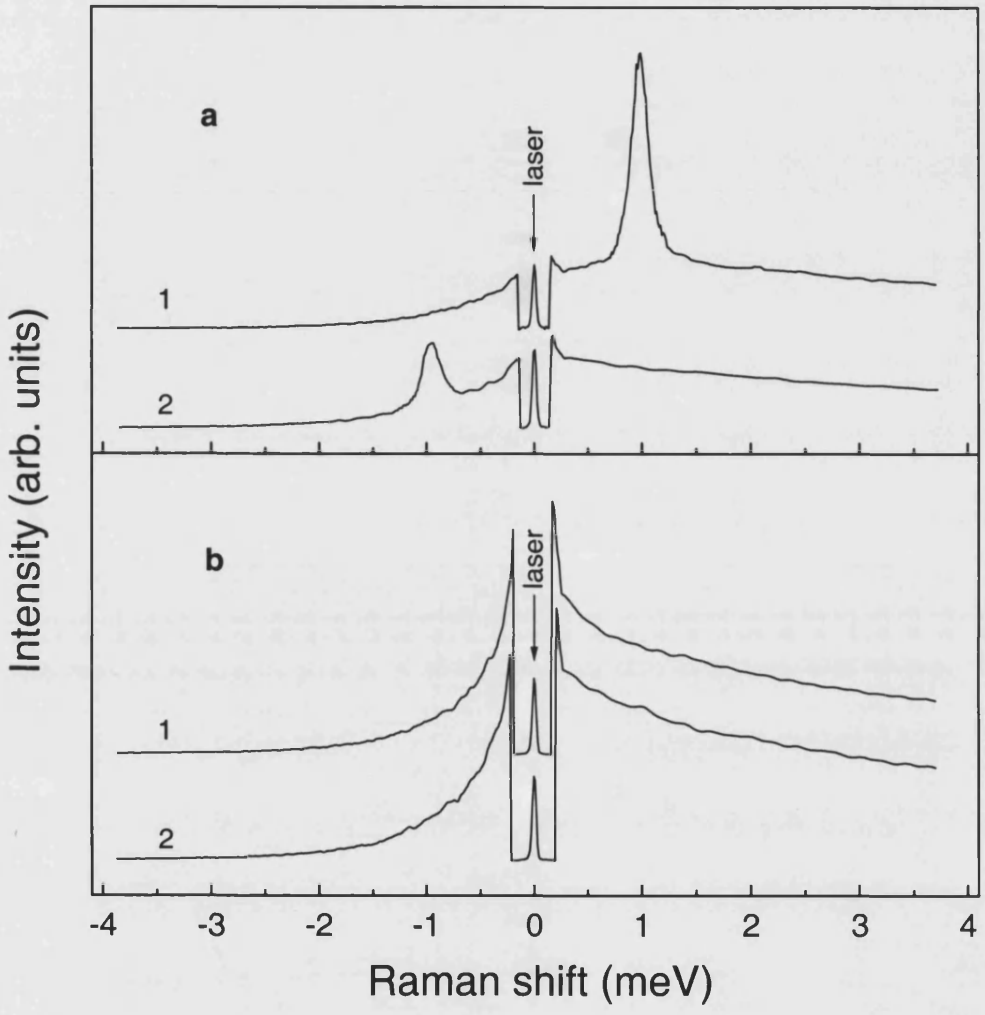

Figure 4.6: Sample S0601: SFR spectra measured in (a) cross circular $z(\sigma^+,\sigma^-)\bar{z}$ (spectrum 1), $z(\sigma^-,\sigma^+)\bar{z}$ (2) and (b) parallel circular $z(\sigma^+,\sigma^+)\bar{z}$ (1), $z(\sigma^-,\sigma^-)\bar{z}$ (2) polarization configurations. Faraday geometry, $B = 14$ T, $E_{laser} = 2.7619$ eV, $T = 4.5$ K. The "vertical" drop in intensity near the laser line is due to a neutral density filter inserted during the scan to attenuate the laser beam.

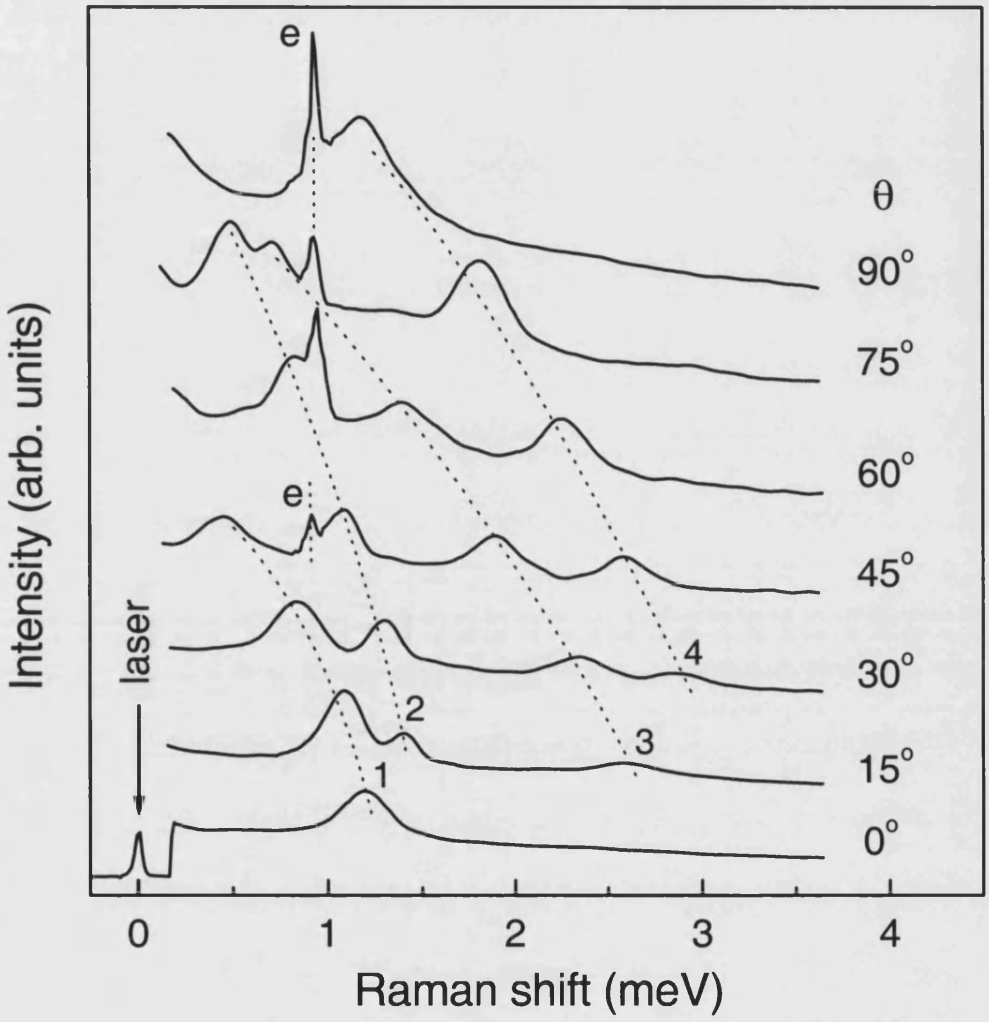

Figure 4.7: Sample B1485 (submonolayers): The Stokes parts of the SFR spectra measured at different angles θ between the magnetic field and the sample growth direction; $\theta = 0^o$ and 90^o correspond to the Faraday and Voigt geometries, respectively. $B = 14$ T, $E_{laser} = 2.7353$ eV, $z(\sigma^+, \sigma^-)\bar{z}$, $T = 4.5$ K. The dotted lines are guides to the eye. The label DE and numbers mark the observed lines.

at any θ. Continuous decrease of the Raman shift of the lines 1-4 with the increase of the angle leads to a consequent disappearance of the line 1-3 from the spectrum. The only line to "survive" is line 4. Becoming more intensive and slightly broader it coincides with the DE line in the Voigt geometry.

The influence of the polarization conditions is demonstrated in Fig. 4.8; as an example the SFR spectra of the sample S0601 taken at $\theta = 30^o$ are chosen. The line 1-4 are strongly circularly polarized. They appears on the Stokes side of the spectrum at $z(\sigma^+, \sigma^-)\bar{z}$ and on its anti-Stokes side at $z(\sigma^-, \sigma^+)\bar{z}$. In the parallel circular configuration $z(\sigma^+, \sigma^+)\bar{z}$ a new line marked 5 is observed (on the Stokes and anti-Stokes sides), whereas the line 1-4 are not detected. Again the line 5 intensity resonance profile almost coincides with that of the DE line. There are no lines detected in $z(\sigma^-, \sigma^-)\bar{z}$. The e line is detected in all possible configurations.

The intensities of the lines 1-4 at any θ depends on the strength of the magnetic field and follows closely the resonant profile of the DE line in both of the samples. We note, that although the lines 1-4 can be detected in any spectral point of the DE line resonance profile, their Raman shifts and relative intensities (peak and integral) are excitation energy dependent. The intensity of the e line increases with the angle and has its maximum at $\theta = 90^0$.

4.4 Discussion

In this section the first question one would like to discuss is "What is the nature of the observed lines?". The results presented above will be combined further with more experimental data, but already at this stage one can make a conclusion. This conclusion comes from the analysis of the intensity resonance profiles, which allow one to divide the lines at least in between two groups. One group consists of just the e line, while the second group includes the DE ($\theta = 90^o$) and 1-5 ($0^o \leq \theta < 90^o$) lines. These lines are now considered in more detail. PL band as well as the existence of the narrow (comparable with the exciting laser line width) Stokes and anti-Stokes components leads one to the suggestion, that this line corresponds to a SFR scattering process, namely of electrons

The e line. The fact that in sample S0601 (QW) the e line resonance profile

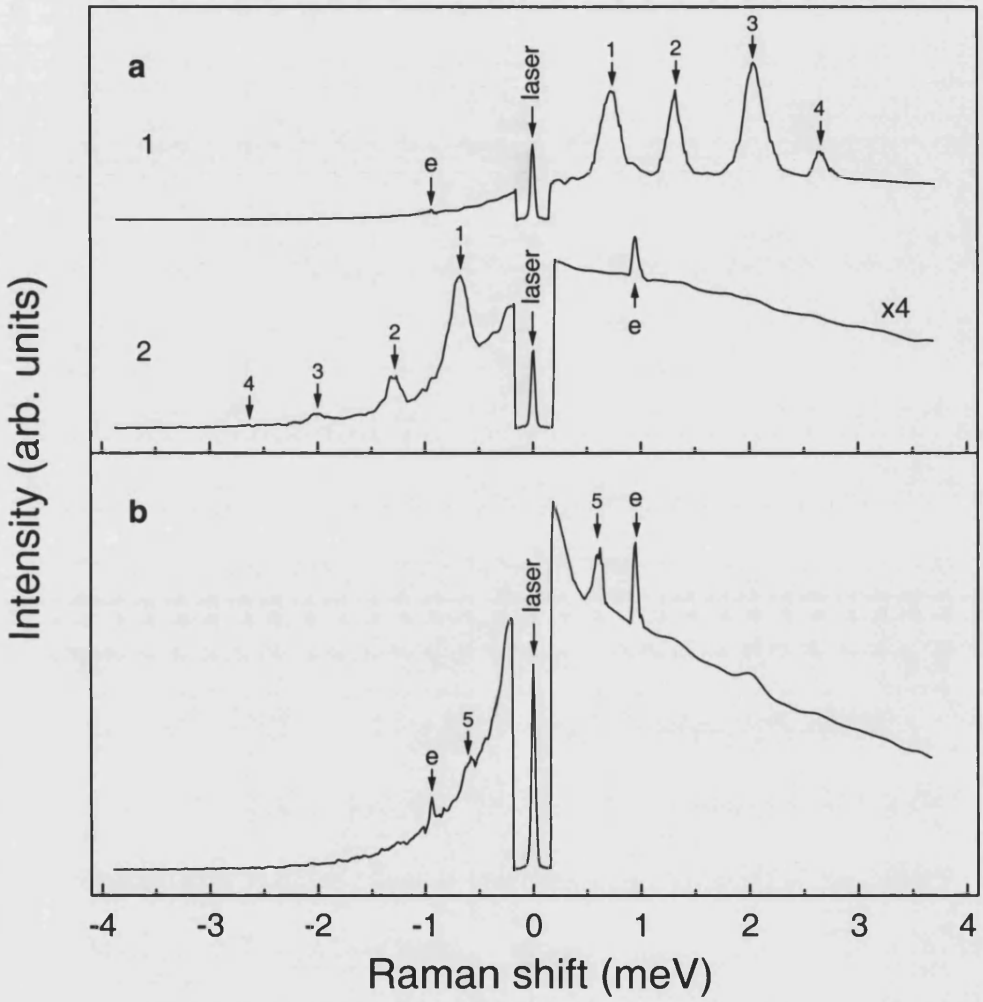

Figure 4.8: Sample S0601: SFR spectra measured in (a) cross circular $z(\sigma^+,\sigma^-)\bar{z}$ (spectrum 1), $z(\sigma^-,\sigma^+)\bar{z}$ (2) and (b) parallel circular $z(\sigma^+,\sigma^+)\bar{z}$ polarization configurations. $\theta = 30^o$, $B = 14$ T, $E_{laser} = 2.7619$ eV, $T = 4.5$ K. The label e and numbers mark the observed lines.

peak position (for Stokes and anti-Stokes) coincides with maximum of the D^0X bound to neutral donors. This suggestion is supported directly by the observation of the corresponding selection rules for this line. The magnetic field dependence of the e line shift from the laser line provides another conformation of our suggestion. This shift is very well described by Eq. 1.1 with $g = 1.19 \pm 0.02$ determined in the Voigt geometry. This value of the g-factor is close to that of an electron in bulk ZnSe and ZnSSe with low sulfur concentration (see Chapter 3 and Ref. [95]). The e line of the sample B1485 (submonolayers) demonstrate similar characteristics. From the magnetic-field dependence of its spectral position one found the g-factor value of 1.15 ± 0.02. This value coincides with that for electrons in bulk ZnSe. For all the samples studied, the value of g does not depend within experimental error on the excitation photon energy across the PL band.

In the case of the sample S0601 the electron participating in the scattering process is bound to a neutral donor located in the QW and the intermediate state is a D^0X state. In the case of the sample B1485 the situation is not so well determined. It was found (see section 4.3.1) that for the CdSe/ZnSe submonolayer structures the entire PL band is formed by excitons localized at CdSe insertions. Then, explaining the e line as a line due to SFR of an electron bound on a neutral donor one has to accept the presence of some contribution of D^0Xs to the PL. However, it is reasonable to expect that in our case (shadow donors only) this contribution should be weak - the concentration of donors inside the very small CdSe-rich island-like volumes or inside the very thin QW layer in between them is small. Additionally, one can propose an alternative type of SFR scattering of an electron. An electron bound at a neutral donor located in the ZnSe barrier regions by means of tunneling can have some amplitude within the CdSe submonolayer insertions. The formation of a negatively charged exciton (X^-; or - trion) [107] acting as an intermediate state in the SFR scattering of an electron is then possible.

The first impression based on our study of the dependence on composition of the electron g-factor in ZnCdSe epilayers (Chapter3) suggests that in the present case we should expect lower values of g than that observed. Such a similarity to the bulk ZnSe value may result from strong penetration of the exciton wave function into ZnSe and ZnSSe barriers in the samples B1485 and S0601, respectively. To check this statement we performed appropriate measurements using a structure with a thicker QW. We found that in this single 50Å ZnCdSe/ZnSe QW of 20%

of Cd structure the electron g-factor is indeed lower (1.10 ± 0.02). The slightly higher value of g measured in the sample S0601 compared to that of bulk ZnSe is in consistence with the results of Ref. [95], where an increase of the electron g-factor with S content in ZnSSe alloy was experimentally confirmed. Analyzing the electron g-factor in QWs case we also have to consider the influence of the reduction of the point symmetry from T_d (bulk) to D_{2d} (QWs). This reduction leads to the anisotropy of the electron g-factor, which can be expressed in the frame of two-band $\mathbf{k} \cdot \mathbf{p}$ method via the energetic heavy-light hole splitting by[1] [14, 18, 108]

$$\Delta g = g^{\perp} - g^{\parallel} \approx \frac{P^2}{E_{ex}^2} \Delta E_{lh-hh}, \tag{4.1}$$

where $g^{\perp}(g^{\parallel})$ is the electron g-factor measured in the Voigt(Faraday) geometry, P^2 corresponds to the squared momentum matrix element connecting the conduction (Γ_6) and the valence (Γ_8) bands, E_{ex} is the excitonic transition energy and ΔE_{lh-hh} the heavy-light hole splitting. Such an anisotropy was experimentally found in QW systems CdTe/CdMnTe and ZnSe/ZnMgSSe [14, 18]. According to Eq. 4.1, in our case, the anisotropy should be in the range of 0.1-0.2. Although some indication of the anisotropy of g was observed in the sample S0601 ($g = 1.17 \pm 0.02$ at $\theta = 45^o$), due to a very strong overlapping the e line with the other lines observed at $\theta < 90^o$, we were unable to perform a precise analysis of this effect.

We can only speculate in order to explain the position of the e line resonance profile of the sample B1485 - unlike the case of the sample S0601 the peak of the resonance profile lies on the high energy side of the PL. Clearly, the binding of a localized exciton by a donor should lead to an additional shift of the LX PL band and the related SFR resonance profile to lower energies. This fact indicates that in the sample B1485 a part of photoexcited excitons are trapped by donors which are not located in the parts of a strong localizing potential. Due to the low concentration of donors the related PL is weak and is overwhelmed by the much stronger PL of LXs. The binding of excitons by these donors leads to a shift of 6 meV to lower energies relative to the 1hh peak of the PLE spectrum (see Fig. 4.1). Similar arguments can be used in the case of charged exciton mediated SFR scattering.

[1] In some cases the much more exact fit to the experimental date is achieved by using the more complicated expression derived with taking into account the wave function spread into the barrier region [18].

The DE line and lines 1 – 5. An attempt to provide an explanation of the origin(s) of such a number of the observed line is a remarkable challenge. We start here from the two experimental facts, which hold for both of the samples. The first fact is that the intensity resonance profiles of these lines very closely follow each other. The second one is that line 4 smoothly turns into the DE line when θ approaches 90^o. It is possible, at this point, to suggest that all the lines are manifestations of different subsystems of one and the same system. The general situation - when all the subsystems can be seen simultaneously - then corresponds to a certain θ "in between" Voigt and Faraday geometries. What is this system? At first instance we can consider at least three possibilities. They are - a single bound/localized electron, a single bound/localized hole or a localized exciton. Simple arguments help to rule out the involvement of bound/localized electrons as well as bound/localized holes. In the case of electrons only one line (counting Stokes and anti-Stokes signals together) corresponding to a transition between two spin states would be detected. We do detect this line (line e). A possible situation when in a SFR spectrum several equidistant lines present due to a multiple SFR scattering of electrons (overtones) can be easily recognized and it is not realized in our case. The same argument is applied to bound/localized holes (in our case we have to consider a heavy hole). Also, since ZnCdSe/ZnSe structures are normally n-type (if not intentionally doped with acceptors) it is unlikely that such strong lines observed in our spectra relate to holes. In contrast, an exciton in a magnetic field possesses a more complicated spin structure. So, the last case which we have to consider in detail belongs to excitons, localized in our case. The involvement of localized excitons is strongly supported by the fact that the spectral positions of the resonance profiles of all the lines correspond to that of PL bands of localized excitons in both of the samples. If we accept this concept, then for example the abrupt-like drop of the high energy side of the resonance profile of the sample B1485 (see Fig. 4.4) can be explained by the idea that the lifetime of the corresponding excitons is shorter compared to that of excitons "from" the low energy side of the PL band [103] and therefore they are not so efficient in the scattering process. Another result in favor of localized excitons comes from the magnetic field dependences of the intensities for the lines DE and 1-5. These dependences demonstrate one common feature - a strong increase of the intensities with the magnetic field. Fig. 4.9 (a) presents a result for the case of the DE line (We should note here, that the diamagnetic shift of the maximum of the LX PL band is less than 1 meV in $B = 14$ T. The value of this shift is much smaller than the full width of the LX PL band (15

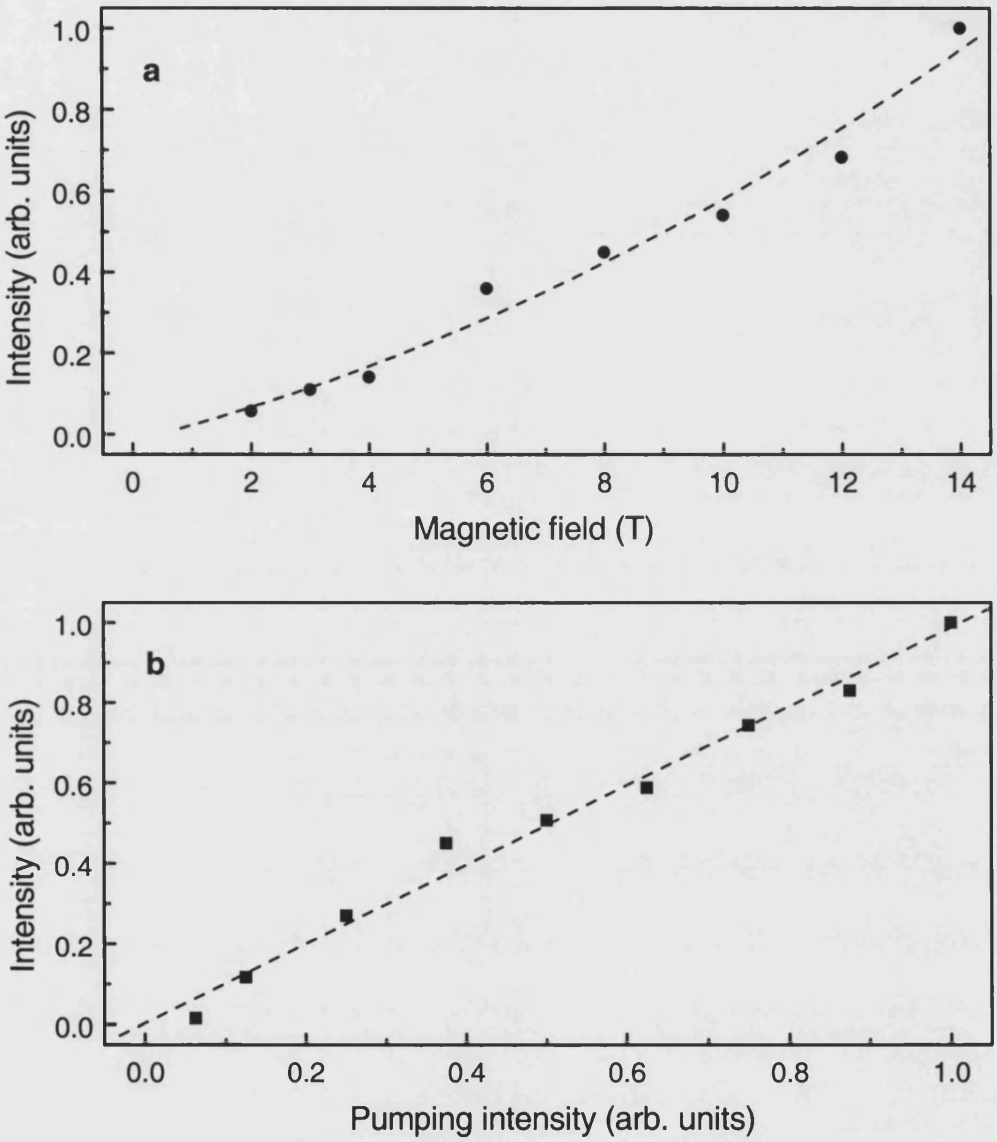

Figure 4.9: Sample B1485: Dependences of the integrated intensity of the DE line on (a) magnetic field strength (Stokes part + anti-Stokes part; $T = 4.5$ K) and (b) pumping intensity at a fixed magnetic field of 6 T (Stokes part only; $T = 1.5$ K). $E_{laser} = 2.7375$ eV. In case (b) the maximum value of pumping intensity was ~ 1 W/cm^2.

meV for the sample B1485). Therefore measuring the dependences we "test" excitons localized in a very narrow energy interval). Such a behaviour can be explained, in principle, by the well known effect of an "additional" localization of the excitons due to shrinking the exciton Bohr radius ($\sim 1/\sqrt{B}$). An increase of the exciton oscillator strength with the magnetic field due to the magnetic confinement effect can also be taken here into account [109]. In general, a modelling of such dependences is a complicated task, which may demand a consideration of a whole set of different mechanisms. We will come back to this point later in our discussion. Fig. 4.9 (b) shows also that in the range of available pumping intensities the intensity of the DE line does not exhibit any super(sub)-linear or saturation behaviour. The same result holds for the line 1-5.

The arguments given above may serve just as a basis to support the concept of localized excitons. A strong support for this concept may come from another experimental result we have in hand, but have not considered so far: the shifts of all the lines are not proportional to B. This kind of magnetic field dependence is unique enough for SFR spectroscopy and it is reasonable to expect that the ability to model such a behaviour for such a number of lines in the frame of a certain concept will provide an unambiguous evidence of its correctness. Thus, to go ahead we have to consider an exciton in a magnetic field or if to say more precisely - its fine structure.

Excitonic fine structure. For a (100)-grown quantum well the growth direction (z) is taken as the quantization axis for the angular momentum and the relevant symmetry is D_{2d}. The conduction band is s-like, with two spin states $S_z = \pm 1/2$. The upper p-like valence band is split into a heavy hole band and a light hole band with the total angular momentum projection $J_z = \pm 3/2$ and $J_z = \pm 1/2$, respectively. The corresponding excitonic states are the heavy hole and light hole excitons (see section 2.5.1 of Chapter 2). We will restrict our attention only by the ground state of 1e-1hh of a heavy hole exciton (1hh exciton). This is because in our case (i) the excitation takes place in resonance with the PL band formed by localized 1hh excitons and (ii) there is a large energy separation between the 1hh and 1lh excitons in the investigated samples. We assume also that the 1hh-1lh splitting is much greater than any Zeeman splittings (a value of ~ 3 meV for the 1hh exciton obtained from polarized PL measurements at $B = 14$ T). in the 1hh and 1lh excitons - then the possible (in the opposite case) magnetic field-induced admixture of the 1lh state to the 1hh state can be neglected.

In the zero-field case the ground state of a heavy hole exciton in zinc-blende quantum wells is fourfold degenerate and is characterized by the angular momentum component $M_z = S_z + J_z$ with the basis set of four states $|\pm 1>$ and $|\pm 2>$. In this representation, the excitons with $M_z = \pm 1$ are dipole-allowed (optically active or "bright" excitons) and the excitons with $M_z = \pm 2$ are forbidden for optical transitions (optically inactive or "dark" excitons). The exchange interaction between an electron and a hole leads to an appearance of a fine structure of the exciton ground state even at $B = 0$.

The exchange interaction of excitons in bulk and low dimensional semiconductors always attracts much attention. Recent comprehensive theoretical studies can be found in Refs. [110, 111, 112, 113]. The Hamiltonian H_{e-h} of the electron-hole exchange in bulk semiconductors is presented as a sum of two exchange terms. In the **k**-space representation one of the exchange terms is an analytic function, whereas the other exchange term is a nonanalytic function at $\mathbf{k} = 0$. The exchange interaction can also be divided in real space into a short-range (SR) part and a long-range (LR) part. The SR part can be defined as the electron-hole exchange integral within a Wigner-Seitz unit cell, whereas the LR part is determined as a contribution to the exchange integral coming from different cells (it gives rise, for example, to a splitting between longitudinal and transverse excitons for $\mathbf{k} = 0$). These two classifications are closely related, but not exactly the same - the LR part can contain some analytic components [114, 115]. In the absence of translational symmetry, the distinction between SR and LR contributions in not so straightforward.

For 1hh excitons in QWs the influence of the electron-hole exchange interaction results [116] (i) in the splitting of the fourfold degenerate level into two doublets - a radiative doublet $|\pm 1>$ and a nonradiative doublet $|\pm 2>$ (A-N splitting); the $|\pm 1>$ doublet is shifted above the $|\pm 2>$ one (ii) in the splitting of the radiative doublet (A-A splitting) and (iii) in the splitting of the nonradiative doublet (N-N splitting)[2]. The A-N splitting is determined by the SR exchange which is proportional to the product of hole and electron spin operators **JS**. The SR exchange (Kohn-Luttinger) Hamiltonian includes also a high order term,

[2]Here the labels A and N stand for the optically active (radiative) or optically nonactive (nonradiative) states, respectively.

proportional to $\mathbf{J}^3\mathbf{S}$ [117]

$$H_{e-h}^{SR} = -\sum_{i=x,y,z} (aJ_iS_i + bJ_i^3S_i), \tag{4.2}$$

where a and b the spin coupling constants, the indexes denote a coordinate system ((x,y) in the QW plane). This cubic term responsible for the N-N splitting and contribute also to the A-A splitting. The LR exchange vanishes for (intrinsic) excitons at $\mathbf{k} = 0$ in a "perfect" QW [110], but may contribute to the A-N and A-A splitting if an exciton bound to an ionized impurity or isoelectronic trap or at presence of an anisotropic localizing potential [118]. Both the A-A and N-N splittings are estimated to be much smaller than the A-N splitting. This is a general schema of the influence of the electron-hole exchange interaction on the 1hh excitonic state.

Due to the Zeeman splittings of electron and hole spin states, an external magnetic field can further modify the structure of the exciton ground state. Thus, the corresponding Hamiltonian (in an arbitrarily directed magnetic field and in a valence hole representation) is [117]

$$H_{ex} = H_e + H_h + H_{e-h}, \tag{4.3}$$

where

$$H_e = \mu_B \sum_{i=x,y,z} g_{e,i}S_iB_i \tag{4.4}$$

and

$$H_h = -2\mu_B \sum_{i=x,y,z} (\kappa_iJ_i + q_iJ_i^3)B_i \tag{4.5}$$

describe the Zeeman splitting of the electrons and holes, respectively. In these expressions κ and q are the (Luttinger) Zeeman splittings constants for the hole. The electron g-factor is expected to show a small variation with field direction [108]. The heavy hole g-factor g_h is strongly anisotropic, being almost zero by symmetry ($\kappa \gg q \approx 0$) for a field perpendicular to the growth axis [117]

$$g_{h,x} = 3q_x \approx 0, \qquad g_{h,y} = -3q_y \approx 0, \qquad g_{h,z} = -2\kappa_z - \frac{9}{2}q_z \approx -2\kappa_z \tag{4.6}$$

Often Eq. 4.5 is written by using an effective heavy hole spin quantum number $\tilde{S}_z = \pm 1/2$ describing the heavy hole states $J_z = \pm 3/2$, so that we have for the hole Hamiltonian $H_h = -g'_{h,z}\mu_B\tilde{S}_z$ with $g'_{h,z} = 3g_{h,z} = -6\kappa_z$.

We will label the value of the A-N-, A-A- and N-N exchange splittings as δ_0, δ_r and δ_{nr}, respectively. For the case of a QW in general, the Hamiltonian H_{ex} can be written in a matrix form, in the order of the basis states $|+1>$, $|-1>$, $|+2>$, $|-2>$ as [119, 120]

$$H_{ex} = \begin{pmatrix} \Omega_{BE}\cos\theta & \delta_r/2 & \Omega_e\sin\theta & \Omega_h\sin\theta \\ \delta_r/2 & -\Omega_{BE}\cos\theta & \Omega_h\sin\theta & \Omega_e\sin\theta \\ \Omega_e\sin\theta & \Omega_h\sin\theta & \Omega_{DE}\cos\theta - \delta_0 & \delta_{nr}/2 \\ \Omega_h\sin\theta & \Omega_e\sin\theta & \delta_{nr}/2 & -\Omega_{DE}\cos\theta - \delta_0 \end{pmatrix}, \quad (4.7)$$

where $\Omega_{BE} = (3g_h^{\parallel} - g_e^{\parallel})\mu_B B/2$, $\Omega_{DE} = (3g_h^{\parallel} + g_e^{\parallel})\mu_B B/2$, $\Omega_e = g_e^{\perp}\mu_B B/2$, $\Omega_h = 3g_h^{\perp}\mu_B B/2$ (BE(DE) marks the term corresponding to the bright(dark) excitonic state); $g_e^{\parallel}(3g_h^{\parallel})$ and $g_e^{\perp}(3g_h^{\perp})$ are the longitudinal and transverse electron(hole) g-factors, respectively. The Hamiltonian H_{ex} may include an additional term of a low-symmetry perturbation [116]. In general, it causes mixing of the excitonic states (in $B \neq 0$), which may lead to an appearance of an anticrossing of the different spin levels in the excitonic fine structure. Such a perturbation may act on the electron and hole spins independently. One of the examples is when the excitonic states are mixed by hyperfine interaction between electrons and nuclear spins [121].

Raman shifts of the DE and lines $1-5$. At this stage of our discussion we are convinced, at least intuitively, that such a rich fine structure of the excitonic ground state can be "connected" to the rich structure observed in the spectra. We therefore, consider more closely the Hamiltonian H_{ex} given by Eq. 4.7. First of all we simplify the Hamiltonian by taking $g_h^{\perp} = 0$ - it is reasonable: see Eqs. 4.6. We also take $\delta_r = \delta_{nr} = 0$. The last is done because it is dictated by the following facts: these values are not known even for bulk ZnSe(CdSe) and they are expected to be small compared to δ_0, which is 0.2 meV for bulk ZnSe and 0.13 meV for bulk CdSe [90]). By doing this we also avoiding two possible adjustable parameters in the following calculation/fitting procedure. This simplification should be considered at least as a first approximation to our task. The Hamiltonian now provides four equations for the energy levels $E_{1,2}$ and $E_{3,4}$, which correspond to the spin states $|\pm 1>$ and $|\pm 2>$, respectively:

$$E_{1,2} = \frac{1}{2}(\pm 3g_h^{\parallel}\mu_B B\cos\theta + \sqrt{(\delta_0 \mp g_e^{\parallel}\mu_B B\cos\theta)^2 + (g_e^{\perp}\mu_B B\sin\theta)^2}) \quad (4.8)$$

$$E_{3,4} = \frac{1}{2}(\pm 3 g_h^{\parallel} \mu_B B \cos\theta - \sqrt{(\delta_0 \mp g_e^{\parallel} \mu_B B \cos\theta)^2 + (g_e^{\perp} \mu_B B \sin\theta)^2}) \qquad (4.9)$$

Fig. 4.10 (a) shows 1hh exciton energy level diagrams calculated according to Eq. 4.8 and Eq. 4.9 for $\theta = 30^o$. We see that there are six possible transitions between the levels (indicated by the arrows 1-6) in which there occurs a change of total angular momentum component of $\Delta M_z = |M_z - M_z'|$; M_z and M_z' take the value ± 1 and ± 2 as appropriate. ΔM_z is equal to 1 for the spin-flip of an electron, to 3 for the spin-flip of a hole and to 2 or to 4 for the simultaneous spin-flip of both particles within the exciton, in opposite or the same directions respectively ($\Delta M_z = 2$ corresponds then to the flip of the angular momentum of the bright exciton, whereas $\Delta M_z = 4$ to the that of a dark exciton). We have to point out here that due to magnetically-induced mixing the bright and dark states are not totally pure $|\pm 1>$ and $|\pm 2>$ states ($B_x \neq 0$). This means that the dark states become directly visible in the optical spectra and the intensity of the corresponding transitions are stronger when the magnetic field is stronger.

Equations describing the energies of the transitions 1-6 on the magnetic field can be obtained from Eq. 4.8 and Eq. 4.9. We used these equations to fit the Raman shifts of the DE and 1-5 lines. Fig. 4.10 (b) shows the result of the fitting for the sample B1485 (submonolayers). We found that the Raman shifts of all the lines can be fitted very well in such a way by a single set of parameters $g_e^{\parallel}$, $g_e^{\perp}$, $3g_h^{\perp}$ and δ_0. A least-squares fitting procedure for the Raman shifts of the lines 1-5 measured under excitation at the maximum of the intensity resonance profile gives (averaged for all the lines) $g_e^{\parallel} = g_e^{\perp} = 1.18 \pm 0.02$, $3g_h^{\perp} = 2.7 \pm 0.2$ and $\delta_0 = 0.68 \pm 0.03$. Using these values we were able to obtain fits of the same quality to the data corresponding to different angles θ varying from the Faraday geometry to the Voigt geometry (Fig. 4.11). The electron and hole g-factors obtained from the fitting are very close to those of electrons and holes in bulk ZnSe and differ strongly from the corresponding values for bulk CdSe [9, 10, 11, 90]. From the analysis of the experimental data of the Faraday geometry we determined directly the bright exciton g-factor of $\sim 1.5 \pm 0.1$. Again this value is very close to the value of the bulk ZnSe exciton g-factor [90]. Such a similarity, as in the case of the g-factor related to the e line, may result from strong penetration of the exciton wave function into ZnSe barriers. Contrary to the g-factors, the A-N splitting δ_0 exhibits an increase of about 3.5 times over the bulk ZnSe value (this value corresponds to $E_{laser} = 2.7353$ eV). This is a well known effect for low-dimensional systems being attributed to the larger overlap of the electron and hole wave functions compared to the bulk case [122].

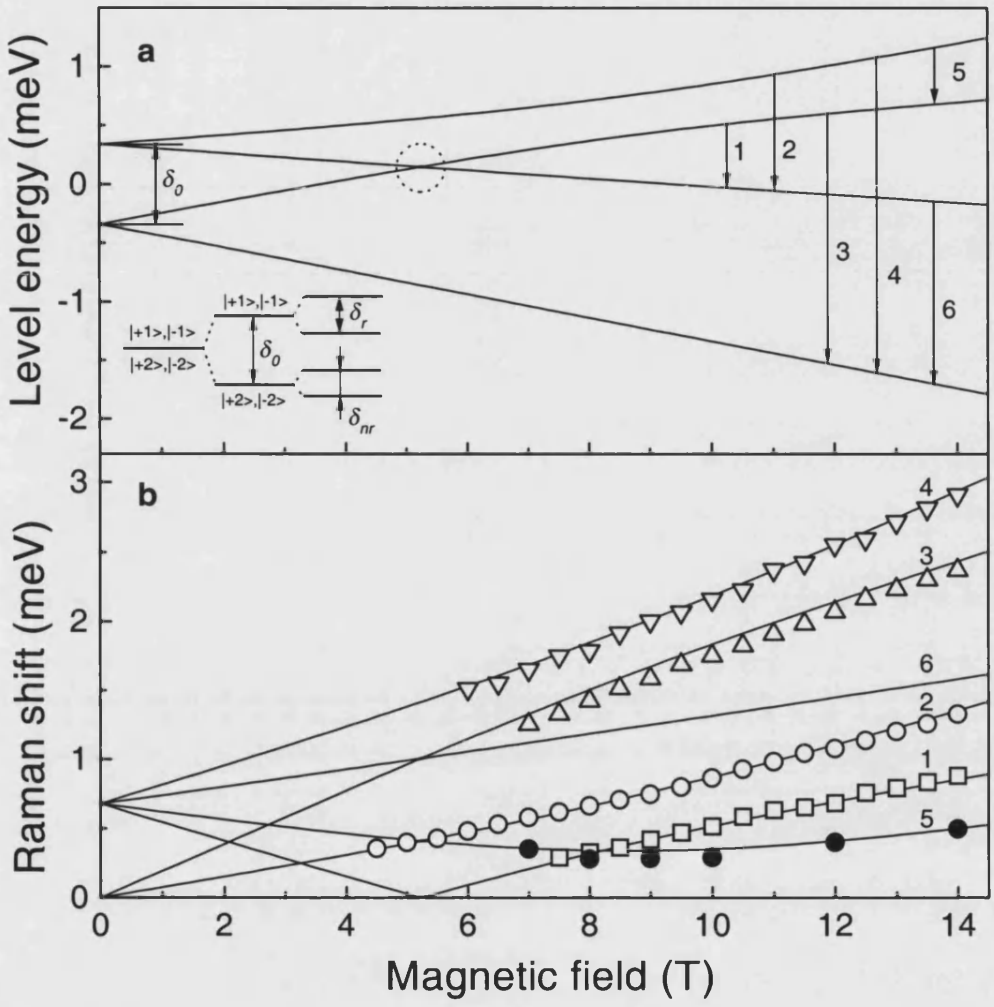

Figure 4.10: Sample B1485: (a) Exciton energy levels obtained according to Eq. 4.8 and Eq. 4.9 for $\theta = 30^o$. The numbered arrows show the spin transitions; the dotted circle indicate the possible level anticrossing (see text). The inset shows the general picture of the influence of the electron-hole exchange interaction on the heavy hole exciton ground state fine structure ($B = 0$ T); the splittings δ_r and δ_{nr} are exaggerated compared to the δ_0 splitting. (b) Calculated Stokes Raman shifts corresponding to the transitions 1-6 of the plot (a) (numbered solid lines). The symbols represent the experimental data ($E_{laser} = 2.7375$ eV) for the lines: 1 - squares, 2 - circles, 3 - up triangles, 4 - down triangles, 5 - solid circles.

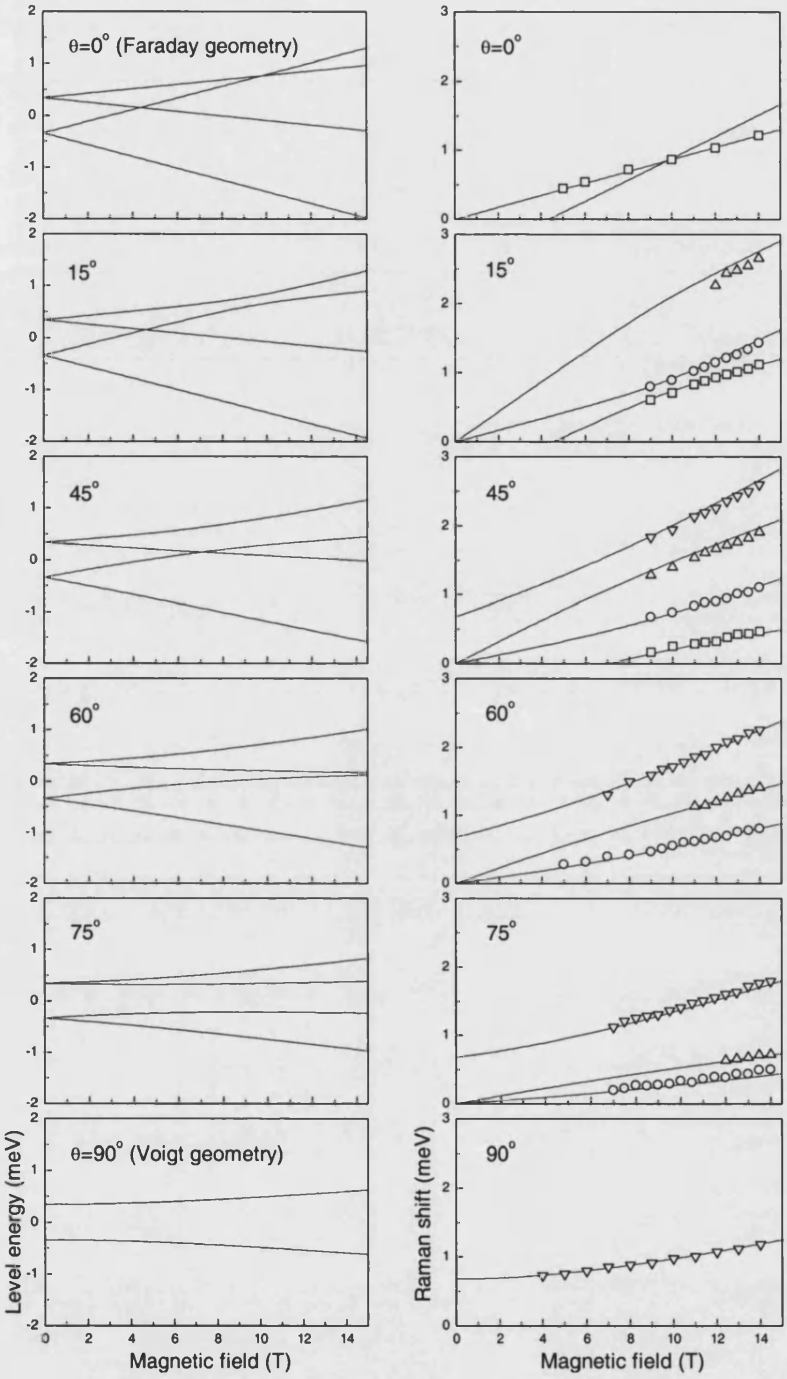

Figure 4.11: Sample B1485: The left column represents the level energy plots and the right column - the Stokes Raman shift plots (see text).

We did not observe the transition marked by the arrow 6 in Fig. 4.10 (a), which is expected in $z(\sigma^-,\sigma^-)\bar{z}$ polarization. Nevertheless, the high quality of the fits obtained for all the other transitions provides a strong evidence of the correctness of our "excitonic" concept. It also indicates, that at least for high enough magnetic fields ($B < 3$ T in our case) the A-A and N-N splittings do not affect the 1hh exciton fine structure noticeably. The same conclusion is valid for the possible anticrossing of the levels E_2 and E_3 due to the low-symmetry perturbations (indicated by the dotted circle in Fig. 4.10 (a)). It also signifies the unimportance of the heavy-light hole coupling and justifies the restriction to the above 4×4 Hamiltonian for the heterosystem considered.

We also successfully fitted the experimental data corresponding to the lines DE and 1-5 of the sample S0601 (QW) as well as the data of the other ZnCdSe/Zn(S)Se QWs (QW widths range from 35 Å to 55 Å). They all showed the same result concerning the values of the electron, hole and exciton g-factors - these values are close to the corresponding values of barrier material. The only noticeable difference comes from the value of the A-N splitting. For example, from the spectra obtained by excitation in resonance with the maximum of the intensity resonance profile we found for the sample S0601 δ_0 to be 0.55 meV. We also found that the value of δ_0 is sensitive to the "position" of the excitation energy E_{laser} within the LX PL band. Thus, a comparison of δ_0 for different samples is not straightforward. This also indicates that by changing E_{laser} we "test" excitons belonging to different localizing states, or in another word, to sites of different localization energies. We will consider this aspect in detail.

Dependence of the A – N splitting on the exciton localization energy. We will concentrate here on the results provided by the sample B1485 because the intensity resonance profile of the excitonic signals was found to be the widest compared to that of the other samples. For our analysis we choose the data of the Voigt geometry. This is reasonable - we observed only one excitonic line DE (Stokes and anti-Stokes being counted together) in this geometry and therefore the fitting error is minimized. We also will refer the exciton localization energy (E_{loc}) to the free-exciton energy ($E^{hh} - E_{laser}$) known from the PLE measurements.

As it is seen in Fig. 4.5 the DE line shift increases when E_{laser} decreases. Employing an expression for the shift of the DE line on the magnetic field derived

from Eq. 4.8 and Eq. 4.9 ($\sqrt{\delta_0^2 + (g_e^{\perp}\mu_B B)^2}$), we find a linear variation of the zero field A-N splitting when E_{laser} is scanned across the CdSe submonolayer related PL band and an almost two-fold increase of δ_0 at the lowest excitation energies. These results are shown in Fig. 4.12. The values of δ_0 found in this particular sample are 3 - 10 times larger than in bulk CdSe and ZnSe [90]. We attribute this enhancement to the larger wave function overlap for the more strongly localized excitons in the low-energy LX PL tail. While it is qualitatively clear that the A-N splitting should vary strongly with the exciton radius (and thus the exciton localization energy) due to its strong sensitivity to changes in the wave function overlap, the exact functional form for this relation cannot be easily obtained. Note that this *increase* of δ_0 for *lower* excitation energies is in contrast to the behavior of quantum dots with full three-dimensional confinement [122], where a *decrease* of the exchange splitting with increasing dot size, i. e., with lower exciton energy, is expected. Such an effect has been observed recently in pure CdSe dots [123].

We have to mention here that the best fit to the data revealed a slight, but gradual increase of $g_e^{\perp}$ with increasing E_{loc}. The g-factor of 1.18 ± 0.02 and of 1.42 ± 0.04 were found for $E_{loc} \approx 9$ meV and 32 meV, respectively. We see that the later value exceed well the ZnSe (and CdSe) value. Perhaps this exceeding of the bulk value originates from the anisotropy of the g-factor ($g^{\perp} \neq g^{||}$) induced by the heavy-light hole splitting [18]. This effect needs further investigation.

The linear variation of the A-N splitting with the exciton localization energy is an exciting result itself, which is interesting to explain. Is it a feature of excitons localized by potential fluctuations in general or should an influence of the "low-dimensionality" be taken into account? At present we are not able to provide an explanation - more experimental data obtained on different systems as well as theoretical studies are necessary. Nevertheless, we consider a speculative approach to this task suggested by Klochikhin [124]. If the exchange splitting of atom states is equal to δ_0^{at}, then the short range electron-hole exchange splitting[3] for a free exciton will be equal to the value

$$v_0 |\phi(0)|^2 \delta_0^{at}, \tag{4.10}$$

where v_0 is the volume of the elementary cell and $\phi(r)$ is the wave function of the

[3]We assume that the A-N splitting is mostly contributed by the short range electron-hole exchange interaction.

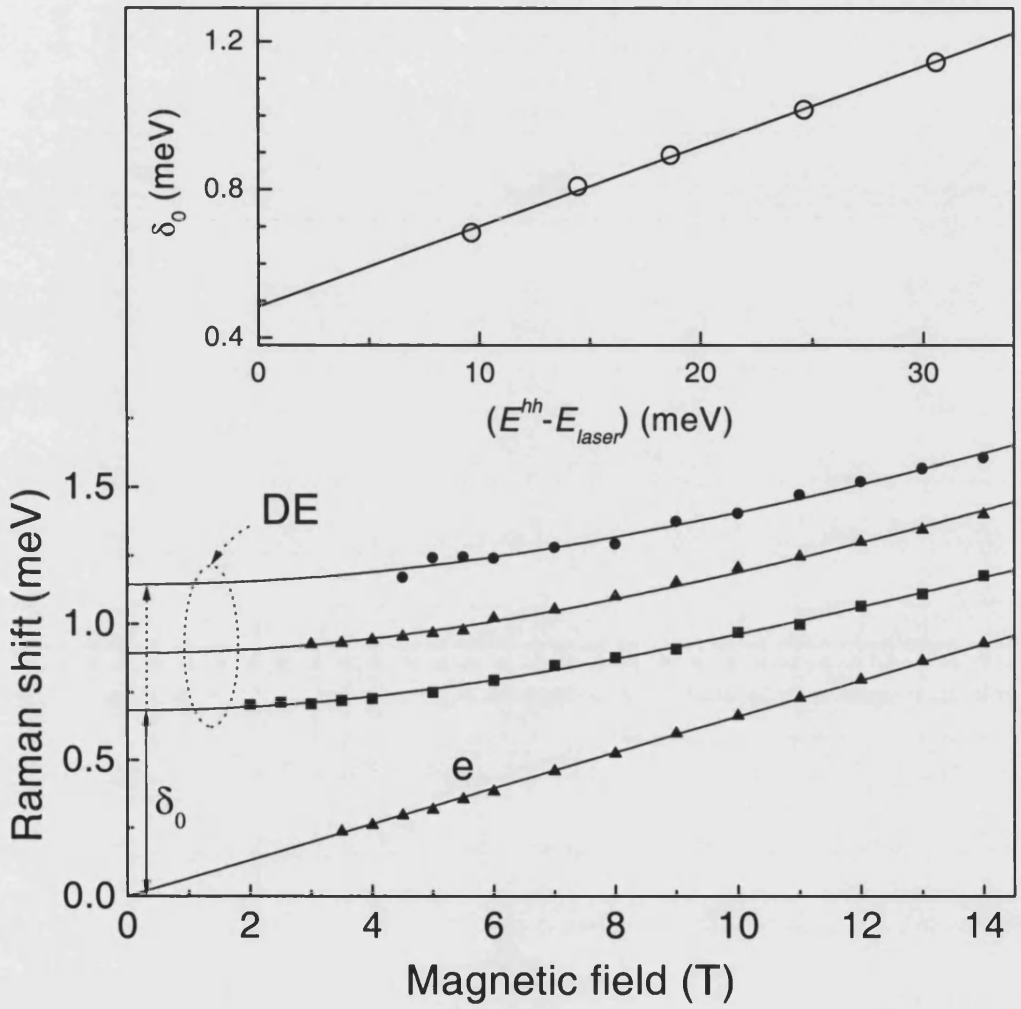

Figure 4.12: Sample B1485: Experimental Stokes Raman shift dependence on the magnetic field and excitation energy E_{laser} for the DE and e lines; 2.7338 eV - squares, 2.7248 eV - triangles, 2.7129 eV - circles. The solid lines are fits to the experimental data of a linear form (line e; Eq. 1.1) and $\sqrt{\delta_0^2 + (g_e^{\perp}\mu_B B)^2}$ (DE line). The inset shows the linear increase the zero-field electron-hole exchange splitting δ_0 on exciton localization energy.

relative motion of the electron and hole in the exciton. For a quasi-2D system the wave function of the exciton can be presented as the product of the wave function of the in-plane motion $\psi_{in-pl}(r)$ and the wave function of transverse motion within quantum well $\phi_q(z)$. For an exciton trapped by a fluctuation well the wave function of the in-plane motion is defined by the radius of the localized state

$$a_{loc} = \left[\frac{\hbar^2}{2\mu E_{loc}}\right]^{1/2}, \tag{4.11}$$

where E_{loc} is the localization energy and μ is the exciton reduced mass and, therefore,

$$|\psi_{in-pl}(0)|^2 \sim a_{loc}^{-2} = \frac{2\mu E_{loc}}{\hbar^2} \tag{4.12}$$

The transverse motion in quantum well is restricted by the quantum well width L_z and estimation of the $\phi_q(0)$ is

$$|\phi_q(0)|^2 \sim L_z^{-1} \tag{4.13}$$

Substituting Eqs. 4.11 and 4.13 into Eq. 4.10 we obtain for the A-N splitting of the localized exciton in a quantum well an expression for its linear dependence on E_{loc}

$$\delta_0 \sim v_0 L_z^{-1} \frac{2\mu E_{loc}}{\hbar^2} \delta_0^{at} \tag{4.14}$$

We note that the dependence of the zero-field (A-N) electron-hole exchange splitting on the quantum well width was observed experimentally (Zeeman spectroscopy) in Refs. [125, 126] on high quality GaAs/AlGaAs QWs - it is of the form L_z^{-1}.

Another speculation is based on the results of variational calculations of the dependence of the excitonic short-range electron-hole exchange interaction for the wide range of quantum well widths in GaAs-based QWs. Such results can be found, for example in Ref. [127]. The enhancement of the exchange interaction F_{exp} compared to bulk well material from the changes of electron-hole overlap in quantum-confined excitons was taken as

$$F_{exp} = \frac{\mid \phi_{QW}(0) \mid^2}{\mid \phi_{bulk}(0) \mid^2} \int_{-\infty}^{\infty} \mid \Psi_e(z)\Psi_h(z) \mid^2 dz, \tag{4.15}$$

where $\Psi_e(z)$ and $\Psi_h(z)$ are the z components of the electron and hole wave functions, which are obtained from solution of the separated Schrëdinger equation under appropriate boundary conditions. It was found that the exchange

enhancement firstly, increases with decreasing quantum well width (as expected; $\sim L_z^{-1}$), secondly tends to saturate at a certain width and thirdly, decreases for the very narrow QWs. The second and the third steps are more clearly seen for the QWs with smaller barrier heights and are due to the relative increase of the spread of the wave functions into the barrier material when the confinement energy increases. This behaviour is similar to the behaviour of the exciton binding energy on the quantum well width (see Fig. 2.10). Very recently, similar variational calculations were applied to the CdSe/ZnSe system of self-assembled quantum dots (CdSe half-sphere on a two-ML wetting layer embedded in ZnSe) [128]. The saturation and the declining parts of the short-range electron-hole exchange interaction dependence on the quantum dot radius have also been found. In both cases (QWs and QDs), in a "rough view" the declining part is linear. Thus, in principal, the dependence shown on the Inset to Fig. 4.12 may, represent the declining part of the exchange interaction. This is consistent with localizing exciton sites in the submonolayer structures being flat quantum islands of fluctuating Cd content and size (lateral size and thickness). As we already said above more experimental and theoretical studies are needed to provide a conclusion. For the calculations the effects of strain and alloying as well as delocalization of the hole wave function in a very narrow(small) QWs(QDs) should be taken into account[128]. Unfortunately, the investigated "ordinary" ZnCdSe/ZnSe QWs do not exhibit wide enough resonance profiles for the DE line - all the variation of the A-N splitting with E_{laser} was found to be just slightly above experimental error.

Microscopic spin – flip mechanisms responsible for the observed signals. The properties of the e line allows one to associate it with the SFR scattering that was described in Chapter 1 and Chapter 3.

The DE and 1-5 lines one also assigns to a SFR scattering process. This assignment is based on the results of earlier works on resonant SFR scattering in different semiconductor QW and QD systems of Refs. [12, 13, 14, 16, 105]. Those measurements revealed, contrary to our work, only one SFR line, which is related to a transition within a bright part of a heavy hole exciton. Nevertheless one believes that the same microscopic scattering mechanism as discussed in these work plays a role in our case. Namely, the SFR lines can be explained as involving acoustic-phonon Raman scattering when the interaction Hamiltonian for transitions between the electron states with different spins is taken into account. The

spin-acoustic-phonon interaction was considered, for example in Ref. [129] and more recently in Ref. [130][4]. This interaction causes spin-flip, which can described in the following simple way: an acoustic phonon (wave) makes distortions of the lattice, which perturbs (mixes) the wave functions of the valence and conduction states (it is similar to the spin-lattice relaxation). In principle both the deformation potential and piezoelectric interaction can be considered [12, 131], although their relative strength should be discussed when considering the case of localized excitons. Thus, for an electron there is some probability to be scattered from one Zeeman state to another with phonon emission/absorption. The SFR scattering mechanism then includes three virtual transitions: 1 - a heavy hole exciton ground state $|+1>$ or $|-1>$ is excited by absorption of the σ^+ or σ^- polarized light, respectively; 2 - an inversion of both electron and hole spins in the exciton takes place via the interaction with acoustic phonons (emission or absorption); 3 - the exciton recombines with emission of a scattered photon of the opposite polarization. The described process corresponds to the flip of the angular momentum of the bright exciton. The spin-flip of just one particle within the exciton (commonly attributed to the hole) leads to the transformation of a bright exciton to a dark one (this is why the line, observed in the Voigt geometry in our very first experiments, has the label DE - dark exciton). The emission or absorption of an acoustic phonon is allowed in our case because of the exciton localization leads to the relaxation of the **k**-vector conservation condition. Thus because of this fact and because of the broad energetic distribution of the exciton localizing sites due to fluctuations in their size as well as Cd content, the observed SFR lines manifest as a result of doubly resonant (incoming and outgoing photons are both in resonance with two real intermediate states), acoustic-mediated spin-flip scattering. The continuous dependence of the SFR scattering shift on the magnetic field strength is explained by the assumption of the bulk-like acoustic phonon involvement - the phonon continuum always provides phonons to fit the Zeeman splitting in a doubly resonant scattering process; this can not be directly achieved with the fully confined phonons.

An important note should be made at this point. The line width of the exciting laser when expressed in meV is $\sim$ 0.04 meV, that is much smaller than the splitting between the levels of the exciton fine structure (up to 3 meV at $B = 14$ T - the strongest magnetic field used in the experiments; see Fig. 4.10). This fact

[4]In Ref. [130] a new mechanism of spin-flip in GaAs in the presence of an external magnetic field is proposed. Namely, the strain produced by the emitted phonon is coupled directly to the electron spin through the variation of the effective g-factor.

allows to obtain a very good resonance condition with one or another excitonic level belonging to a particular localizing site. Nevertheless, the excitation exactly in resonance with one of the levels can be still in a good resonance condition with other levels localized at the same site or with the "energetically" close levels of different sites. The first leads to that one observes in the spectra under $z(\sigma^+,\sigma^-)\bar{z}$ polarization not only, let say the 2 and 4 lines but also the 1 and 3 lines (see Fig. 4.10) originating from the same site. The latter leads to an uncertainty in the site selectivity of the (resonant) excitation. From the analysis of the Raman shift of the Stokes and anti-Stokes components of the lines measured at a certain magnetic field strength and at the same excitation energy[5] as well as their line shape (well fitted by Lorentzians) we conclude that this uncertainty is relatively small and being "inside" the error of the g-factors and δ_0 determination at any E_{loc}. Also an uncertainty in the site selectivity appears when the magnetic field changes. In this case the constant exciting laser energy "passes" resonantly the levels (of the same nature) of the different sites. This uncertainty is easy to estimate from the value of the relative magnetic field dependent shift of a level of the exciton fine structure. The estimated value is less than 1 meV, being smaller than size of the circles representing the experimental data in the inset to Fig. 4.10.

Finally, we mention a mechanism of exciton-spin-relaxation (at $B = 0$ T) due to the long-range part of the electron-hole exchange interaction in an exciton. For free excitons, this interaction acts as an effective magnetic field coupling the bright exciton spin states (in this sense it is similar to the well known Dyakonov-Perel mechanism for free carriers [131]). The concept of this mechanism was elaborated theoretically by Maialle, de Andrada e Silva and Sham [111]. Several experimental works showed that this mechanism does play an important role in changing the heavy-hole exciton spin from a $|+1>$ into $|-1>$ (or vice versa) state in intrinsic quantum wells under a resonant excitation (see for example Ref. [132]). Nevertheless, it was also experimentally showed that at low temperatures excitonic localization strongly affects this mechanism, resulting in a reduced exciton spin-flip rate (see for example Ref. [133]). To decide whether this mechanism should also be taken into consideration in our case further theoretical

[5]This case corresponds to the perfect resonance condition for both sites when, for example the bottom level of one site "crosses" the top level of the other site; or if to use the language of the totally pure states, the level of the $|-2>$ state crosses the level of the $|+1>$ one. One should remember here that in a magnetic field with a nonzero cross component ($B_x \neq 0$) the bright and dark excitonic states are mixed, so that the otherwise forbidden states $|\pm 2>$ can be excited by light.

and experimental studies are needed.

4.5 Outlook

Finishing this Chapter we would like to mention briefly at least three topics related to the behaviour of localized excitons. These topics were left out of consideration in this work, but which can be discussed later on the basis of the available experimental data.

The first topic concerns a modelling of the magnetic field dependence of the SFR intensities of the observed lines related to the excitonic transitions as well as the relative intensities of these lines at a constant magnetic field.

The second topic is related to the analysis of the spectral width of the observed lines, its dependence on E_{loc}. Particularly, we found that in a constant magnetic field the line 1 (observed in the Faraday geometry) becomes slightly narrower with increasing E_{loc}, whereas the line DE (observed in the Faraday geometry) demonstrates the opposite behaviour.

The modelling of the temperature dependence of the intensities of observed lines is the third topic. Fig. 4.13 presents the results of the measurements of such a dependence for the line 1-4 (the measurements were carried out at a very low excitation power). For all the lines the dependence corresponds to that of a temperature-activated process. For example, for the line 1 we found that the activation process occurs at about $T = 15$ K and a characteristic activation energy ε is about 7 meV. This value, being close to the value of the PL Stokes shift of about 8 meV, was obtained by fitting the experimental data at high temperatures by the expression $\ln(I(T)/I(4.5K) = \varepsilon/kT$. For the other lines the activation process starts at lower temperatures. To model these T-dependences is a complicated task but may be possible by considering the appropriate rate equations, which describe generation, recombination, thermal delocalization of excitons and spin transitions between the quartet levels.

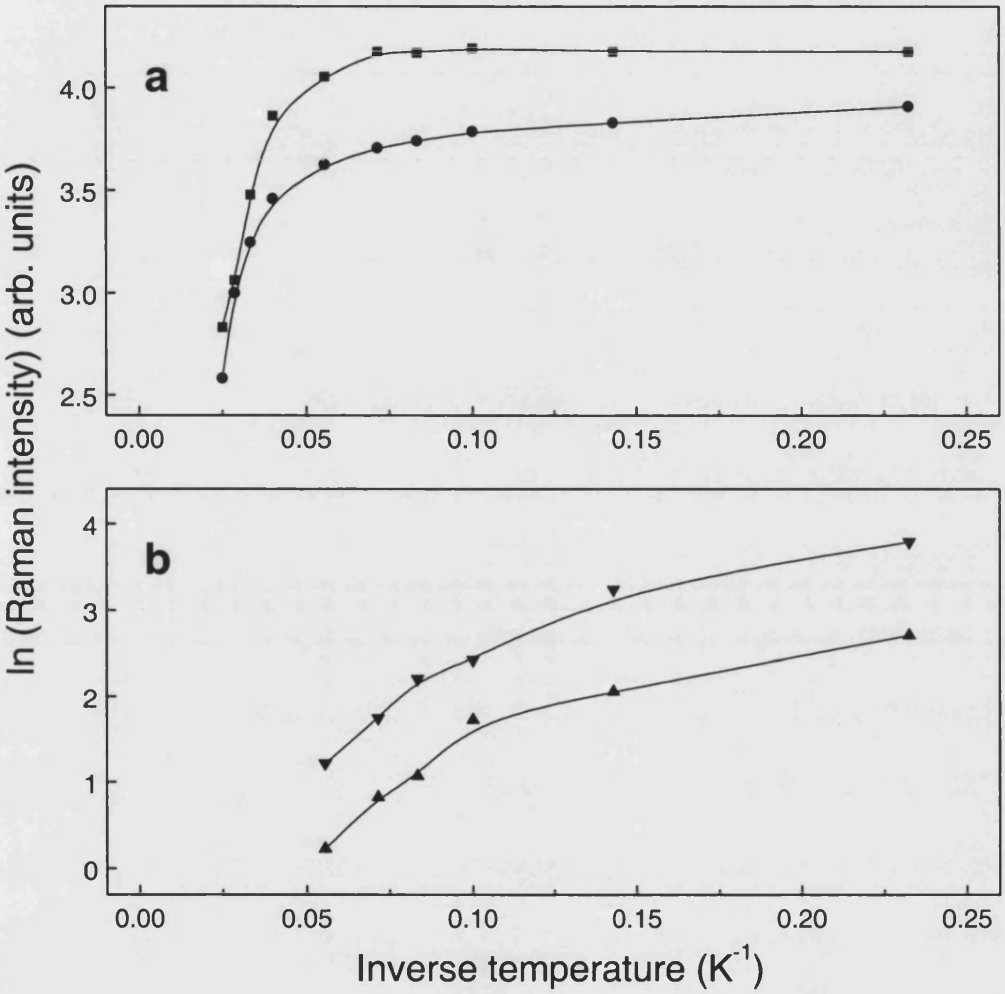

Figure 4.13: Sample S0601: Temperature dependence of the integrated intensities for the Stokes parts of the line (a) 1 and 2, (b) 3 and 4. $\theta = 30°$, $B = 14$ T, $E_{laser} = 2.7619$ eV.

Chapter 5

Overall conclusion

In this chapter, as a conclusion to the whole thesis, the results of the application of SFR spectroscopy to ZnCdSe-based heterostructures presented and discussed in Chapter 3 and Chapter 4 are given in a condensed form.

To Chapter 3:

Bulk epitaxial layers of ZnCdSe of different Cd content have been studied. This study also included epitaxial layers of the end-members of this alloy - CdSe and ZnSe. All the layers were of the single-phase cubic modification.

For all the substances it was found that: (a) the excitation in resonance with the shallow donor-bound exciton PL transition in the presence of a magnetic field produces strong Stokes and anti-Stokes Raman signals associated with transitions between the spin states of the donor-bound electron; (b) the Raman shift of the signals is linearly proportional to the magnetic field; (c) the Raman shift of the signals does not depend within experimental error on the spectral position of the excitation when it changes across the donor-bound exciton PL band.

As a result of these findings the dependence of the electron g-factor over the whole range of Cd content has been determined for the first time. The value of the g-factor gradually decreases with increasing Cd content but does not change sign. For the particular case of CdSe, the g-factor was measured to be $+0.42 \pm 0.01$.

Calculations based on five-band $\mathbf{k}\cdot\mathbf{p}$ perturbation theory, along with the method of determining the squared interband matrix elements developed by Hermann and Weisbuch were successfully used to reproduce the experimental dependence of the g-factor on Cd content, which can be approximated well by $g(x) = 1.16 - 0.56x - 0.18x^2$. The values of the squared interband matrix elements found from these calculations for cubic CdSe are $P^2 = 18.3$ eV and $P'^2 = 4.9$ eV.

The SFR study was accompanied by the study of photoluminescence, reflectance and phonon Raman scattering. This allowed us to measure some parameters of excitons which are not well known at present for the cubic modification of CdSe: the transition energy for free excitons and the transition energy and the diamagnetic coefficient for neutral shallow donor-bound excitons. The dependence of the LO-phonon energy of ZnCdSe on Cd content was also found.

To Chapter 4:

ZnCdSe/Zn(S)Se quantum wells of thickness 35-55 Å and Cd content 12-25 percent and submonolayer CdSe/ZnSe quantum wells have been studied.

For all the structures qualitatively similar SFR spectra were measured. Depending on the magnetic field orientation up to five spectral signals are observed under excitation within the inhomogeneously broadened photoluminescence of excitons localized in QWs by potential fluctuations. The analysis of the data obtained under different experimental conditions and the use of a model Hamiltonian describing the fine structure of the heavy hole exciton ground state in a magnetic field allowed us to establish that the signals correspond to the transitions between different levels of excitonic fine structure. Such transitions are determined by spin-flip transitions of the electron and/or hole in an exciton and lead to a flip of the exciton angular momentum. The Raman scattering process can be discussed then in terms of a doubly resonance mediated by acoustic phonons.

The analysis of the experimental data also allowed us to determine the g-factors of the excitonic electron and hole and the value of the zero field electron-hole exchange splitting. The values of the g-factors are close to that of bulk ZnSe in all the studied structures whereas the exchange splitting is enhanced and is typically of order 0.5-1.2 meV.

The structure of a 0.5 monolayer CdSe/ZnSe showed the widest intensity resonance profile for the observed excitonic signals amongst all the structures. This allowed the study of the dependence of the electron g-factor and exchange splitting on exciton localization energy. A slight increase of the g-factor was found. The exchange interaction increases linearly with the localization energy and changes by a factor of two when the localization energy changes from 10 to 30 meV.

In the SFR spectra the signals due to spin-flip of electrons bound at donors or localized by potential fluctuations in a quantum well were also identified. The corresponding g-factor does not depend within experimental error on the spectral position of the excitation within the the photoluminescence band, being very closed to the bulk ZnSe value, but changes slightly towards lower values for the wider quantum wells.

Appendix A

Parameters of ZnSe and CdSe

	ZnSe (cubic)	CdSe (cubic)
a_0, Å	5.6676^{exp}	6.077^{exp}
E_0, eV	2.821^{exp}	1.764^{calc}
m_e/m_0	0.16^{exp}	$0.13^{exp,hex}$
m_{hh}/m_0	0.6^{exp}	$0.45^{exp,hex}$
m_{lh}/m_0	0.15^{exp}	0.145^{calc}
E_Γ^{LO}, meV	31.7^{exp}	26.5^{exp}
a_{hy}, eV	-4.7^{exp}	-2.6^{calc}
b_{sh}, eV	-1.2^{exp}	-0.8^{calc}
C_{11}, 10^{10} N/m^2	8.26^{exp}	6.67^{calc}
C_{12}, 10^{10} N/m^2	4.98^{exp}	4.63^{calc}
r_B, Å	33.0^{calc}	43.4^{calc}
E_x, meV	19^{exp}	$15^{exp,hex}$

These parameters are met throughout the thesis and their shown values are the most frequently used in the literature. These values are empirical (exp) or calculated (calc) and related to low-temperatures; (hex) labels values of the hexagonal modification. Some other parameters are collected in Table 3.1, p. 59.

Appendix B

The electron g-factor

The g-factor is a coefficient in the formula for splitting of spin degenerate energy levels ΔE in an external magnetic field B (Zeeman effect)[1]. It determines the scale of the splitting in units of the Bohr magneton (see Eq. 1.1).

The g-factor was first introduced by A. Landé in 1921, who showed that for different states of an electron in an atom the value of g is given by the formula:

$$g = 1 + \frac{J(J+1) + S(S+1) - L(L+1)}{2J(J+1)}, \tag{B.1}$$

where J, S and L are quantum numbers representing respectively in units of $\hbar$ the total angular momentum of the atom, the electron spin and orbital angular momentum. The simplest case is that of a single electron whose orbital momentum $L = 0$ (free electron). The pure spin g-factor g_0 is then two.

The value $g_0 = 2$ is a good approximation for a free electron with small energy. For a free electron with relativistic energy $E = (m^2c^4 + c^2p^2)^{1/2}$ a correction to the energy splitting in Eq. 1.1 of order $1/c^2$ should be taken into account. Another correction of order $1/c$, arises from the interaction with the zero-point vibrations of the radiation field [134, 135]. It results in the "only-spin" value being:

$$g_s = (1 + \alpha/2\pi)g_0 \approx 2.00229, \tag{B.2}$$

[1]The g-factor is often called the gyromagnetic ratio because it also determines the ratio of the magnetic moment of a particle to its angular momentum.

where $\alpha = 1/137$ is the fine structure constant.

In atoms and in solids, the g-factor will differ from the value g_s as a result of spin-orbit interaction. It is appropriate to expect that in the solids the magnitude of the interaction is closely related to that in the free atom because it occurs well inside the ion core and the wave function in the solid is the same in this region, apart from normalization, as in the isolated atom.

In general, the spin-orbit interaction is the interaction of a spin momentum with the magnetic field that it sees, as a result of the relative motion of the other charges. Thus in an atom, an electric field in the frame of the nucleus will result in a magnetic field in the frame of electron moving around. The Hamiltonian for the atom including these interactions can be written as [136]

$$\begin{aligned} H &= \sum_i \frac{p_i^2}{2m} - \sum_i \frac{Ze^2}{r_i} + \sum_i \sum_j \frac{e^2}{r_{ij}} + \sum_i \frac{\hbar}{4m^2c^2} \frac{Ze^2}{r_i^3} \mathbf{r}_i \times \mathbf{p}_i \cdot \sigma_i \\ &+ \sum_i \sum_j \frac{e^2\hbar}{2m^2c^2} \frac{\mathbf{r}_{ij}}{r_{ij}^3} \times (\mathbf{p}_i - \mathbf{p}_j) \cdot \sigma_i + \sum_i \sum_j \frac{e^2\hbar}{4m^2c^2} \frac{\mathbf{r}_{ij}}{r_{ij}^3} \times \mathbf{p}_i \cdot \sigma_i \end{aligned} \quad \text{(B.3)}$$

where Z is the atomic number and the indices i and j refer to the electrons; $\mathbf{r}_i$ is measured from the nucleus; $\mathbf{r}_{ij} = \mathbf{r}_i - \mathbf{r}_j$; the components of σ are the Pauli spin matrices:

$$\sigma_x = \begin{pmatrix} 0 & 1 \\ 1 & 0 \end{pmatrix}; \quad \sigma_y = \begin{pmatrix} 0 & -i \\ i & 0 \end{pmatrix}; \quad \sigma_z = \begin{pmatrix} 1 & 0 \\ 0 & -1 \end{pmatrix} \quad \text{(B.4)}$$

In Eq. B.3 the first three terms include the kinetic and Coulomb energies; the fourth term is the spin-orbit interaction with the nucleus; the fifth term is the sum of the electron-electron spin-orbit interactions, also known as the spin-other orbit interactions. Each term is expressed in the rest frame of the electron whose spin appears in that term. The last term is the Thomas precession which results on transforming back to the rest frame of the atom.

The g-factor of conduction electrons in crystals is determined mostly by the spin-orbit interaction of the valence electrons and of the closed shell lying just below these valence states. Usually the spin-other orbit terms are ignored, and each electron then has a spin-orbit energy given by [136]

$$H_{so} = \frac{\hbar}{4m^2c^2} \nabla V(\mathbf{r}) \times \mathbf{p} \cdot \sigma, \quad \text{(B.5)}$$

where $V(\mathbf{r})$ is an effective potential arising from the nucleus and the remaining electrons; it has the symmetry of the space group of the crystal[2].

To obtain the energy levels of conduction electrons in a magnetic field and thus to determine the g "shift" caused by the spin-orbit interaction one has to consider the Hamiltonian defined by:

$$H = \frac{1}{2m}\left(\mathbf{p} + \frac{e\mathbf{A}}{c}\right)^2 + V + \frac{\hbar}{4m^2c^2}\sigma \cdot \nabla V \times \left(\mathbf{p} + \frac{e\mathbf{A}}{c}\right) + \frac{1}{2}g_s\mu_B\mathbf{H}\cdot\sigma, \quad \text{(B.6)}$$

where $\mathbf{H} = \nabla \times \mathbf{A}$ is the magnetic field vector and $\mathbf{A}$ is the vector-potential. The last term in this equation represents, of course the Zeeman contribution.

The effect of the magnetic field on Bloch functions is not small because they extend throughout the crystal. It makes the task very complicated - the energy levels cannot be obtained by using perturbation theory. The idea to handle this problem came first from Luttinger and Kohn [138], who recognized that if the electrons occupy only small portions of the conduction band such that the extent in $\mathbf{k}$-space of the occupied region is small compared to a reciprocal lattice vector, a perturbation treatment in powers of the wave vector can be used to obtain an approximation to the Hamiltonian. To the first order, this is the effective mass Hamiltonian. To obtain g-factors this approach was used first by Luttinger [139], Yafet [140], Cohen and Blount [141].

The treatment of Luttinger and Kohn is based on the introduction of the functions $\chi_{\mathbf{k}}(\mathbf{r}) = \exp(i\mathbf{k}\cdot\mathbf{r})\psi_{\mathbf{k_0}}(\mathbf{r})$ as a basis for a representation. Here $\mathbf{k_0}$ is the location of the energy minimum of the band of interest; the $\psi_{\mathbf{k_0}}$ are the Bloch functions of the Hamiltonian at zero magnetic field and at $\mathbf{k_0}$; $\mathbf{k}$ is measured from $\mathbf{k_0}$. The essential point is that $\chi_{\mathbf{k}}(\mathbf{r})$ depends on $\mathbf{k}$ only through $\exp(i\mathbf{k}\cdot\mathbf{r})$. As a result the effective mass Hamiltonian can be written in a form consisting of two terms. The first term is the usual effective mass result implying a free-electron like orbital motion from cell to cell [138]. The second term shows that an electron carries with it an effective magnetic moment μ^* in this free-electron like motion, partly from the spin μ_s and partly from "unquenched" orbital motion μ_l within

[2]In some cases the spin polarization of the nuclei causes the Overhauser shift of the conduction electron spin resonance frequency which results in nonegligible changes of the effective g-factor [137].

a unit cell [141]:

$$\mu^* = \mu_l + \mu_s = -\mu_B \left(\mathbf{L} + \frac{1}{2} g_s \sigma \right), \tag{B.7}$$

where $\mathbf{L}$ has the nature of orbital angular momentum.

The "spin" Hamiltonian corresponding to μ^*, takes the form [141]:

$$< n|\mu^*|n > \cdot \mathbf{H} = \frac{1}{2} \mu_B \sum_{ij} H \lambda_i G_{ij} \sigma_j, \tag{B.8}$$

where λ_i are the direction cosines of $\mathbf{H}$ relative to the axes x, y, z. The matrix (B.8) is

$$\frac{1}{2} \mu_B H \begin{pmatrix} \sum \lambda_i G_{iz} & \sum (\lambda_i G_{ix} - i \lambda G_{iy}) \\ \sum \lambda_i G_{ix} + i \lambda_i G_{iy} & -\sum \lambda_i G_{iz} \end{pmatrix} \tag{B.9}$$

Its eigenvalues are $\pm 1/2 g \mu_B H$, where the effective g-factor is defined as

$$g = \left[\sum_{ijl} \lambda_i \lambda_j G_{il} G_{jl} \right]^{1/2} \tag{B.10}$$

The quantity

$$Q_{ij} = \sum_{l} G_{il} G_{jl} \tag{B.11}$$

is a symmetric second-rank tensor and can be diagonalized. Designating the principal components of Q_{ij} as g_1^2, g_2^2 and g_3^2 and letting λ_i' now be the direction cosines of $\mathbf{H}$ relative to the principal axes of Q_{ij} one gets:

$$g = \left[(\lambda_1')^2 g_1^2 + (\lambda_2')^2 g_2^2 + (\lambda_3')^2 g_3^2 \right]^{1/2} \tag{B.12}$$

Appendix C

The $\mathbf{k} \cdot \mathbf{p}$ method

The $\mathbf{k} \cdot \mathbf{p}$ method is a tool for accurate calculations of the band energy dispersion and wave functions at and near the high-symmetry points in $\mathbf{k}$ space with the aid of perturbation theory. It is a semi-empirical technique in the sense, that to obtain quantitative results, experimental values of such parameters as energy gaps, effective masses, g-factors and oscillator strengths of the optical transitions in the vicinity of the band-edges have to be used as input parameters. Often some of the inputs are determined with the best accuracy in optical experiments. Therefore, the $\mathbf{k} \cdot \mathbf{p}$ method is particularly convenient for interpreting optical spectra.

The basic idea of the method is to consider the $\mathbf{k}$-dependent terms in the Schrödinger equation for a crystal as a perturbation.

Consider now basics of the stationary (time independent) perturbation theory. In this case the Hamiltonian of a quantum mechanical system is considered as

$$H = H_0 + H', \tag{C.1}$$

where H_0 is a Hamiltonian for the unperturbed system and for which the solution of the Schrödinger equation is known, H' is a Hamiltonian representing a weak perturbation for the system. The solution of the equation

$$H\psi = E\psi \tag{C.2}$$

for the full Hamiltonian H can be represented in terms of the eigenfunctions and eigenvalues of the known Hamiltonian H_0 and parameter λ:

$$\psi = \psi_0 + \lambda\psi_1 + \lambda^2\psi_2 + \lambda^3\psi_3 + \cdots, \tag{C.3}$$

$$E = E_0 + \lambda E_1 + \lambda^2 E_2 + \lambda^3 E_3 + \cdots, \tag{C.4}$$

where ψ_0, ψ_1, $\cdots$ and E_0, E_1, $\cdots$ are the various orders of corrections due to the perturbation H'. In general, the zero order state ψ_0 could be either nondegenerate or degenerate and the perturbation approach is different for the two cases. The detailed procedure allowing one to determine the different order corrections can be found in textbooks on Quantum Mechanics; see for example [142].

In the nondegenerate case the perturbation approach gives for the first order corrections to a state ψ_0 (or $|m>$ in Dirac notation)

$$\psi_1 = \sum_n a_n^{(1)} |n>, \tag{C.5}$$

where the coefficients:

$$a_k^{(1)} = \frac{<k|H'|m>}{E_m - E_n}, \quad k \neq m \tag{C.6}$$

The correction to the energy, which is the expectation value of H' for the unperturbed state $|m>$, is given by

$$E_1 = <m|H'|m> \tag{C.7}$$

In second order the perturbation approach gives for the wavefunctions:

$$\psi_2 = \sum_{n \neq m} a_n^{(2)} |n>, \tag{C.8}$$

where

$$a_k^{(2)} = \sum_{n \neq m} \frac{<k|H'|n><n|H'|m>}{(E_m - E_k)(E_m - E_n)} - \frac{<k|H'|m><m|H'|m>}{(E_m - E_k)^2}, \tag{C.9}$$

and for the energy:

$$E_2 = \sum_{n \neq m} \frac{|<m|H'|n>|^2}{E_m - E_n} \tag{C.10}$$

The full second order corrections for the unperturbed state $|m>$ therefore are

$$\psi = u_m + \sum_{k\neq m} u_k \left(\frac{<k|H'|m>}{E_m - E_k} - \frac{<k|H'|m><m|H'|m>}{(E_m - E_k)^2} \right) + \sum_{k\neq m}\sum_{n\neq m} u_k \frac{<k|H'|n><n|H'|m>}{(E_m - E_k)(E_m - E_n)}, \tag{C.11}$$

$$E = E_m + <m|H'|m> + \sum_n \frac{|<m|H'|n>|^2}{E_m - E_n} \tag{C.12}$$

In the degenerate case the states u_m and u_l have the same unperturbed energy. Then the coefficient given in Eq. C.6 causes difficulty due to the denominator being equal to zero, unless $<l|H'|m>=0$. If $<k|H'|m>\neq 0$ one assumes that H' breaks the degeneracy at some order of perturbation. The two nondegenerate states then can be presented as a certain linear combination of u_m and u_l:

$$\psi_0 = a_m u_m + a_l u_l \tag{C.13}$$

and for the energy:

$$E_0 = E_m = E_l \tag{C.14}$$

The first order correction is given by

$$E_1 = \frac{1}{2}(<m|H'|m> + <l|H'|l>) \pm \frac{1}{2}\left[(<m|H'|m> - <l|H'|l>)^2 + 4|<m|H'|l>|^2\right]^{1/2} \tag{C.15}$$

If the degeneracy of the states is not lifted in first order one must go to second order. The second order correction is given by the eigenvalue equations:

$$\begin{aligned} \left(\sum_{n\neq m} \frac{|<m|H'|n>|^2}{E_m - E_n} - E_2 \right) a_m + \sum_{n\neq m} \frac{<m|H'|n><n|H'|l>}{E_m - E_n} a_l &= 0 \\ \sum_{n\neq m} \frac{<l|H'|n><n|H'|m>}{E_m - E_n} a_m + \left(\sum_{n\neq m} \frac{|<l|H'|n>|^2}{E_m - E_n} - E_2 \right) a_l &= 0 \end{aligned} \tag{C.16}$$

A necessary and sufficient condition that degeneracy is removed in any given order is when the diagonal elements of H' in the two degenerate states are unequal or when the H diagonal matrix element is nonzero [143].

Consider now the Schrödinger equation for an electron in a ideally periodic crys-

tal, neglecting for simplicity the spin-orbit coupling:

$$H\Psi(\mathbf{r}) = \left(\frac{p^2}{2m} + V(\mathbf{r})\right)\Psi(\mathbf{r}) = E\Psi(\mathbf{r}), \tag{C.17}$$

where p represents the electron momentum, m its mass. The potential $V(\mathbf{r})$ in which the electron moves is periodic in it dependence on position $\mathbf{r}$, with the periodicity of the crystal lattice. According to the Bloch theorem the solutions of Eq. C.17 are Bloch functions:

$$\Psi(\mathbf{r}) = \exp^{i\mathbf{kr}} u_{\mathbf{k}}(\mathbf{r}), \tag{C.18}$$

where $\mathbf{k}$ is a wavevector in the first Brillouin zone, $u_{\mathbf{k}}(\mathbf{r})$ is required to have the crystal lattice periodicity; it is the so called central cell function. A substitution (C.18) into (C.17) gives an equation in $u_{\mathbf{k}}(\mathbf{r})$ of the form

$$\left(\frac{p^2}{2m} + \frac{\hbar}{m}\mathbf{k}\cdot\mathbf{p} + \frac{\hbar^2 k^2}{2m} + V(\mathbf{r})\right) u_{n\mathbf{k}}(\mathbf{r}) = E_n(\mathbf{k}) u_{n\mathbf{k}}(\mathbf{r}), \tag{C.19}$$

where $n = 1, 2, 3...$ is used to index different energy bands. For any given $\mathbf{k}$, the set of all $u_{n\mathbf{k}}(\mathbf{r})$ is a complete and orthonormal set of functions having the periodicity of $V(\mathbf{r})$. Hence if we choose $\mathbf{k} = \mathbf{k_0}$, the wavefunction for any $\mathbf{k}$ may be expressed in terms of the wave function for $\mathbf{k_0}$,

$$u_{n\mathbf{k}}(\mathbf{r}) = \sum_{n'} c_{n'n}(\mathbf{k} - \mathbf{k_0}) u_{n'\mathbf{k_0}}(\mathbf{r}), \tag{C.20}$$

where $c_{n'n}$ are the expansion coefficients that are to be determined by the standard eigenvalue solution method [143]. Defining for a particular $\mathbf{k} = \mathbf{k_0}$

$$H_{\mathbf{k_0}} = \frac{p^2}{2m} + \frac{\hbar}{m}\mathbf{k_0}\cdot\mathbf{p} + \frac{\hbar^2 k_0^2}{2m} + V(\mathbf{r}) \tag{C.21}$$

$$H_{\mathbf{k_0}} u_{n\mathbf{k_0}}(\mathbf{r}) = E_n(\mathbf{k_0}) u_{n\mathbf{k_0}}(\mathbf{r}) \tag{C.22}$$

and remembering that $\mathbf{p} = -i\hbar\nabla$ we obtain

$$\left[H_{\mathbf{k_0}} + \frac{\hbar}{m}(\mathbf{k} - \mathbf{k_0})\cdot\mathbf{p} + \frac{\hbar^2}{2m}\left(k^2 - k_0^2\right)\right] u_{n\mathbf{k}} = E_n(\mathbf{k}) u_{n\mathbf{k}}(\mathbf{r}) \tag{C.23}$$

The $\mathbf{k}\cdot\mathbf{p}$ proportional term in this equation, as well as the usually very small term in k^2, can now be treated by stationary perturbation theory as a perturbation of the normal crystal Hamiltonian.

In the case of a nondegenerate band with the extremum at the Γ-point of the Brillouin zone ($\mathbf{k_0} = 0$) one obtains for the first order perturbation correction to the wavefunctions $u_{n\mathbf{k}}$ and energy $E_n(\mathbf{k})$ respectively:

$$u_{n\mathbf{k}} = u_{n0} + \frac{\hbar}{m} \sum_{n' \neq n} \frac{< u_{n0}|\mathbf{k} \cdot \mathbf{p}|u_{n'0} >}{E_n(0) - E_{n'}(0)} u_{n0} \tag{C.24}$$

$$E_n(\mathbf{k}) = E_n(0) + \frac{\hbar}{m} < u_{n0}|\mathbf{k} \cdot \mathbf{p}|u_{n0} > \tag{C.25}$$

For crystals without inversion symmetry, the functions u_{n0} may not have a well-defined parity, leading to a small correction to energy proportional to $\mathbf{k}$. It causes a small band warping. There is also a correction to the central cell part of the Bloch function proportional to the momentum matrix element. It leads, for example to a mixture of the p-type valence band states to the s-type states of the conduction band as one moves away from the conduction band zone centre.

To the second order, the energy becomes

$$E_n(\mathbf{k}) = E_n(0) + \frac{\hbar^2 k^2}{2m} + \frac{\hbar^2}{m^2} \sum_{n' \neq n} \frac{| < u_{n0}|\mathbf{k} \cdot \mathbf{p}|u_{n'0} > |^2}{E_n(0) - E_{n'}(0)} \tag{C.26}$$

This equation can be rewritten in terms of an effective mass m

$$E_n(\mathbf{k}) = E_n(0) + \frac{\hbar^2 k^2}{2m}, \tag{C.27}$$

where an expression for the effective mass is defined:

$$\frac{m_0}{m} = 1 + \frac{2}{m_0 k^2} \sum_{n' \neq n} \frac{| < u_{n0}|\mathbf{k} \cdot \mathbf{p}|u_{n'0} > |^2}{E_n(0) - E_{n'}(0)} \tag{C.28}$$

This formula particularly shows that the effective mass m is different from a free electron mass m_0 because of coupling between electronic states in different bands via the $\mathbf{k} \cdot \mathbf{p}$ term. Further more, one can see that band with energies less (higher) than E_n contribute a positive (negative) term to m_0/m making m of the nth-band smaller (larger) than the free electron mass.

Using the perturbation approach one has to carry out summations over all the bands. To reduce the number of bands taken into consideration Löwdin suggested so called decoupling method [144, 145] in which all the bands can be divided into two sets A and B. Bands in the set A interact strongly with one another but any

band in A interacts only weakly with any band in the set B. The interactions connecting bands in A with bands in B are then removed iteratively, while keeping all the matrix elements connecting bands in A. After this procedure the bands in A are left with "renormalized" interactions with one other. The matrix $(d \times d)$ representing the "renormalized" Hamiltonian from A must then be diagonalized exactly; d is the number of bands including spin degeneracy. As an example the Hamiltonian of the Γ_6 conduction band in the basis $|1/2, +1/2>$ (spin up) and $|1/2, -1/2>$ (spin down) and when all the interactions with the other bands are removed is represented by the matrix (2×2):

$$H^{\Gamma_6}(\mathbf{k}) = \begin{pmatrix} E_0 + \hbar^2 k^2/2m & 0 \\ 0 & E_0 + \hbar^2 k^2/2m \end{pmatrix}, \tag{C.29}$$

The Löwdin perturbation method in the framework of $\mathbf{k}\cdot\mathbf{p}$ approach will converge rapidly as long as

$$\frac{\hbar}{m}|(\mathbf{k} - \mathbf{k_0}) \cdot \mathbf{p}| \ll |E_n - E_{n'}|, \quad n \in A, \quad n' \in B \tag{C.30}$$

The bands for the set A are selected in order to satisfy Eq. C.30.

A three-band $\mathbf{k} \cdot \mathbf{p}$ approach, successfully used for narrow-gap semiconductors by Kane [145] and Pidgeon and Brown [146] does not give a good description of experimental results obtained on the medium-gap and wide-gap semiconductors. The reason is that in this case, the fundamental gap between Γ_6^c and Γ_8^v is about 1.5–3.5 meV, i.e., it is comparable, for example to the gap between the Γ_6^c and the upper Γ_7^c. Therefore, for most of the medium and wide-gap semiconductors it is appropriate as a starting point to include bands in the set A only if the separation between them is at least 3 eV.

Five-band $\mathbf{k}\cdot\mathbf{p}$ theory, fits with high precision the effective mass and the g-factor of most common medium and wide-gap semiconductor compounds and alloys. It includes into consideration the Γ_6^c, Γ_7^c, Γ_8^c, Γ_7^v, Γ_8^v bands (due to the degeneracies within each of the five bands the resulting Hamiltonian is represented by a matrix (14×14)). This approach has been used by Hermann and Weisbuch [93], Rössler [147], Cardona *et al.* [96] and Pikus [148]. One of the most complete treatments has been worked out by Pfeffer and Zawadzki [149], who described in great detail the conduction and valence bands of GaAs and InP. The modern development of the five-band $\mathbf{k} \cdot \mathbf{p}$ theory includes far-band contributions and polaron effects.

Appendix D

The exchange interaction

The exchange interaction is a specific mutual influence of identical particles (particles which posses the same physical properties: mass, charge, spin, quantum numbers). It manifests effectively as a result of a certain special interaction and is a quantum mechanical effect with no analogy in classic physics.

As a consequence of the quantum mechanical principle for identical particles, according to which these particles are indistinguishable, the wave function of a system has to possess a certain symmetry relative to a permutation of two of these particles, i.e. of their coordinates and their spin projections. For particles with integer spin (bosons) the system wave function is unchangeable under such permutations (symmetrical function). For particles with half-integer spin (fermions) - the system wave function changes its sign (antisymmetrical function). If the forces of the interaction between the particles do not depend on their spins, the system wave function can be written as a product of two wave functions. One of the wave functions depends only on coordinates of the particles and the second one depends only on their spins. In this case the coordinate part of the system wave function, which describes the movement of the particles in space, has to possess a certain symmetry relative to permutation of the coordinates, which also depends on the symmetry of the spin part. The existence of such a symmetry means that there is a certain correlation in the movement of the identical particles. This correlation influences the energy of the system even when there are not any interactions between the particles. Usually an interaction between the particles is considered as a result of a force interaction.

Therefore, the mutual influence of the identical particles can be considered as being due to specific, so-called "exchange forces". These forces determine the so called "exchange interaction".

The appearance of the exchange interaction can be illustrated by the example of a helium atom. The spin interactions in light atoms are small, therefore the wave function Ψ of the two electrons in the helium atom can be written as

$$\Psi = \Phi(\mathbf{r}_1, \mathbf{r}_2)\chi(\mathrm{s}_1, \mathrm{s}_2), \tag{D.1}$$

where $\Phi(\mathbf{r}_1, \mathbf{r}_2)$ is a function of coordinates $\mathbf{r}_1$, $\mathbf{r}_2$ and $\chi(\mathrm{s}_1, \mathrm{s}_2)$ is a function of their spin projections s_1, s_2 onto a certain direction. Since the electrons are fermions Ψ should be an antisymmetric functions. This means that if the total spin S of both electrons is equal to zero (spins are antiparallel), the function χ is an antisymmetric function relatively to a spin coordinate permutation. Therefore, the function Φ should be a symmetric function relatively to a space coordinate permutation. In the case when the total spin $S = 1$ (spins are parallel), χ is symmetric and Φ is antisymmetric. Let $\psi_n(\mathbf{r}_1)$ and $\psi_m(\mathbf{r}_2)$ be the wave functions of the electrons in the Helium atom; n and m index a set of quantum numbers, which determines an electronic state in the atom. Then, the coordinate part of Ψ for $S = 1$:

$$\Phi_a = \frac{1}{\sqrt{2}}\left[\psi_n(\mathbf{r}_1)\psi_m(\mathbf{r}_2) - \psi_m(\mathbf{r}_1)\psi_n(\mathbf{r}_2)\right] \tag{D.2}$$

and for $S = 0$:

$$\Phi_s = \frac{1}{\sqrt{2}}\left[\psi_n(\mathbf{r}_1)\psi_m(\mathbf{r}_2) + \psi_m(\mathbf{r}_1)\psi_n(\mathbf{r}_2)\right] \tag{D.3}$$

In the state with the antisymmetric wave function Φ_a the mean space between the electrons is larger then in the state with the symmetrical wave function Φ_s. It is seen that the probability $|\Psi|^2 = |\Phi_a|^2|\chi_s|^2$, which determines the existence of the electrons in the same space point $\mathbf{r}_1 = \mathbf{r}_2$ is zero for the state Φ_a. Thus the average energy of the Coulomb interaction (repulsion) of the two electrons is smaller in the state Φ_a, than in the state Φ_s. A correction to the energy of the system due to the electron interaction is determined by perturbation theory and is equal to

$$\Delta E = K \pm A, \tag{D.4}$$

where the signs $\pm$ relate to the symmetrical and antisymmetrical coordinate

states of the system, respectively and

$$K = e^2 \int \frac{|\psi_n(\mathbf{r}_1)|^2 |\psi_m(\mathbf{r}_2)|^2}{|\mathbf{r}_1 - \mathbf{r}_2|} d\tau_1 d\tau_2 \tag{D.5}$$

$$A = e^2 \int \frac{\psi_n^*(\mathbf{r}_1)\psi_m(\mathbf{r}_1)\psi_m^2(\mathbf{r}_2)\psi_n(\mathbf{r}_2)}{|\mathbf{r}_1 - \mathbf{r}_2|} d\tau_1 d\tau_2, \tag{D.6}$$

where $d\tau$ is a volume unit. The quantity K is called the Coulomb integral and has a classical physics meaning. It represents the electrostatic (Coulomb) interaction of two charged "clouds" with the charge densities $e|\psi_n(\mathbf{r}_1)|^2$ and $e|\psi_m(\mathbf{r}_2)|^2$. The quantity A, which is called the exchange integral, also can be interpreted as an electrostatic interaction of two charged "clouds" with the charge densities (exchange charges) $e\psi_n^*(\mathbf{r}_1)\psi_m(\mathbf{r}_1)$ and $e\psi_m^*(\mathbf{r}_2)\psi_n(\mathbf{r}_1)$ (the asterisk means complex conjugation), i.e. when each of the electrons exists simultaneously in either states ψ_n and ψ_m - which is impossible from the classical physics point of view. It follows from Eq. D.4 that the difference in the total energy of the helium atom with $S = 0$ and with $S = 1$ is $2A$. Thus, although the explicit spin interaction in this case is small and was neglected, the identity of two electrons in the helium atom leads to the dependence of the system energy on the total spin S as if it there exists an additional exchange interaction between the particles. Obviously, in this case the exchange interaction is a part of the Coulomb interaction of the electrons[1].

The exchange interaction effectively manifests itself in cases when the wave functions of the particles in the system overlap. This is seen from the expression for the exchange integral (D.6): if the degree of overlapping of the states $\psi_n^*(\mathbf{r})$ and $\psi_m(\mathbf{r})$ is negligible, then A is very small. The character of the exchange interaction is different for fermions and bosons. For the fermions the exchange interaction being a consequence of the Pauli exclusion principle results in repulsion of the electrons from each other at distances of an order or less than the electron de Broglie wave length. In a system of the identical bosons, the exchange interaction has a character of a mutual attraction of the particles.

If a system of identical particles is in an external field, for example in the Coulomb field of a nucleus, then the existence of a certain symmetry of the wave function and the corresponding correlation in movement of the particle will influence the

[1]This type of exchange is often called Heisenberg, direct exchange or potential exchange. However, there are additional types of important exchange mechanisms: indirect exchange, RKKY interaction exchange, exchange in the Kondo effect, itinerant exchange; see [150].

energy of the system in the field. This also is an exchange effect. Usually in an atom, in a molecule and in a crystal this exchange interaction is an "opposite sign" effect compare to the exchange interaction existing between the particles. Thus, the total exchange effect can either decrease or increase the energy of the system. For example, in ferromagnetics the minimum energy state corresponds to a situation when the electrons of the incompletely filled shells of the adjacent atoms are parallel. In contrast, in molecules with covalent bonding, for example the hydrogen molecule, the lowest energy state is when the spins of the electrons are antiparallel.

It was shown first by Heisenberg and then proved by Dirac that for the system of spins the exchange interaction energy represented above by the exchange integral A is expressed approximately by [151]

$$-2\sum_{ij} J\mathbf{S}_i \cdot \mathbf{S}_j, \tag{D.7}$$

where the value of J is called the exchange coefficient or exchange constant and is strongly related to the overlap of the coordinate (orbital) wave functions and hence to the interparticle distance, that is, $J = J(\mathbf{r}_{ij})$. In crystals, in general the exchange interaction is anisotropic and J is represented by a second-rank tensor. The reason is that the spatial coordinate wave functions are not spherically symmetrical in crystals. The spins feels the deviation from the spherical symmetry by means of the spin-orbit coupling.

An interesting example of the exchange interaction can be found when considering excitons in semiconductors. The exchange existing between an electron and a hole in an exciton can modify remarkably the optical excitonic spectra and is an important part of the exciton spin relaxation mechanisms. The theoretical treatment of the electron-hole exchange interaction starts from considering the interaction of two electrons that are respectively in the valence and conduction bands. Landau and Berestetskii, in positronium theory, derived rules for transforming the Hamiltonian that describes the interaction of two electrons in empty and filled bands, into a Hamiltonian describing the interaction of an electron and a positron. Similar rules are valid on going from electron-electron to electron-hole interaction [152].

References

[1] P. A. Fleury and J. F. Scott. Spin-flip Raman scattering from conduction electrons in CdS and ZnSe. *Phys. Rev. B*, 3(6):1079–1985, 1971.

[2] R. L. Hollis and J. F. Scott. Spin-flip scattering in ZnTe-experimental. *Phys. Rev. B*, 15(2):942–953, 1977.

[3] Y. Oka and M. Cardona. Resonant spin-flip Raman scattering on donor and acceptor states in ZnTe. *Phys. Rev. B*, 23(8):4129–4139, 1981.

[4] D. Heiman, P. A. Wolff, and J. Warnock. Spin-flip Raman scattering, bound magnetic polaron, and fluctuations in (Cd,Mn)Se. *Phys. Rev. B*, 27(8):4848–4860, 1983.

[5] D. L. Peterson, D. U. Bartholomew, U. Debska, A. K. Ramdas, and S. Rodriguez. Spin-flip Raman scattering in n-type diluted magnetic semiconductors. *Phys. Rev. B*, 32(1):323–340, 1985.

[6] S. I. Gubarev, T. Ruf, and M. Cardona. Resonant spin-flip Raman scattering on photoexcited carriers in p-type Cd(0.95)Mn(0.05)Te crystals. *Phys. Rev. B*, 43(18):14564–14568, 1991.

[7] J. Stühler, M. Hirsch, G. Schaack, and A. Waag. Raman scattering of the paramgnetic spin flip in Cd(1-x)Mn(x)Te, the role of band-gap excitations as intermediate states, and optically detected electron-nuclear double resonance. *Phys. Rev. B*, 49(11):7345–7356, 1994.

[8] C. M. Townsley, J. J. Davies, D. Wolverson, P. J. Boyce, G. Horsburgh, T. A. Steel, K. A. Prior, and B. C. Cavenett. Spin-flip Raman scattering studies of compensating donor centers in nitrogen-doped zinc selenide grown by molecular-beam epitaxy. *Phys. Rev. B*, 53(16):10983–10987, 1996.

[9] C. Orange, B Schlichtherle, D. Wolverson, and J. J. Davies. Angle-resolved studies of the spin-flip Raman scattering of holes bound to acceptors in p-type nitrogen-doped zinc selenide. *Phys. Rev. B*, 55(3):1607–1616, 1997.

[10] W. Heimbrodt, C. L. Orange, D. Wolverson, J. J. Davies, K. Kimura, and T. Yao. Determination of nitrogen-acceptor spin-Hamiltonian parameters in ZnSe epilayers via spin-flip Raman spectroscopy. *Phys. Rev. B*, 56(11):6889–6894, 1997.

[11] O. Z. Karimov, D. Wolverson, J. J. Davies, S. I. Stepanov, T. Ruf, S. V. Ivanov, S. V. Stepanov, C. B. O'Donnell, and K. A. Prior. The electron g-factor for cubic Zn(1-x)Cd(x)Se determined by spin-flip Raman scattering. *Phys. Rev. B*, 62(24):16582–16586, 2000.

[12] V. F. Sapega, M. Cardona, K. Ploog, E. L. Ivchenko, and D. N. Mirlin. Spin-flip Raman scattering in GaAs/Al(x)Ga(1-x)As quantum wells. *Phys. Rev. B*, 45(8):4320–4326, 1992.

[13] V. F. Sapega, T. Ruf, M. Cardona, K. Ploog, E. L. Ivchenko, and D. N. Mirlin. Resonant Raman scattering due to bound-carrier spin flip in GaAs/Al(x)Ga(1-x)As quantum wells. *Phys. Rev. B*, 50(4):2510–2519, 1994.

[14] A. A. Sirenko, T. Ruf, K. Eberl, M. Cardona, A. A. Kiselev, E. L. Ivchenko, and K. Ploog. Spin-flip Raman scattering in GaAs/AlAs multiple quantum wells. *Proceedings of the 12th Intl. Conf. on High Magnetic Fields in Semiconductor Physics.* Eds. G. Landwehr and W. Ossau. World Scientific, Singapore, 2:561–564, 1997.

[15] A. A. Sirenko, T. Ruf, M. Cardona, D. R. Yakovlev, W. Ossau, A. Waag, and G. Landwehr. Electron and hole g factors measured by spin-flip Raman scattering in CdTe/Cd(1-x)Mg(x)Te single quantum wells. *Phys. Rev. B*, 56(4):2114–2119, 1997.

[16] A. A. Sirenko, V. I. Belitsky, T. Ruf, M. Cardona, A. I. Ekimov, and C. Trallero-Griner. Spin-flip and acoustic-phonon Raman scattering in CdS nanocrystals. *Phys. Rev. B*, 58(4):2077–2087, 1998.

[17] T. Ruf, O. Z. Karimov, D. Wolverson, J. J. Davies, A. N. Reznitsky, A. A. Klochikhin, S. Yu. Verbin, L. N. Tenishev, S. A. Permogorov, and S. V. Ivanov. Spin-flip Raman scattering in submonolayer CdSe/ZnSe structures. *Physica B*, 273-274:911–914, 1999.

[18] J. J. Davies, D. Wolverson, I. J. Griffin, O. Z. Karimov, C. L. Orange, D. Hommel, and M. Behringer. Gyromagnetic ratios of electrons confined in quantum wells in ZnSe/Zn(x)Mg(1-x)S(y)Se(1-y) heterostructures. *Phys. Rev. B*, 62(15):10329–10334, 2000.

[19] R. J. Elliott. Theory of the effect of spin-orbit coupling on magnetic resonance in some semiconductors. *Phys. Rev.*, 96(2):266–279, 1954.

[20] R. J. Elliott and R. Loudon. The possible observation of electronic Raman transitions in crystals. *Phys. Lett.*, 3(4):189–191, 1963.

[21] P. A. Wolff. Thomson and Raman scattering by mobile electrons in crystals. *Phys. Rev. Lett.*, 16(6):225–228, 1966.

[22] Y. Yafet. Raman scattering by carriers in Landau levels. *Phys. Rev.*, 152(2):858–862, 1966.

[23] P. E. Kelley and G. B. Wright. Landau level Raman scattering. *Bull. Am. Phys. Soc.*, 11:812, 1966.

[24] R. E. Slusher, C. K. N. Patel, and P. A. Fleury. Inelastic light scattering from Landau-level electrons in semiconductors. *Phys. Rev. Lett.*, 18(3):77–79, 1967.

[25] D. G. Thomas and J. J. Hopfield. Spin-flip Raman scattering in cadmium sulfide. *Phys. Rev.*, 175(3):1021–1032, 1968.

[26] C. K. N. Patel and E. D. Shaw. Tunable stimulated Raman scattering from conduction elecrons in InSb. *Phys. Rev. Lett.*, 24(9):451–455, 1970.

[27] J. F. Scott and T. C. Damen. Anomalous double spin-flip Raman scattering in CdS, and a visible spin-flip laser. *Phys. Rev. Lett.*, 29(2):107–109, 1972.

[28] S. D. Smith, R. B. Dennis, and R. G. Harrison. The spin-flip Raman laser. *Prog. Quant. Electr.*, 5:205–292, 1977.

[29] J. F. Scott. Spin-flip Raman scattering in p-type semiconductors. *Rep. Prog. Phys.*, 43:951–1002, 1980.

[30] S. Geschwind and R. Romestain. High resolution spin-flip Raman scattering in CdS, in *Light Scattering in Solids IV, Topics in Applied Physics*, volume 54. Springer, Berlin, 1984.

[31] H. G. Häfele. Spin-flip Raman scattering, in *Landau Level Spectroscopy, Modern Problems in Condensed Matter Sciences*, volume 27.1. North-Holland, Amsterdam, 1991.

[32] J. J. Davies, D. Wolverson, O. Z. Karimov, and I. J. Griffin. Spin-flip Raman scattering studies of II-IV heterostructures. *J. Cryst. Growth*, 214/215:616–624, 1999.

[33] V. F. Sapega. Polarization of hot photoluminescence in magnetic field in GaAs crystals. PhD thesis, Ioffe Physical–Technical Insitute, Leningrad, Russia, 1984.

[34] M. Cardona. Resonance phenomena, in *Light Scattering in Solids II, Topics of Applied Physics*, volume 50. Springer, Berlin, 1982.

[35] W. Hayes and R. Loudon. *Scattering of Light by Crystals.* Wiley, Chichester, 1978.

[36] T. C. Damen, S. P. S. Porto, and B. Tell. Raman effect in zinc oxide. *Phys. Rev.*, 142(2):570–574, 1965.

[37] G. L. Bir and G. E. Pikus. *Symetry and strain-induced effects in semiconductors.* John Willey & Sons, Inc., New York, 1974.

[38] E. L. Ivchenko. Exchange interaction and spin-flip Raman-scattering by acceptor-bound holes in quantum-well structures. *Sov. Phys. Solid State*, 34(2):254–264, 1992.

[39] M. I. Dyakonov and V. I. Perel. Theory of optical spin orientation of electrons and nuclei in semiconductors, in *Optical Orientation, Modern Problems in Condensed Matter Sciences*, volume 8. North-Holland, 1984.

[40] M. Cardona. Introduction, in *Light Scattering in Solids I, Topics of Applied Physics*, volume 8. Springer, Berlin, 1983.

[41] M. V. Klein. Equivalence of resonant Raman scattering in solids with absorption followed by luminescence. *Phys. Rev. B*, 8(2):919–921, 1973.

[42] Y. R. Shen. Distinction between resonance Raman scattering and hot luminescence. *Phys. Rev. B*, 9(2):622–626, 1974.

[43] D. J. Stukel, R. N. Euwema, T. C. Collins, F. Herman, and R. L. Kortum. Self-consistent orthogonalized-plane-wave and empirically refined

orthogonalized-plane-wave energy-band models for cubic ZnS, ZnSe, CdS, and CdSe. *Phys. Rev.*, 179(3):740–751, 1969.

[44] C. Tuncay and M. Tomak. Empirical tight-binding band structure of wurtzite semiconductors SiC, ZnSe, and ZnTe. *phys. stat. sol. (b)*, 127:543–547, 1985.

[45] Y. D. Kim, M. V. Klein, S. F. Ren, Y.C. Chang, H. Luo, N. Samarth, and J. K. Furdyna. Optical properties of zinc-blende CdSe and Zn(x)Cd(1-x)Se film grown on GaAs. *Phys. Rev. B*, 49(11):7262–7270, 1994.

[46] M. L. Cohen and J. R. Chelikowsky. *Electronic structure and optical properties of Semiconductors.* Springer, Berlin, 2nd edition, 1989.

[47] A. S. Nasibov, Y. V. Korostelin, P.V. Shapkin, L. G. Suslina, D. L. Fedorov, and L. S. Markov. Exciton luminescence in ideal solid solutions (Zn(x)Cd(1-x)Se system, 0<x<1). *Solid State Commun.*, 71(10):867–869, 1989.

[48] N. Samarth, H. Luo, J. K. Furdyna, R.G. Alonso, Y. R. Lee, A. K. Ramdas, S. B. Qadri, and N. Otsuka. Molecular beam epitaxy of ZnCdSe epilayers and ZnSe and ZnSe/ZnCdSe superlattices. *Appl. Phys. Lett.*, 56(12):1163–1165, 1990.

[49] R. Hill. Energy-gap variations in semiconductor alloys. *J. Phys. C*, 7:521–526, 1974.

[50] S. Permogorov and A. Reznitsky. Effect of disorder on the optical spectra of wide-gap II-VI semiconductor solid solutions. *J. Luminescence*, 52:201–223, 1992.

[51] H. J. Lozykowsky and V. K. Shastri. Excitonic and Raman properties of ZnSe/ZnCdSe strained-layer quantum wells. *J. Appl. Phys.*, 69(5):3235–3242, 1991.

[52] N. Samarth, H. Luo, J. K. Furdyna, R.G. Alonso, S. B. Qadri, Y. R. Lee, A. K. Ramdas, and N. Otsuka. Growth of cubic (zinc blende) CdSe by molecular beam epitaxy. *Appl. Phys. Lett.*, 54(26):2680–2682, 1989.

[53] D. Stroud. Band gaps of semiconductor alloys. *Phys. Rev. B*, 5(8):3366–3368, 1972.

[54] M. Y. Valakh, M. P. Lisitsa, G. S. Pekar, G. N. Polysskii, V. I. Sidorenko, and A. M. Yaremko. Anharmonic coupling of phonon modes in mixed ZnCdSe crystals. *phys. stat. sol (b)*, 113:635–645, 1982.

[55] Y. Kawakami, M. Funato, Sh. Fujita, S. Fujita, Y. Yamada, and Y. Masumoto. Localized excitons in cubic ZnCdS lattice matched to GaAs. *Phys. Rev. B*, 50(19):14655–14658, 1994.

[56] I. M. Lifshitz. The energy spectrum of disordered systems. *Ad. Phys.*, 13(52):483–536, 1965.

[57] R. Zimmermann. Theory of exciton linewidth in II-VI semiconductor mixed crystals. *J. Cryst. Growth*, 101:346–349, 1990.

[58] H. Mayer, U. Rössler, K. Wolf, A. Elsner, H. Stanzl, T. Reisinger, and W. Gebhardt. Strain splitting of nitrogen acceptor levels in ZnSe. *Phys. Rev. B*, 52(7):4956–4964, 1995.

[59] H. Mayer, U. Rössler, S. Permogorov, H. Stolz, H. Vogelsang, and W.von der Osten. Resonant Brillouin scattering in biaxially strained ZnSe. *J. Cryst. Growth*, 138:195–198, 1994.

[60] J. W. Matthews and A. E. Blakeslee. Defects in epitaxial multilayers. *J. Cryst. Growth*, 27:118–125, 1974.

[61] C. B. O'Donnell, G. Lacey, G. Horsburgh, A. G. Cullis, C. R. Whitehouse, P. J. Parbrook, W. Meredith, I. Galbraith, P. Möck, K. A. Prior, and B. C. Cavenett. Measurements by X-ray topography of the critical thickness of ZnSe grown on GaAs. *J. Cryst. Growth*, 184/185:92–95, 1998.

[62] A. Krost, G. Bauer, and J. Woitok. High resolution x-ray diffraction, in *Optical characterization of epitaxial semiconductor layers.* Springer, Berlin, 1996.

[63] S. Nakashima, A. Fujii, K. Mizoguchi, A. Mitsuishi, and K. Yoneda. Raman scattering measurements of strains in ZnSe epitaxial films on GaAs. *Jpn. J. Appl. Phys.*, 27(7):1327–1330, 1988.

[64] T. Ohtsuka, J. Kawamata, Z. Zhu, and T. Yao. *p*-type CdSe grown by molecular beam epitaxy using a nitrogen plasma scource. *Appl. Phys. Lett.*, 65(4):467–468, 1994.

[65] C. G. Van de Walle. Band lineups and deformation potentials in the model-solid theory. *Phys. Rev. B*, 39(3):1871–1883, 1989.

[66] M. V. Maximov, I. L. Krestnikov, S. V. Ivanov, N. N. Ledentsov, and S. V. Sorokin. Calculation of the size-quantization levels in strained ZnCdSe/ZnSe quantum wells. *Semiconductors*, 31(8):800–803, 1997.

[67] R. Essaid, P. Biegenwald, S. Sanchez, T. Cloitre, F. Liaci, B. Gil, and R-L Aulombard. Linear spectroscopy and exciton binding energies in ZnCdSe-ZnSe heterostructures. *Materials Science and Engineering*, B43:116–120, 1997.

[68] P. Biegenwald, B. Gil, L. Konczewicz, and P. Testud. ZnSe-ZnCdSe single quantum wells: dispersion relations and absorption processes. *Materials Science and Engineering*, B43:133–136, 1997.

[69] B. Gil and P. Biegenwald. Variational treatment of the exciton binding energy problem in low-dimensional systems with one marginal potential. *Solid State Commun.*, 94:883–888, 1995.

[70] P. J. Parbrook, P. J. Wright, B. Cockayne, A. G. Cullis, B. Henderson, and K. P. O'Donnell. The growth of ZnSe/CdSe and ZnS/CdS strained layer superlattices by MOVPE. *J. Cryst. Growth*, 106:503–509, 1990.

[71] S. H. Xin, P. D. Wang, A. Yin, C. Kim, M. Dobrowolska, J. L. Merz, and J. K. Furdyna. Formation of self-assembling CdSe quantum dots on ZnSe by molecular beam epitaxy. *Appl. Phys. Lett*, 69:3884–3886, 1996.

[72] S. V. Ivanov, A. A. Toropov, S. V. Sorokin, T. V. Shubina, I. V. Sedova, A. A. Sitnikova, P. S. Kop'ev, Zh. I. Alferov, H.-J. Lugauer, G. Reuscher, M. Keim, F. Fischer, A. Waag, and G. Landwehr. CdSe fractional-monolayer active region of molecular beam epitaxy grown green ZnSe-based laser. *Appl. Phys. Lett.*, 74:498–500, 1998.

[73] Z. Zhu, H. Yoshihara, K. Takebayashi, and T. Yao. Interfacial alloy formation in ZnSe/CdSe quantum-well heterostructures characterized by photoluminescence spectroscopy. *Appl. Phys. Lett.*, 63:1678–1680, 1993.

[74] M. Strassburg, V. Kutzer, U. W. Pohl, A. Hoffman, I. Broser, N. N. Ledentsov, D. Bimberg, A. Rozenauer, U. Fischer, D. Gerthsen, I. L. Krestnikov, M. V. Maximov, P. S. Kop'ev, and Zh. I. Alferov. Gain studies of

ZnCdSe quantum islands in a ZnSe matrix. *Appl. Phys. Lett.*, 72:942–944, 1998.

[75] M. C. Bartelt and J. W. Evans. Scaling analysis of diffusion-mediated island growth in surface absorption process. *Phys. Rev. B*, 46:12675–12687, 1992.

[76] V. Bressler-Hill, A. Lorke, S. Varma, P. M. Petroff, K. Pond, and W. H. Weinberg. Initial stages of InAs epitaxy on vicinal GaAs(001)-(2x4). *Phys. Rev. B*, 50:8479–8487, 1994.

[77] A. G. Khachaturyan. *Theory of structural transformations in solids.* Wiley, New York, 1983.

[78] V. I. Marchenko and A. Ya. Parshin. Elastic properties of crystal surfaces. *Sov. Phys. JETP*, 52:129–131, 1981.

[79] V. I. Marchenko. Possible structures and phase transitions on the surface of crystals. *JETP Lett.*, 33:381–383, 1981.

[80] V. A. Shchukin, N. N. Ledentsov, P. S. Kop'ev, and D. Bimberg. Spontaneous ordering of arrays of coherent strained islands. *Phys. Rev. Lett.*, 75:2968–2971, 1995.

[81] S. Ivanov, S. Sorokin, I. Krestnikov, N. Faleev, B. Ber, I. Sedova, Yu. Kudryavtsev, and P. Kop'ev. Interplay of kinetics and thermodynamics in molecular beam epitaxy of (Mg,Zn,Cd)S,Se. *J. Cryst. Growth*, 184/185:70–74, 1998.

[82] W. Meredith, G. Horsburgh, G. D. Brownlie, K. A. Prior, B. C. Cavenett, W. Rothwell, and A. J. Dann. Microprobe Raman study of the variation of LO phonon frequency with Cd concentration in the ternary compound Zn(1-x)Cd(x)Se. *J. Cryst. Growth*, 159:103–107, 1996.

[83] P. Yu and M. Cardona. *Fundamentals of semiconductors.* Springer, Berlin, second edition, 1999.

[84] G. Kudlek and J. Gutowski. Analysis of strain and impurity distribution in II-IV epilayers with optical methods. *J. Luminescence*, 52:55–69, 1992.

[85] C. D. Lee, S. I. Min, and S. K. Chang. High purity ZnSe epilayers grown by atmospheric double zone metalorganic atomic layer epitaxy. *J. Cryst. Growth*, 159:108–111, 1996.

[86] D. Wolverson, P. J. Boyce, C. M. Townsley, B. Schlichtherle, and J. J. Davies. Spin-flip Raman scattering studies of doped epitaxial zinc selenide. *J. Crysr. Growth*, 159:229–237, 1996.

[87] D. J. Dunstan, J. E. Nicholls, B. C. Cavenett, and J. J. Davies. Zinc vacancy-associated defects and donor-acceptor recombination in ZnSe. *J. Phys. C: Solid State Phys.*, 13(34):6409–6419, 1980.

[88] J. J. Davies, J. E. Nicholls, and C. P. Hilton. Direct determination of the signs of the g-factors of shallow donor electrons in CdS, in ZnS, in ZnSe and in ZnS(x)Se(1-x). *J. Phys. C: Solid State Phys.*, 18(0):1035–1036, 1985.

[89] M. Willatzen, M. Cardona, and N. E. Christensen. Spin-orbit coupling parameters and g factor of II-VI zinc-blende materials. *Phys. Rev. B*, 51(24):17992–17994, 1995.

[90] Landolt-Börnstein. *Numerical Data and Functional Relationships in Science and Technology*, volume 22. Springer, Berlin, 1987.

[91] L. M. Roth. g factor and donor spin-lattice relaxation for electrons in germanium and silicon. *Phys. Rev.*, 118(6):1534–1540, 1960.

[92] M. Cardona. Band parameters of semiconductors with zincblende, wurtzite, and germanium structure. *J. Phys. Chem. Solids*, 24:1543–1555, 1963.

[93] C. Hermann and C. Weisbuch. $\mathbf{k}\cdot\mathbf{p}$ perturbation theory in III-V compounds and alloys: a reexamination. *Phys. Rev. B*, 15(2):823–833, 1977.

[94] M. Cardona. Comment on "g-factor anisotropy of conduction electrons in InSb". *Phys. Rev. B*, 34(10):7402–7403, 1986.

[95] D. Wolverson, J. J. Davies, C. L. Orange, K. Ogata, Sz. Fujita, Sg. Fujita, K. Nakano, H. Okuyama, S. Itoh, B. Jobst, and D. Hommel. Spin-flip Raman scattering of wide-band-gap II-VI ternary alloys. *Phys. Rev. B*, 60(24):13555–13560, 1999.

[96] M. Cardona, N. E. Christensen, and G. Fasol. Relativistic band structure and spin-orbit splitting of zink-blende-type semiconductors. *Phys. Rev. B*, 38(3):1806–1827, 1988.

[97] H. K. Ng, Y. A. Leem, R. Knobel, I. P. Smorchkova, A. A. Sirenko, and N. Samarth. Cyclotron resonance in modulation-doped ZnSe/Zn(1-x)Cd(x)Se and ZnTe/CdSe single quantum wells. *Phys. Rev. B*, 75(23):3662–3664, 1999.

[98] C. Janowitz, O. Gunther, G. Jungk, R. L. Johnson, P. V. Santos, M. Cardona, W. Fasching, and H. Sitter. Dielectric function and critical-points of cubic and hexagonal CdSe. *Phys. Rev. B*, 50(4):2181–2187, 1994.

[99] J. Puls and F. Henneberger. Electron-hole exchange interaction of excitons in quantum wells. *phys. stat. sol. (a)*, 164:499–504, 1997.

[100] J. Puls, H.-J. Wünsche, and F. Henneberger. Bi-excitons in wide-gap II-VI quantum wells. *Chem. Phys.*, 210(1-2):235–247, 1996.

[101] A. Klochikhin, A. Reznitsky, S. Permogorov, T. Breitkopf, M. Grun, M. Hetterich, C. Klingshirn, V. Lyssenko, W. Langbein, and J. M. Hvam. Luminescence spectra and kinetics of disordered solid solutions. *Pphys. Rev. B*, 59(20):12947–12972, 1999.

[102] S. Permogorov, A. Klochikhin, A. Reznitsky, L. Tenishev, S. Ivanov, S. Sorokin, and C. Klingshirn. Two-dimensional localization of excitons in qws formed by II-VI solid solutions. *J. Cryst. Growth*, 214/215:1158–1159, 2000.

[103] S. V. Ivanov, A. A. Toropov, T. V. Shubina, S. V. Sorokin, A. V. Lebedev, I. V. Sedova, P. S. Kop'ev, G. R. Pozina, J. P. Bergman, and B. Monemar. Growth and excitonic properties of single fractional monolayer CdSe/ZnSe structures. *J. Appl. Phys.*, 83(6):3168–3171, 1998.

[104] N. N. Ledentsov, I. L. Krestnikov, M. V. Maximov, S. V. Ivanov, S. V. Sorokin, Kop'ev, Zh. I. Alferov, D. Bimberg, and C. M. Sotomayor Torres. Response to "Comment on 'Ground state exciton lasing in CdSe submonolayer inserted in a ZnSe matrix' "[Appl. Phys. Lett. 70, 2765 (1997)]. *Appl. Phys. Lett.*, 70(20):2766–2767, 1997.

[105] A. A. Sirenko, T. Ruf, N. N. Ledentsov, A. Y. Egorov, P. S. kop'ev, V. M. Ustinov, and A. E. Zhukov. Resonant spin-flip Raman scattering and localized exciton luminescence in submonolayer InAs-GaAs structures. *Solid State Commun.*, 97(3):169–174, 1996.

[106] M. P. Halsall, S. V. Railson, D. Wolverson, J. J. Davies, B. Lunn, and D. A. Ashenford. Spin-flip Raman scattering in CdTe/Cd(1-x)Mn(x)Te multiple quantum wells: A model system for the study of electron-donor binding in semiconductor heterostructures. *Phys. Rev. B*, 50(16):11755–11763, 1994.

[107] K. Kheng, R. T. Cox, Y. M. Daubigne, F. Bassani, K. Saminadayar, and S. Tatarenko. Observation of negatively charged excitons X^- in semiconductor quantum-wells. *Phys. Rev. Lett.*, 71(11):1752–1755, 1992.

[108] E. L. Ivchenko and A. A. Kiselev. Electron g factor of quantum wells and superlattices. *Sov. Phys. Semicond.*, 26(8):827–831, 1992.

[109] G. E. W. Bauer and T. Ando. Exciton mixing in quantum wells. *Phys. Rev. B*, 38(9):6015–6030, 1988.

[110] L. C. Andreani and F. Bassani. Exchange interaction and polariom effects in quantum-well escitons. *Phys. Rev. B*, 41(11):7536–7544, 1990.

[111] M. Z. Maialle, E. A. de Andrada e Silva, and L. J. Sham. Exciton spin dinamics in quantum wells. *Phys. Rev. B*, 47(23):15776–15788, 1993.

[112] A. Franceschetti, L. W. Wang, H. Fu, and A. Zunger. Short-range versus long-range electron-hole exchange interaction in semiconductor quantum dots. *Phys. Rev. B*, 58(20):13367–13370, 1998.

[113] H. Fu, L. W. Wang, and A. Zunger. Excitonic exchange splitting in bulk semiconductors. *Phys. Rev. B*, 59(8):5568–5574, 1999.

[114] M. M. Denisov and V. P. Makarov. Longitudinal and transverse excitons in semiconductors. *phys. stat. sol. (b)*, 56(9):9–58, 1973.

[115] K. Cho. Unified theory of symmetry-breaking effects on excitons in cubic and wurtzite structures. *Phys. Rev. B*, 14(10):4463–4482, 1976.

[116] E. L. Ivchenko and A. Yu. Kaminskii. Optically-detectable localized-exciton level anticrossing in semiconductors. *Phys. Solid State*, 37(5):768–773, 1995.

[117] H. W. van Kersten, E. C. Cosman, and W. A. J. A. van der Poel. Fine structure of excitons in type-II GaAs/AlAs quantum wells. *Phys. Rev. B*, 41(8):5283–5292, 1989.

[118] S. V. Gupalov, E. I. Ivchenko, and A. V. Kavokin. Anisotropic exchange splitting of excitonic levels in small quantum systems. *Superlattices and Microstructures*, 23(6):1205–1209, 1996.

[119] S. Yu. Verbin. Private communication.

[120] M. Bayer, O. Stern, A. Kuther, and A. Forchel. Spectroscopy study of dark excitons in $In_xGa_{1-x}As$ self-assembled quantum dots by a magnetic-field-induced symmetry breaking. *Phys. Rev. B*, 61(11):7273–7276, 2000.

[121] W. M. Chen, M. Godlewski, B. Monemar, and J. P. Bergman. Steady-state level-anticrossing spectra for bound-exciton triplets associated with complex defects in semiconductors. *Phys. Rev. B*, 41(9):5746–5755, 1990.

[122] U. Woggon, F. Gindele, W. Langbein, and M. Hetterich. Exchange interaction in II-VI quantum dots and wells. *phys. stat. sol. (a)*, 164:505–510, 1997.

[123] M. Nirmal, D. J. Norris, M. Kuno, and M. G. Bawendi. Observation of the "dark exciton" in cdse quantum dots. *Phys. Rev. Lett.*, 75(20):3728–3731, 1995.

[124] A. A. Klochikhin. Private communication.

[125] R. Bauer, D. Bimberg, J. Christen, D. Oertel, D. Mars, J. N. Miller, T. Fukunaga, and H. Nakashima. Reduced dimensionality induced doublet splitting of heavy hole exciton in GaAs wells. *Proc. of the 18th Int. Conference on the Physics of Semiconductors*, 1:525–528, 1986.

[126] Y. Chen, B. Gil, P. Lefebvre, and H. Mathieu. Exchange effects on excitons in quantum wells. *Phys. Rev. B*, 37(11):6429–6432, 1988.

[127] E. Blackwood, M. J. Snelling, R. T. Harley, S. R. Andrews, and C. T. Foxon. Exchange interaction of excitons in GaAs heterostructures. *Phys. Rev. B*, 50(19):14246–14254, 1994.

[128] J. Puls, M. Rabe, H.-J. Wünsche, and F. Henneberger. Magneto-optical study of the exciton fine structure in self-assembled CdSe quantum dots. *Phys. Rev. B*, 60(24):16303–16306, 1999.

[129] S. T. Pavlov and Y. A. Firsov. The spin-phonon interaction of electrons and the oscillations of the longitudinal magnetoresistance in semiconductors. *Sov. Phys. Solid State*, 9(6):1394–1402, 1967.

[130] A. V. Khaetskii and Y. V. Nazarov. Spin-dephasing processes in semiconductor quantum dots. *Phyisca E*, 6:470–473, 2000.

[131] G. E. Pikus and A. N. Titkov. Spin relaxation under optical orientation in semiconductors, in *Optical Orientation, Modern Problems in Condensed Matter Sciences*, volume 8. North-Holland, 1984.

[132] A. Vinattieri, J. Shah, T. C. Damen, D. S. Kim, L. N. Pfiffer, M. Z. Maialle, and L. J. Sham. Exciton dynamics in GaAs quantum wells under resonant excitation. *Phys. Rev. B*, 50(15):10868–10879, 1994.

[133] R. Spiegel, G. Bacher, A. Forchel, B. Jobst, D. Hommel, and G. Landwehr. Plarization-dependent formation of biexcitons in ZnCdSe/ZnSe quantum wells. *Phys. Rev. B*, 55(15):9866–9871, 1997.

[134] J. Schwinger. On quantum-electrodynamics and the magnetic moment of the electron. *Phys. Rev.*, 73(0):416–417, 1948.

[135] J. M. Luttinger. A note on the magnetic moment of the electron. *Phys. Rev.*, 74(8):893–898, 1948.

[136] Y. Yafet. *g factors and spin-relaxation of conduction electrons,* in Solid State Physics: Advances in research and applications. Eds. F. Seitz and D. Turnbull, volume 14. Academic Press, New York and London, 1963.

[137] G. Denninger and H. Pascher. Overhauser shift and dynamic nuclear polarization in InSb observed by coherent spin-flip Raman scattering. *Semicond. Sci. Technol.*, 5:S172–S175, 1990.

[138] J. M. Luttinger and W. Kohn. Motion of electrons and holes in perturbed periodic fields. *Phys.Rev.*, 97(4):869–883, 1955.

[139] J. M. Luttinger. Quantum theory of cyclotron reonance in semiconductors: general theory. *Phys. Rev.*, 102(4):1030–1041, 1956.

[140] Y. Yafet. The g value in conduction electron spin resonance. *Phys. Rev.*, 106(4):679–684, 1956.

[141] M. H. Cohen and E. I. Blount. The g-factor and de Haas-van Alphen effect of electrons in Bismuth. *Phil. Mag.*, 5:115–126, 1960.

[142] L. I. Schiff. *Quantum mechanics.* McGraw-Hill, 3rd edition, 1984.

[143] J. Singh. *Physics of semiconductors and their heterostructures.* McGraw-Hill, 1993.

[144] P. O. Löwdin. A note on the quantum-mechanical perturbation theory. *J. Chem. Phys.*, 19(11):1396–1401, 1951.

[145] E. O. Kane. Energy band structure in p-type germanium and silicon. *J. Phys. Chem. Solids*, 1:82–99, 1956.

[146] C. R. Pidgeon and R. N. Brown. Interband magneto-absorption and Faraday rotation in InSb. *Phys. Rev.*, 146(2):575–583, 1966.

[147] U. Rössler. Nonparabolicity and warping in the conduction band of GaAs. *Solid State Commun.*, 49(0):943, 1984.

[148] G. E. Pikus. Spin zone spallation in A(III)B(V) cubic-crystals. *Izv. Akad. Nauk SSSR, Seria Fiz.*, 52(3):493–496, 1988.

[149] P. Pfeffer and W.Zawadzki. Five-level $\mathbf{k} \cdot \mathbf{p}$ model for the conduction and valence bands in GaAs and InP. *Phys. Rev. B*, 53(19):12813–12828, 1995.

[150] G. Burns. *Solid state physics.* Academic Press, Inc., Orlando, Florida, 1985.

[151] W. Low. *Paramagnetic resonance in solids,* in Solid State Physics: Advances in research and applications. Eds. F. Seitz and D. Turnbull. Academic Press, New York and London, 1960.

[152] G. E. Pikus and G. L. Bir. Exchange interaction in excitons in semiconductors. *Sov. Phys. -JETP*, 33(1):108–114, 1971.